Behaviour of uniformly dimpled colloidal particles

Samantha Ivell

Lincoln College
University of Oxford

Supervisor: Prof. Dirk Aarts

A thesis submitted for the degree of
Doctor of Philosophy

Hilary Term 2014

Abstract

Uniformly dimpled colloidal particles are studied using laser scanning confocal microscopy and optical tweezing, alongside real-space image analysis. In particular, a comparison is made between the behaviour of these particles with that of isotropic spherical particles of the same size and polydispersity.

We begin by detailing the synthetic techniques as well as the methods used for both experiments and simulations in this work. We then probe the structures and ordering exhibited by the dimpled particles and their spherical counterparts at a single featureless wall. Only the first layer at the wall is observed, and pronounced differences in both the translational and orientational order between the two types of particle is found. Furthermore, we show that the presence of the dimple leads to disordered structures that develop over time. Next, we reduce the dimensionality of the system to quasi-two and study the depletion induced interactions in a monolayer of colloidal particles at a single featureless wall. Using both confocal microscopy and Monte Carlo simulations, we illustrate the selectivity of the depletion interaction with regard to particle shape and polymer size. A level of complexity is then added to the problem by introducing a second colloidal system of small spherical particles. The resulting binary mixture, still with additional non-adsorbing polymer and in a monolayer at a wall, allows us to investigate so-called "lock and key" binding. We show that the inclusion of a lock particle cavity, whose shape and size is complementary to those of the key particle, significantly favours binding behaviour, which is further improved by using a depletant consisting of a small polymer and charge-screening salt. Finally, the depletion induced force between lock and key particles at contact is directly measured using optical tweezers. The dependence of the force due to depletion upon the overlap volume between the particles is illustrated, and we find that the strongest force is produced when the key is held within the cavity of the dimpled lock, demonstrating semi-quantitative agreement with theoretical predictions.

Declaration

This thesis is submitted for the degree of Doctor of Philosophy in Physical and Theoretical Chemistry at the University of Oxford. No part of this thesis has been accepted or is currently being submitted for any degree, diploma, certificate or other qualification in this University or elsewhere. This thesis is wholly my own work, except where indicated.

Contents

Abstract **i**

Declaration **iii**

1 Introduction **1**

1.1 Colloidal systems 1

1.2 Complexity in colloidal systems 2

1.3 Interparticle interactions 3

1.4 Uniformly dimpled colloidal particles 4

1.5 Scope of the thesis 5

2 Synthetic techniques and experimental methods **7**

2.1 Introduction 8

2.2 Particle synthesis 8

2.2.1 Uniformly dimpled colloidal particles 8

2.2.2 Spherical particles 9

2.3 Polymer synthesis 10

2.4 Sample preparation 12

2.5 Sample cells 13

2.6 Confocal microscopy 15

2.7 Static light scattering 18

2.8 Optical trapping 19
2.9 Particle tracking 22
2.9.1 IDL routine 22
2.9.2 Mathematica routine 23

3 Monte Carlo simulations 25
3.1 Introduction 26
3.2 Algorithm details 26
3.2.1 Moving a colloidal particle 29
3.2.2 Moving a polymer particle 34

4 Emerging disorder of uniformly dimpled colloidal particles 37
4.1 Introduction 38
4.2 Experimental details 39
4.3 Results and discussion 40
4.4 Conclusions 46

5 Shape anisotropy and depletion interactions at a planar wall 47
5.1 Introduction 48
5.2 Theory 49
5.2.1 Depletion attractions 49
5.2.2 DLVO theory 51
5.2.3 Total forces 53
5.3 Experiments 54
5.3.1 Experimental setup 54
5.3.2 Results and discussion 55
5.4 Simulations 62
5.4.1 Simulation parameters 62

5.4.2 Results and discussion 63
5.5 Conclusions 64

6 Depletion induced binding of lock and key colloids 65

6.1 Introduction 66
6.2 Theory 66
6.3 Experimental details 68
6.4 Results and discussion 70
6.4.1 Polymer concentration 71
6.4.2 Polymer size 75
6.4.3 Particle shape 77
6.4.4 Calculation of dimple depth 80
6.4.5 Self-interactions 80
6.5 Conclusions 81

7 Direct measurement of depletion induced forces 83

7.1 Introduction 84
7.2 Theory 85
7.2.1 Optical forces 86
7.2.2 Force due to the depletion interaction 86
7.3 Experimental details 87
7.4 Results and discussion 89
7.5 Conclusions 95

Summary 97

A Calculating the volume of the overlap of depletion zones 99

A.1 Lock-lock overlaps 99
A.1.1 Dimpled particles in chain formation 100

A.1.2 Dimpled particles in dimple-down formation 102

A.1.3 Spherical particles 104

A.2 Lock-key overlaps 105

List of publications **119**

Acknowledgements **121**

Chapter 1

Introduction

Colloidal systems are extremely versatile, and have applications in fields ranging from fundamental physics to drug delivery [1]. In this introduction, we define what is meant by the term "colloidal", and outline the characteristic features that make colloid science so rich. The addition of complexity in such systems is then discussed in section 1.2, along with a brief overview of the interparticle interactions in section 1.3. In section 1.4, we introduce the uniformly dimpled particles from whom this thesis takes its name, and we finish by presenting the scope of the thesis in section 1.5.

1.1 Colloidal systems

In the 1860s, Thomas Graham first proposed the epithet "colloid" (stemming from the Greek for glue [2, 3]) due to his observations of gelatine-like behaviour in suspensions of particles in liquid. Following on from this, the term "colloidal" is now defined by the International Union of Pure and Applied Chemistry (IUPAC) as being a "state of subdivision, implying that the molecules or polymolecular particles dispersed in a medium have at least in one direction a dimension roughly between 1 nm and 1 μm, or that in a system discontinuities are found at distances of that order" [4]. This rather broad definition means that a wide variety of systems can be labelled as colloidal, as determined solely by their characteristic length scales.

By virtue of these length scales, colloidal particles are known to exhibit erratic, so-called Brownian motion, named after Robert Brown, who, in 1827, noted that the movement of pollen

grains in water appeared to be random [5]. It was later deduced that this was a product of continual collisions with the solvent molecules [2,3,6]. The first theoretical treatments of Brownian motion were provided almost simultaneously by Einstein, von Smoluchowski and Langevin, and were put to the test by Perrin in the early 1900s [6–11]. In this revolutionary work, Perrin directly measured the root-mean-square displacements of spherical colloidal particles as a function of time, and was able to both experimentally obtain a value for Boltzmann's constant, and provide the first direct proof for the existence of atoms and molecules [2]. Perrin's experiments demonstrate one of the fundamental uses of colloidal systems: to model atomic systems [1].

The ability to mimic atomic behaviour is a direct consequence of the colloidal size regime. Colloidal particles are known to be thermodynamically similar to atoms at equilibrium [7,8,12], but the former are much more experimentally accessible. Not only are the length scales involved such that colloidal particles are directly resolvable using optical microscopy [13,14], but, since the diffusion coefficient scales with the inverse of particle radius, they move slowly enough that their behaviour can be easily tracked in real time [15,16]. Additionally, colloidal systems can be referred to as "soft", meaning that their elastic constants are much smaller than those in the equivalent atomic systems [12]. This means that colloids feel the effect of weaker external forces [17] - a fact that is exploited in optical tweezing, for example.

1.2 Complexity in colloidal systems

Due to recent advances in synthetic techniques, it is now possible to create colloidal particles that vary hugely in features such as shape and surface chemistry. Following on from the use of spherical colloidal particles as models for atoms, the inclusion of additional complexity allows us to probe more elaborate systems; indeed a range of particles, dubbed "colloidal molecules" [18,19], has been produced, whose shapes mirror those of space-filling models of molecules such as water and ammonia [20,21]. However, the usefulness of novel particles such as these is not simply limited to their resemblance to atoms and molecules, but extends to additional properties that are interesting in their own right, as discussed below.

The ability of particles to spontaneously self-assemble has been the subject of great interest in colloid science for many years, and has been one of the contributing factors towards the development of more complex colloidal systems [22–29]. With the addition of anisotropy, it is

believed that structures that are far more intricate and technologically exciting are accessible. A prime example of this is the photonic band gap crystal: a crystal through which light of certain frequencies cannot propagate, and one that is thought to be achievable using non-spherical colloidal particles [30–34]. Self-assembling building blocks come in many forms, as hinted previously, and can be split into three main categories: those which are anisotropic in shape, for example cubes [35], peanuts [36] and raspberries [37]; those with non-uniform surface chemistry, including Janus [38–40] and patchy particles [41]; and those combining the two, such as "elephant trunk-like" and "acorn-like" Janus particles [42] and amphiphilic mushroom-caps [43]. Although all three classes are important, it is the first that constitutes the focus of this thesis.

1.3 Interparticle interactions

In the 1940s, Derjaguin and Landau [44] and independently, Verwey and Overbeek [45] described the interactions present between colloidal particles in suspension. Their combined findings have since become known as DLVO theory, and describe the interplay between the long range van der Waals attractions and the short range double layer repulsions. We are able to manipulate the interparticle interactions in the lab by, for example, altering the surface chemistry of the particles, changing the solvent properties, or adding components such as polymers [46].

The introduction of polymers into a colloidal suspension allows the interparticle interactions to be finely tuned. Asakura and Oosawa [47, 48], and later, Vrij [49] noted that two bodies in a solution of macromolecules feel an interaction owing to an osmotic pressure imbalance. When suspended in a polymer solution, there exists a region surrounding each colloidal particle from

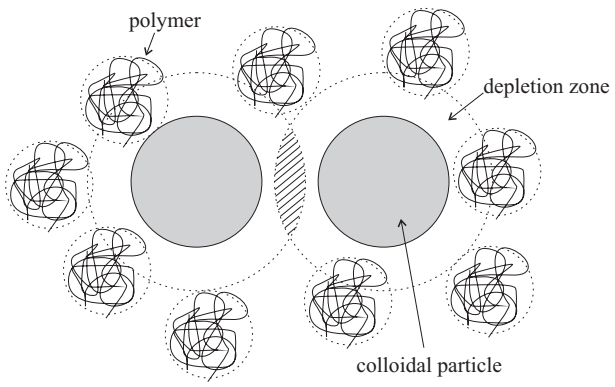

Figure 1.1: The origin of the depletion interaction. Colloidal particles are pushed together due to the osmotic imbalance caused by the overlap of depletion zones.

which the centres of mass of the polymer particles are entropically excluded - this is known as the depletion zone. When two colloidal particles approach one another, the depletion zones overlap causing a disparity in osmotic pressure, which leads to an interparticle attraction (see figure 1.1). In the work presented in this thesis, we use polymer particles to induce this so-called depletion interaction, and are able to control both the range and strength of the interaction by varying the size and concentration of polymer, respectively. Polymers of different sizes additionally allow us to vary the shape selectivity of the interparticle interaction.

1.4 Uniformly dimpled colloidal particles

The systems of interest in this work are based upon colloidal suspensions of the "lock" particles of Sacanna et al. [50, 51]. These particles are uniform in surface chemistry, but anisotropic in shape due to the inclusion of a well-defined dimple on an otherwise spherical particle (see figure 1.2(a)). It is this shape anisotropy that makes these particles behave in such a compelling way, particularly when in the presence of additional depletant. As outlined in section 1.3, polymers may be used to induce a depletion attraction between colloidal particles, and, as shown in figure 1.2(b), this interaction is highly directionally selective in our system.

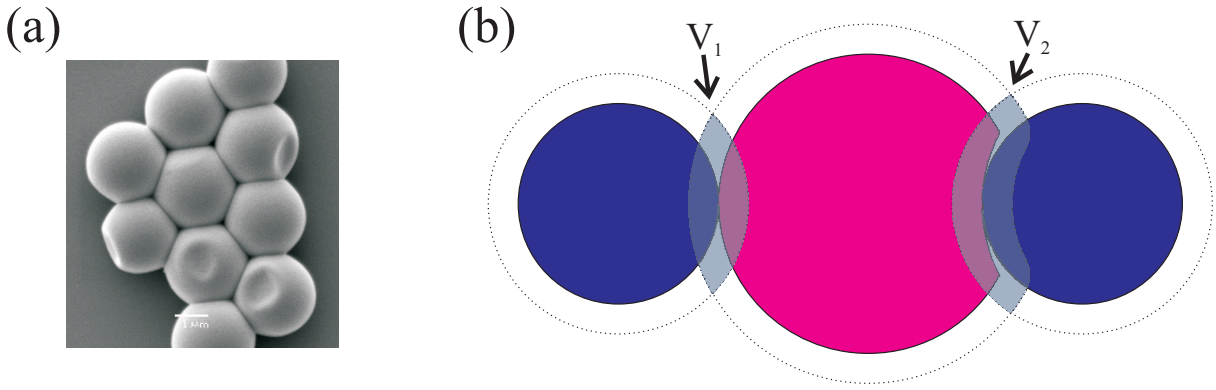

Figure 1.2: (a) Scanning electron microscopy image of the dimpled particles. (b) The depletion attraction is proportional to the overlap volume of the depletion zones, denoted here by V_1 and V_2. V_2 is bigger than V_1 and hence we see a directionally selective interparticle interaction.

1.5 Scope of the thesis

In this thesis, the behaviour of uniformly dimpled colloidal particles (introduced in section 1.4) is studied using confocal microscopy and real-space image analysis. In particular, the changes in the structures and ordering seen due to the inclusion of a single round cavity on an otherwise spherical particle are probed in a variety of systems.

We begin in chapter 2 by detailing the synthetic pathways and experimental setups used throughout this work. Protocols for the synthesis of both the colloidal particles and the polymer solutions are provided, as well as information about the cells in which the experimental systems are contained. We outline the experimental techniques used, including confocal microscopy, static light scattering and optical trapping, and present the routines used for particle tracking.

Chapter 3 introduces Monte Carlo simulations and their uses for both experimentalists and theorists. An overview of the specific algorithm used to simulate the experimental systems in this work is presented.

In chapter 4 we investigate the ordering of colloidal particles in the vicinity of a single featureless wall. We demonstrate that a small perturbation in the shape of a particle can lead to disordered structures that develop over time. We speculate that the transition from a disordered to an ordered state is driven by the pressure from the particles in the layers above the observation plane.

In chapters 5 and 6 we study depletion induced interactions in quasi-two-dimensional colloidal systems. In chapter 5 we observe the effect of particle shape, depletant, and colloid and polymer concentration on said interactions by computing radial distribution functions. Monte Carlo simulations are run alongside the experiments in order to corroborate our findings. In chapter 6 we add a level of complexity to the problem by introducing a second colloidal system, resulting in a binary mixture which allows us to investigate depletion induced "lock and key" binding.

In chapter 7 we use optical trapping to directly measure the depletion induced attraction between lock and key particles.

We finish this work with a summary of our overall findings.

Chapter 2

Synthetic techniques and experimental methods

ABSTRACT

We describe the synthetic pathways for all the colloidal systems used in this thesis, as well as the polymer solutions. The experimental techniques are outlined, including information on confocal microscopy, light scattering and optical trapping. Finally, the routines for particle tracking are presented.

2.1 Introduction

In this chapter we present the synthetic techniques and experimental methods used throughout this thesis. We begin in section 2.2 by outlining the pathways used to synthesise both dimpled and spherical colloidal particles, and in section 2.3 we describe the methods utilised to make the polymer solutions. Section 2.4 explains sample preparation, section 2.5 gives an overview of the sample cells used during the experiments, and the experimental techniques of confocal microscopy, static light scattering and optical trapping are detailed in sections 2.6, 2.7 and 2.8, respectively. Finally, we finish by giving the algorithms for particle tracking in section 2.9.

2.2 Particle synthesis

2.2.1 Uniformly dimpled colloidal particles

Uniformly dimpled colloidal particles were made using 3-methacryloxypropyl trimethoxysilane (TPM), following Sacanna et al. [50,51], and were modified for use with confocal microscopy by incorporating rhodamine B isothiocyanate (RITC) dye [52] prior to crosslinking. All chemicals were sourced from Sigma-Aldrich unless otherwise specified, and used as received. To make the dye, RITC and 3-aminopropyltrimethoxysilane (both 9.4 mM) were added to 5.34 ml dimethylsulfoxide. The mixture was stirred on a magnetic stirring plate for 10 days under nitrogen. Next,

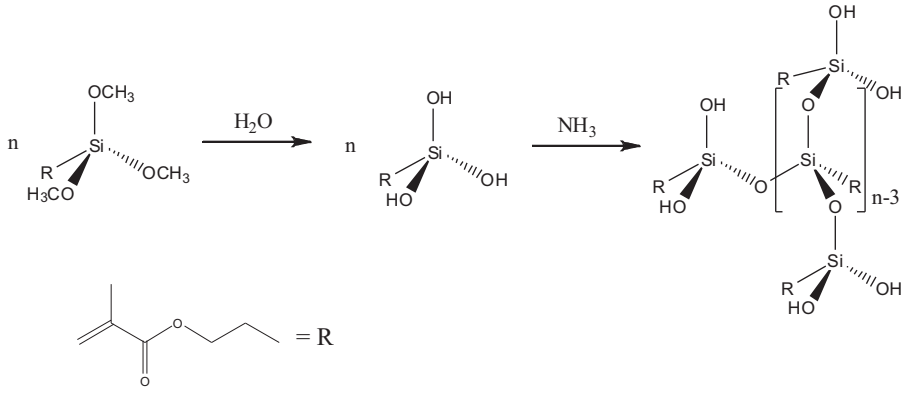

Figure 2.1: Mechanistic scheme showing the formation of the TPM droplets [51]. We first hydrolyse the TPM and then add base to catalyse the polycondensation reaction. Once formed, these droplets are crosslinked using potassium persulfate. This attacks the alkene part of the TPM oligomers.

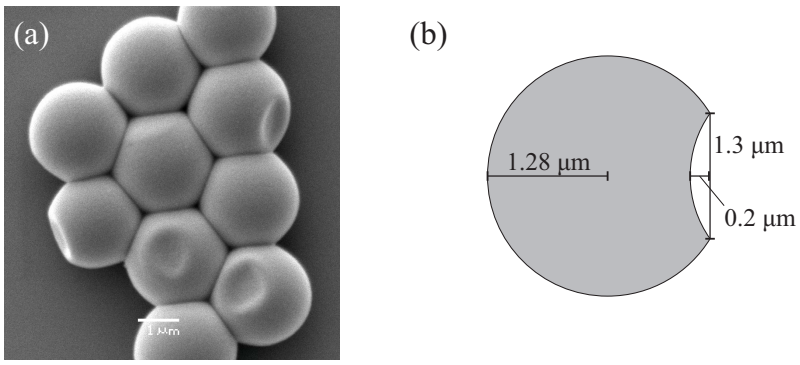

Figure 2.2: (a) Scanning electron microscopy image, and (b) dimensions of the dimpled particles.

10 ml TPM (Polysciences) was added to 100 ml deionised water and left to hydrolyse overnight with magnetic stirring. A mixture of 40 ml deionised water, 50 µl ammonium hydroxide (28% NH_3) and 200 µl TPM was left to react with slow magnetic stirring until the solution appeared cloudy and turbid. At this stage, the hydrolysed TPM (HTPM) was carefully added dropwise until the resulting droplets reached the desired size. Generally, 30-50 ml HTPM was required for this. A few drops of the RITC dye mixture were then added, along with 0.1% w/w Pluronics f108 stabiliser. 2.5 mM potassium persulfate (in powdered form) was charged to the reaction vessel, the mixture was heated to 75°C, and left with gentle stirring for up to 6 hours. Finally, the particles were washed in water by repeated centrifugation at 800 rpm. Due to the slow stirring speeds required, the dye was not evenly distributed throughout the batch of particles, resulting in some particles appearing brighter than others. This had no effect on our image analysis routines. These particles had a diameter of 2.56 µm and a polydispersity of 4%, as determined by static light scattering. The dimples were found to be approximately 1.3 µm across and 200 nm deep, as determined by scanning electron microscopy and atomic force microscopy, respectively (see figure 2.2). From these measurements we were able to calculate the radius of curvature of the dimple and found it to be 1.16 µm. The particles were stable in water due to the charged initiator residues.

2.2.2 Spherical particles

To enable the study of both the effect of non-sphericity and the lock-key mechanism (described in [50]), spherical particles were also synthesised from TPM. The method was identical to that given above, with the exception that azobisisobutyronitrile (BDH Laboratories) was used in place of potassium persulfate. The use of an oil soluble initiator, rather than a water soluble

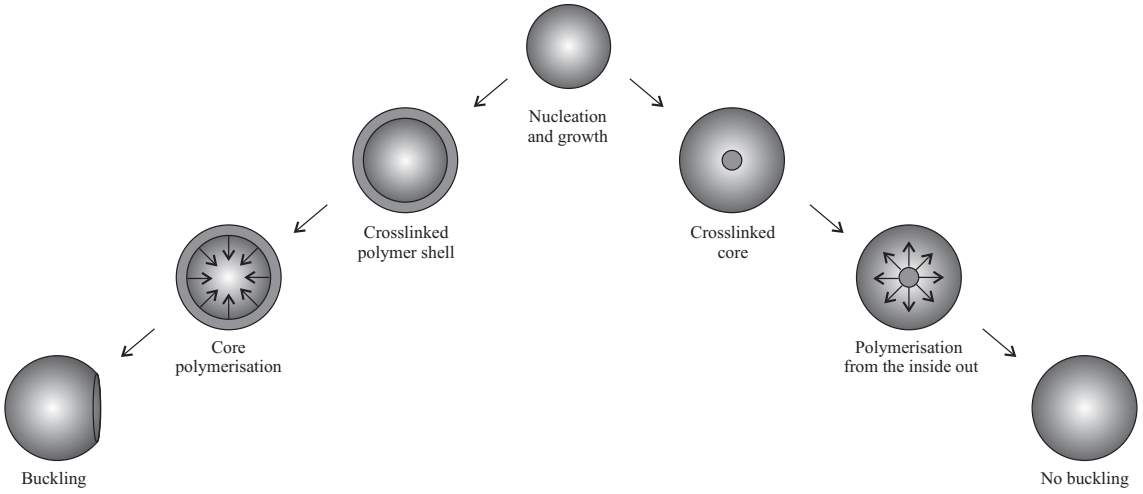

Figure 2.3: The difference between the synthesis of dimpled and spherical particles [50]. If we follow the left hand route, we see that the initiator is water soluble, and thus the crosslinking reaction begins on the outside of the droplets and we get dimpled particles. Conversely, following the right hand method gives us spherical particles, as the initiator is oil soluble, and therefore the crosslinking starts within the droplet itself.

one, meant that the crosslinking reaction began inside the particles and thus no buckling was seen (see figure 2.3). In one case, spherical particles were made from the same batch of seed droplets as the dimpled particles, and hence any effects pertaining to polydispersity should be consistent between the two samples. This allowed us to look closely at the effect of shape anisotropy on the behaviour of the particles.

A second batch consisting of smaller spherical particles was also synthesised - these were made in a similar way to the previous particles, but with two small differences: the particles were only 1.72 μm in diameter, with a polydispersity of 5%, as determined by static light scattering; and the dye used was fluoroscein isothiocyanate (FITC). The size of the particles was controlled by the amount of HTPM added after drop formation, and as such, these smaller particles were made by adding much less material in this step (approximately 5 ml compared to 30-50 ml). The FITC dye solution was made in an identical fashion to that used for the RITC dye. Scanning electron microscopy images of both batches of spherical particles are given in figure 2.4.

2.3 Polymer synthesis

Polymer solutions of both xanthan and poly(ethylene oxide) were used as a non-adsorbing depletant in chapters 5, 6, and 7. A 2 mg ml^{-1} aqueous solution of xanthan ($M_w = 3 \times 10^6$ g mol^{-1},

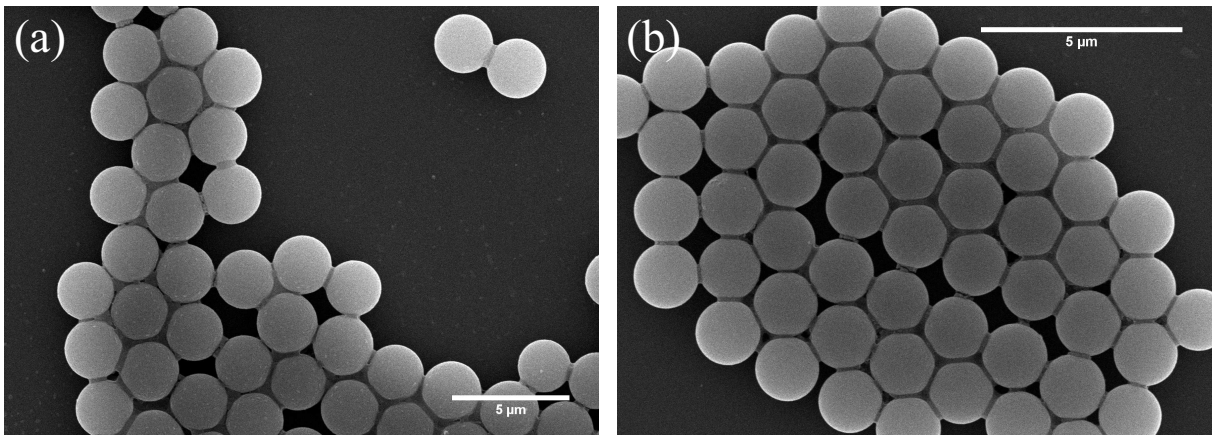

Figure 2.4: Scanning electron microscopy images of the large spherical particles (a), and the small spherical particles (b). In both cases the scale bar is 5 µm.

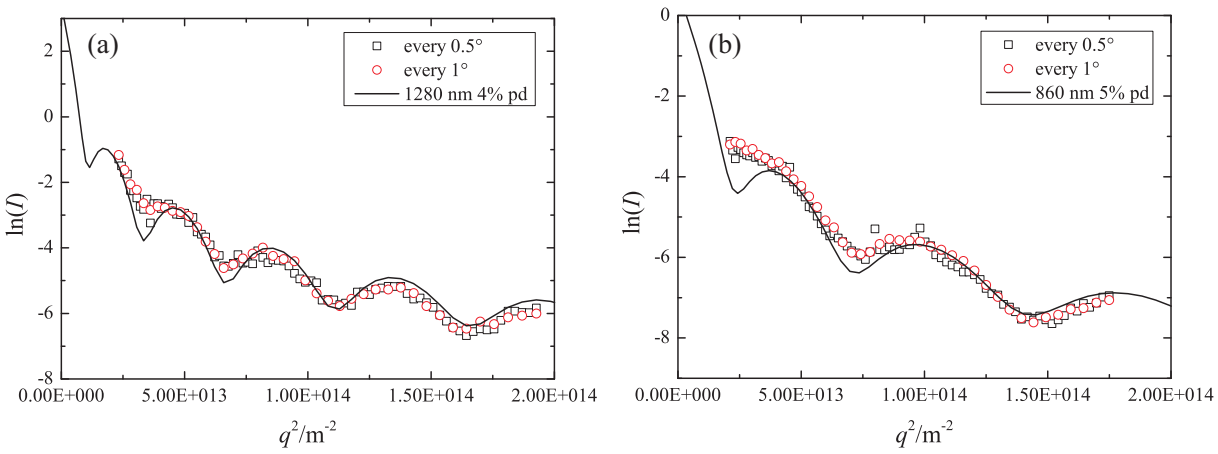

Figure 2.5: Static light scattering data for the large spherical particles (a), and the small spherical particles (b). Shown are data points measured at intervals of 1° and 0.5°. The solid lines represent a Mie theory fit of the experimental data using a spectrum generator provided by Arnout Imhof (Utrecht University).

Name	Shape	Dye	σ/μm	PD	Solvent	ρ/g cm^{-3}	n
STPM28	dimpled	RITC	2.56	4%	water	1.228 [51]	1.494
RTPM1	spherical	RITC	2.56	4%	water	1.228 [51]	1.494
RTPM2	spherical	FITC	1.72	5%	water	1.228 [51]	1.494

Table 2.1: Physical properties of the particles synthesised in this thesis. σ is the particle diameter, PD is the polydispersity of the sample, and n is the refractive index.

sourced from Aldrich) was prepared following Koenderink et al. [53]. NaCl was added at a concentration of 0.1 M in order to screen double layer repulsions, and 2 mM NaN_3 was added to prevent bacteria growth [54]. This solution was stirred and heated to 85°C. Once up to temperature, the heating was halted, and the mixture was left to stir for a further 15 hours. Using the Benoit-Doty model [55], along with the definition of contour length given by Coviello et al. [56] and the values for the persistence length and linear mass density from [53], the radius of gyration of the polymer was calculated to be 222 nm.

A polymer solution of poly(ethylene oxide) (PEO) was also synthesised. This was made by simply adding powdered PEO ($M_w = 1 \times 10^6$ g mol^{-1}, sourced from Sigma-Aldrich) to deionised water and stirring gently until completely dissolved. This took approximately 24 hours. It was not necessary to add anything to prevent bacteria growth in this case, as PEO is not a biopolymer. The radius of gyration was calculated to be 57 nm, following Shang et al. [57]. In some cases, salt was required to screen the charges in the system. Instead of adding salt to the polymer, a 0.1 M NaCl solution was added to the individual samples directly.

2.4 Sample preparation

The systems used for each experiment were prepared in small vials by combining the appropriate amounts of each stock solution with deionised water. These were then homogenised using a bench-top vortex, and the desired volume was transferred to the sample cell. The concentration of colloidal particles in each system was described using the colloid volume fraction, $\phi_c = \frac{4}{3}\pi R^3 n_c$, or in some cases the colloid area fraction, $\phi_c^a = \pi R^2 n_c h$, with R the particle radius, n_c the number density of colloidal particles, and h the height of the sample. These definitions were used for both the dimpled and spherical particles. Similarly, the polymer concentration was given in terms of the polymer volume fraction, $\phi_p = \frac{4}{3}\pi R_g^3 n_p$, with R_g the radius

of gyration of the polymer, and n_p the number density of polymers.

In order to correctly predict the sedimentation behaviour of the systems, it was necessary to consider both the gravitational length and sedimentation velocity of the particles. The gravitational length, ξ, of a particle in solution is given as [46],

$$\xi = \frac{k_{\mathrm{B}}T}{m^* g}, \tag{2.1}$$

with k_{B} Boltzmann's constant, T the temperature, m^* the buoyant mass, and g the acceleration due to gravity. The buoyant mass is further defined as $m^* = \frac{4}{3}\pi R^3 \Delta\rho$, with $\Delta\rho$ the density difference between the solvent and the particles. This length gives us an indication of the height over which gravitational energy is comparable to thermal energy, and thus allows us to determine whether sedimentation or diffusion is the more dominant process: if $\xi > R$ then Brownian motion governs the particles' behaviour and we see only a smooth concentration gradient due to gravity [54], but if $\xi < R$ then the gravitational energy is too strong, and the particles sediment completely to the bottom of the container. Assuming that the dimple had a negligible effect, the gravitational lengths were 0.2 μm and 0.7 μm for the large and small particles used in this work, respectively.

The sedimentation velocity of a particle is defined as [54],

$$v_s = \frac{m^* g}{6\pi\eta R}, \tag{2.2}$$

with η the viscosity of the sample, which here was estimated to be 10^{-3} Pa s. Substituting in the two particle radii, and once more assuming that the dimple had no effect, we found sedimentation velocities of 0.8 μm s^{-1} and 0.4 μm s^{-1} for the large and small particles, respectively.

2.5 Sample cells

In this thesis, most observations were made using either laser scanning confocal microscopy (LSCM) or bright field microscopy. Experiments that utilised LSCM were carried out in a homemade cell constructed from a small (10 mm in diameter) glass vial which had been cut in half across the width, glued onto a coverslip (with Araldite epoxy glue) and subsequently plasma-cleaned to ensure that the particles did not stick to the wall. After filling, the cell was

Figure 2.6: a) Sketch of the homemade sample cell. A small glass vial is cut across the width and glued onto a coverslip. After being filled, the cell is sealed with a lid. b) Sketch of the sample cell used for bright field microscopy. Two strips of double sided sticky tape are put onto a microscopy slide and covered with a glass coverslip.

sealed with a screw-on plastic lid (see figure 2.6(a)). This proved to be relatively air tight, as checked by recording the mass of a filled cell at the time of preparation and again after 2.5 days and finding the two measurements to be consistent.

The experiments in chapter 7 required a different cell, as the inverted bright field microscopes used meant that we still observed the sample from below, but now, the illumination source came from above. The opaque plastic lids used previously thus prevented any light from reaching the sample, and instead we required a cell that was transparent on both the top and bottom. A simple solution was to use glass capillary tubes, which were sealed and attached to a glass microscopy slide. Initially, clear nail polish was used as the sealant due to the speed at which it dried. However, it was noted that, over a period of approximately 24 hours, the dimpled colloidal particles became spherical. We hypothesised that the small amounts of nail polish present at either end of the tube reacted with the particles in some way, and caused swelling, resulting in the dimple being pushed out of the particle. To investigate this phenomenon, both UV glue (Norland optical adhesive 81) and Araldite epoxy glue were used in the place of nail polish, and the results corroborated our original thoughts: when in a tube sealed with Araldite, the particles remained dimpled, but when in contact with either UV glue or nail polish, de-

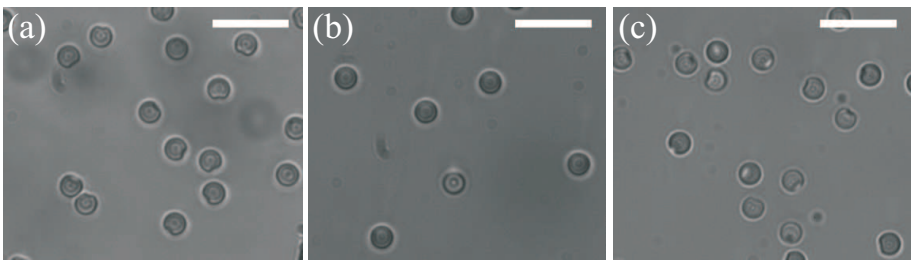

Figure 2.7: a) Dimpled particles in a capillary tube of height 0.5 mm, sealed with nail polish, immediately after sample preparation. b) The same sample, but after five hours - the particles have lost their dimples. c) The dimpled particles in a similar tube sealed with Araldite, 24 hours after sample preparation, and the dimples are still clearly visible. Scale bars are 10 μm.

dimpling occurred (see figure 2.7). Both uncured UV glue and nail polish contain acetone, and thus it was believed that acetone caused the particles to swell.

Instead of glass capillary tubes (which do not have smooth enough surfaces for good optical observation), a new sample cell was designed consisting of a microscopy slide, two strips of double-sided sticky tape, and a small (22 mm $\times$ 22 mm) glass coverslip. The strips of sticky tape allowed us to form a narrow channel into which the sample was administered using capillary action - see figure 2.6(b). These cells were sealed with Araldite to avoid de-dimpling.

2.6 Confocal microscopy

The majority of the work presented in this thesis utilised laser scanning confocal microscopy. This technique was first realised by Marvin Minsky in the 1950s [58], following his frustration at the poor signal to noise ratio when imaging neurons. He found that the optical density of the neuron cells meant that multiple scattering led to a blurred image - the same can be said for certain colloidal samples, and as such confocal microscopy is a very useful tool for observing such samples. Here, we describe the principles of confocal microscopy and its advantages over traditional bright field microscopy, using the reviews [59, 60] as a guide.

A schematic of a confocal microscope is shown in figure 2.8 [59]. Initially, laser light is passed through a pinhole to create an epitaxial point source. This light is then directed through

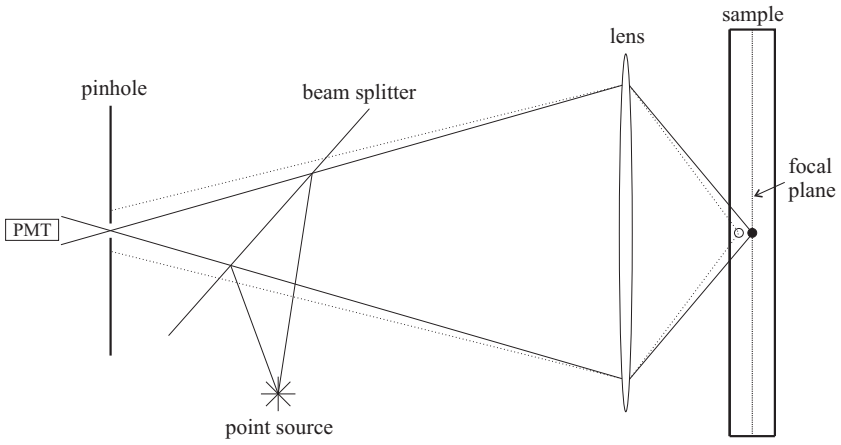

Figure 2.8: Schematic of a confocal microscope from [59]. The filled circle is in the focal plane, while the open circle is out of focus and the light coming from the latter is blocked by the pinhole.

a set of beam splitters such that the only light emerging is of an appropriate wavelength to excite the fluorescent dye in our sample. The light is directed onto the focal plane of the sample using a lens, and the resulting fluorescence passes back through the lens towards the detector (usually a photo multiplier tube, or PMT). Before reaching the detector, the light must pass through a second pinhole: this pinhole is conjugate to the focal plane of the sample and thus blocks any light originating from objects outside of this focal plane, so any out of focus light is eliminated. A two-dimensional image is obtained by scanning the focal plane of the sample, pixel by pixel. We are also able to build three-dimensional images by varying the focal depth and thus scanning different planes of the sample.

Microscopy image quality is governed by two measures: contrast and resolution, both of which are greater in confocal microscopy than in traditional bright field microscopy, and can be quantified using the point spread function (PSF) [59]. The PSF can be thought of as the probability that photons will reach a particular point, or will be received from that point [17, 59]. Before any further discussion, it is convenient to switch to optical coordinates, ρ and ζ, defined relative to the real coordinates around the optical axis, r (radial) and z (axial), as $\rho = r\,(2\pi\mathrm{NA}/\lambda)$ and $\zeta = z\left(2\pi\mathrm{NA}^2/n\lambda\right)$, respectively, with NA the numerical aperture of the objective, λ the wavelength of the light in a vacuum, and n the refractive index of the medium. The numerical aperture is defined as $\mathrm{NA} = n\sin(\alpha)$, with α half the angle of the light cone entering or leaving the objective. The PSFs for confocal microscopy are given as,

$$p(\rho, 0) = \left(\frac{2J_1(\rho)}{\rho}\right)^4, \tag{2.3}$$

in the focal plane, with J_1 the Bessel function of the first kind, and,

$$p(0, \zeta) = \left(\frac{\sin(\zeta/4)}{\zeta/4}\right)^4, \tag{2.4}$$

along the optical axis. It should be noted here that the PSFs for confocal microscopy are the squares of those for conventional microscopy as the light passes through the objective twice in the former case.

An illuminated point on the sample has the radius of the Airy disk, which is defined as the position where the PSF first has a minimum ($p(\rho_{airy}, 0) = 0$). From figure 2.9(a), we can see that the Airy disk is the same for both confocal and bright field microscopy, but that the width

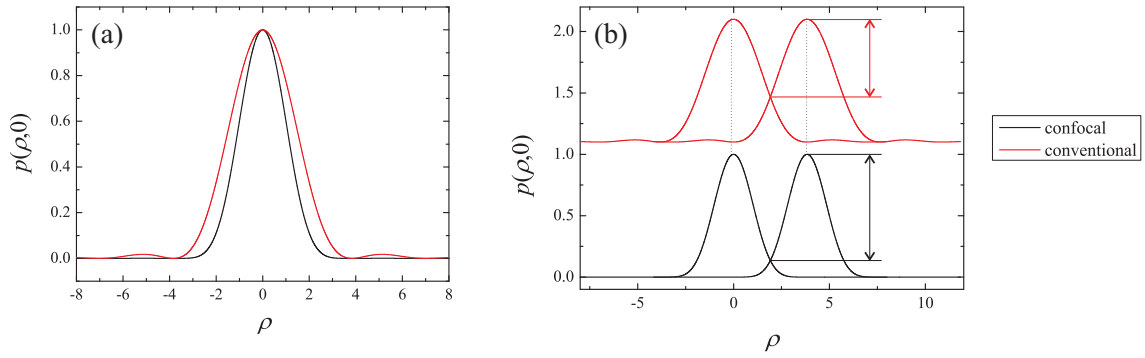

Figure 2.9: a) PSFs for both confocal (black) and conventional (red) microscopy. b) Radial PSFs for two objects separated by an Airy disk. The difference in the drop in intensity between the two maxima is indicated.

of the PSF is much narrower for the confocal case. Also, we see that the secondary maxima are much smaller in confocal microscopy. This means that the contrast is greatly improved, as the light is more contained within the central peak of the PSF. The presence of the pinhole also adds to the amelioration in contrast by preventing out of focus and scattered light from reaching the detector.

The PSF can also give us information about the resolution of a microscope: two illuminated points will only appear separate if their PSFs are far enough apart to be distinct [59]. More explicitly, the Rayleigh criterion tells us that two objects will be resolvable using a traditional microscope if they are separated by at least one Airy disk radius [61] - this corresponds to a drop of intensity of 26% between the two maxima (see figure 2.9(b)). For confocal microscopy, the drop in intensity is much larger than 26% if two points are separated by an Airy disk radius. This means that the separation required to fulfill the Rayleigh criterion is smaller and thus we are able to distinguish objects that are closer together using confocal microscopy, meaning we have increased resolution.

The confocal system used in this thesis was a Zeiss Exciter LSM 5 laser scanning confocal microscope. This contained a 543 nm HeNe laser source and was fitted with a 63× oil immersion objective, with an NA of 1.4.

2.7 Static light scattering

Particles synthesised in this thesis were characterised using static light scattering (SLS). This technique allows us to measure both the particle size and the polydispersity of the sample [62].

In static light scattering, a light source is passed through the sample and the intensity of the scattered radiation is measured at different scattering angles, θ. For each angle, we record the scattered intensity over the period of a few seconds and take the time-average, hence the "static" in the name. A schematic of the setup is shown in figure 2.10.

The scattering vector, $\mathbf{q}$, is defined as the difference between the wavevectors of the scattered and incident beams, and its magnitude is,

$$q = \frac{4\pi n}{\lambda} \sin\left(\frac{\theta}{2}\right), \tag{2.5}$$

with n the refractive index of the solvent, and λ the wavelength of the light. The angular dependence of the scattered intensity is given not only by eq. (2.5), but also by the particle shape, and we may gain further insight into the sample by fitting the detected intensities with the Mie solutions to Maxwell's equations [64, 65].

To characterise the particles synthesised in this work, extremely dilute ($< 1 \times 10^{-4}$ wt%) samples were prepared, such that no scattering could be seen by eye, and the solutions appeared clear. These were contained within stoppered glass NMR tubes, with an external diameter of 10 mm, and placed in an ALV/CGS-3 Goniometer. The light source was a 22 mW HeNe laser with a wavelength of 632.8 nm. The scattered intensities were measured at intervals of 0.5° or

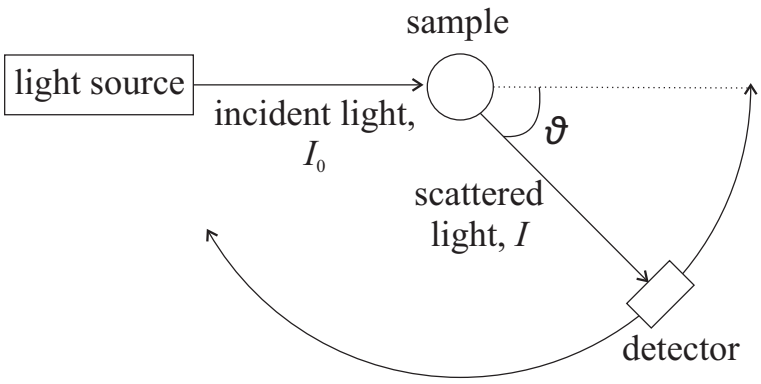

Figure 2.10: Schematic of the SLS setup [63].

1° between 20° and 60°. Particle size and polydispersity information was extracted by creating predicted spectra (with a program written by Arnout Imhof (Utrecht University) - see figure 2.5) using the same refractive index as the sample and varying the particle size and polydispersity, until good agreement with the experimental spectra was seen.

2.8 Optical trapping

In 1970, Arthur Ashkin first observed the acceleration and trapping of particles using the radiation pressure from a beam of light [66]. He found that an object suspended in a medium of lower refractive index would be drawn into the beam axis of a weakly focused laser beam, and would simultaneously be accelerated in the direction of the beam. In later work, he used gravity to balance the radiation pressure of the laser in order to levitate particles [67], and finally, in 1986, Ashkin et al. created the first single-beam gradient force optical trap, where a strongly focused laser beam was used to trap a particle in three dimensions [68]. Since then, optical traps have been widely used in many different fields from biology to physics [69–73].

The basic principles behind optical trapping are as follows [12, 74]. A 3D potential energy well is created by strongly focusing a beam of laser light through an objective lens with a high numerical aperture. Provided that there is a refractive index mismatch between the particle and the surrounding medium, the particle can be trapped in this energy well. Depending upon the ratio between the particle radius, R, and the wavelength of laser light, λ, we can further describe the theory behind optical trapping by considering three possible regimes: the Rayleigh regime, where $R \ll \lambda$; the Mie regime, where $R \approx \lambda$; and the ray optics regime, where $R \gg \lambda$. In the work done in this thesis, we are, strictly speaking, in the Mie regime, as $R \approx \lambda$. However, in the Rayleigh and ray optics regimes, the physics behind optical trapping can be explained by a simple force argument, but the same cannot be said of the Mie regime [75, 76]. As such, for the purposes of giving an insight into the working of optical trapping, we use the ray optics regime as a basis [77].

A schematic of a particle being held in an optical trap created by a Gaussian laser beam is shown in figure 2.11. As the laser light hits the particle, the rays are refracted due to the difference in refractive index between the particle and the surrounding medium. The light beams therefore change direction, meaning that there is a change in the momentum of the light. There

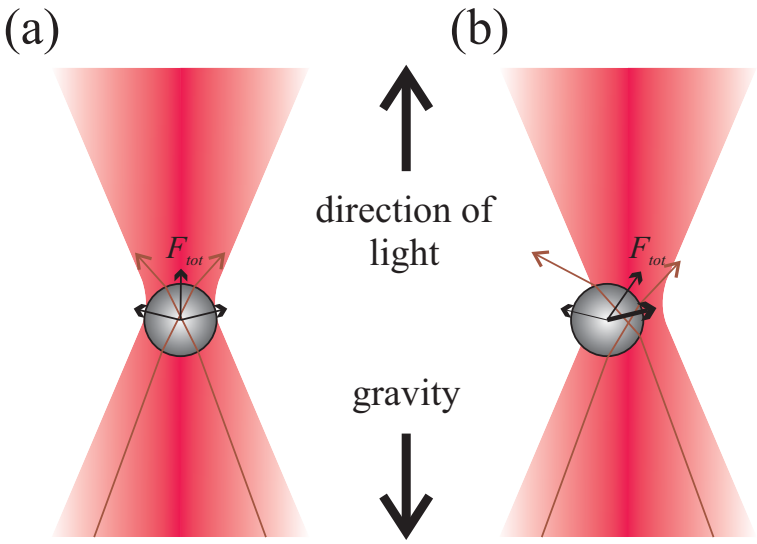

Figure 2.11: Schematic of particle being held in an optical trap. In (a), the particle is in the centre of the beam and so does not feel any restoring force. In (b), the particle is off axis; the higher intensity light towards the middle of the laser beam causes a greater momentum change and so the net force on the particle is towards the centre.

is an additional momentum change caused by reflection of light off the particle surface. These changes must be balanced by a momentum change in the particle, corresponding to a force being felt by the particle. For a particle that is held centrally in a trap (figure 2.11(a)), the sum of the optical forces results in the particle remaining in the centre and being pushed slightly in the direction of propagation of light. If, on the other hand, the particle is to one side of the optical axis (figure 2.11(b)), the optical forces act to pull the particle to the trap centre. Due to the Gaussian profile of the laser beam, the rays nearest the centre of the trap have a higher intensity than those at the edges, and thus make a greater contribution to the optical force, resulting in the particle being drawn to the highest light intensity in the centre of the trap. Provided the sum of the optical forces matches that from the effective particle weight, the particle will be trapped in 3D.

The discussion above considers an isotropic spherical particle, but the work presented here used a spherical particle with a well-defined dimple. In this case, an optical trap will not only fix the translational coordinates of the particle, but will also control the orientation to some extent. The strongest forces will be generated when the laser light passes through the particle along the optically thickest axis, as this results in the maximum change in momentum. As such, the dimpled particles will orient themselves such that the dimple is perpendicular to the laser beam.

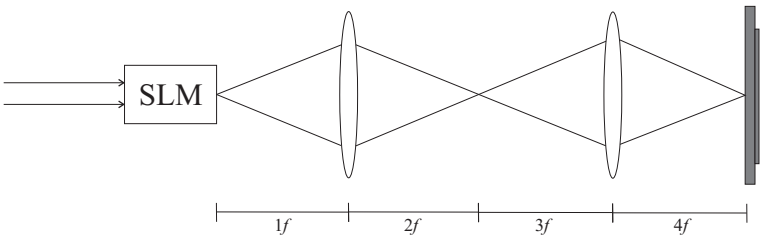

Figure 2.12: Schematic of the $4f$ setup used in this work. The light travels four focal lengths from the SLM to the back aperture of the sample objective, via two lenses, hence the name.

The experimental system used in this work was based upon a standard $4f$ setup (see figure 2.12), combined with an optical microscopy system (see figure 2.13) [78]. The laser light had a wavelength of 1064 nm, and the optical traps were generated using a spatial light modulator (SLM). An SLM allows us to digitally create specific diffraction gratings, which in turn generate multiple traps and hence we can hold more than one particle in place at a time [79–81]. A visible light dichroic mirror was used to allow the laser light to reach the sample in order to trap the particles, while reflecting the visible light from the LED to allow the sample to be imaged onto

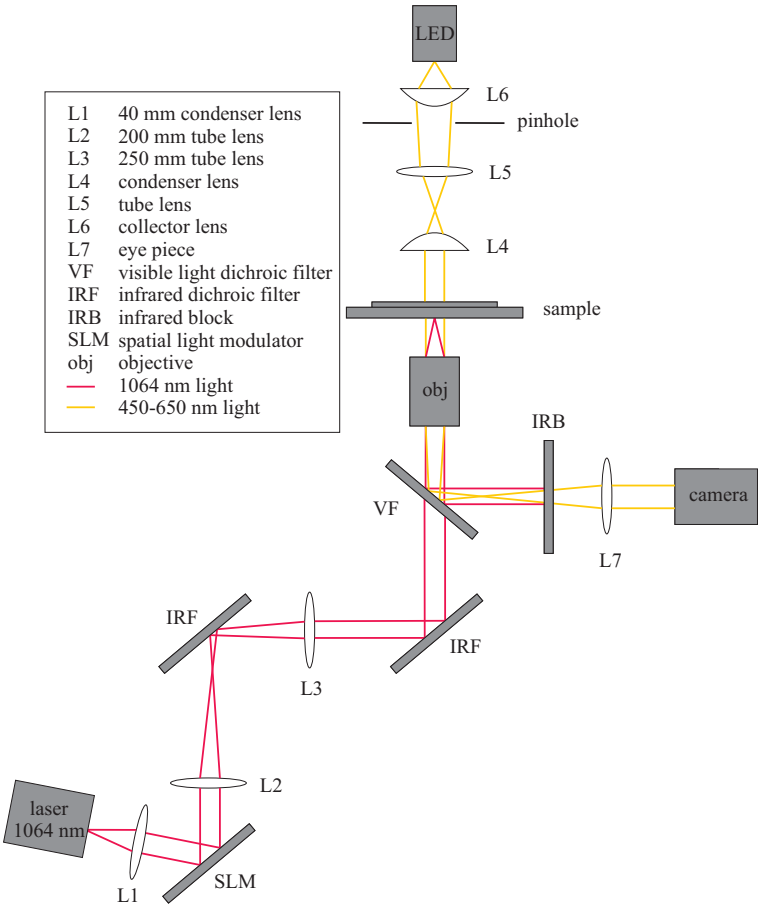

Figure 2.13: Diagram of the optical trapping setup.

the camera. An infrared block was also used just before the camera to remove any remaining laser light.

2.9 Particle tracking

In all the work within this thesis, it was necessary to locate the centre of each particle in order to analyse, both qualitatively and quantitatively, the order and structural behaviour of our systems. To do this, two image analysis routines were written: one in IDL (Interactive Data Language), following Crocker and Grier [82], and one in Mathematica, following McLoone [83]. It should be noted that these routines are optimised for truly circular objects, but still work within the accuracy required for the anisotropic particles used in this work. The outputs from the two separate routines were similar, and which one to use was decided by overlaying the tracked centres onto the experimental images and finding the best match. We begin by describing the IDL routine, which was used for the analysis in chapters 4 and 6 (figure 2.14).

2.9.1 IDL routine

The experimental data was split into individual frames, and each frame was read into the program sequentially. A bandpass filter, "bpass", was then applied, which smoothed the images and removed any small artifacts. Next, the coordinates of all the features in the image were located, using "feature", which identified the roughly circularly symmetric objects using a Gaussian mask. The particles were selected from this list of features by adding constraints to the brightness and size. Finally, a cut-off was added to ensure that no two particles were found to be closer than the measured particle diameter.

In chapter 4, not only did we require the particle coordinates, but we also wanted to identify those particles whose dimple was facing down towards the bottom of the cell. The dimples appeared as dark spots in the centres of the particles, and were thus located using similar routines to those described above, but now, the images were inverted first such that the dimples became bright spots on a dark background.

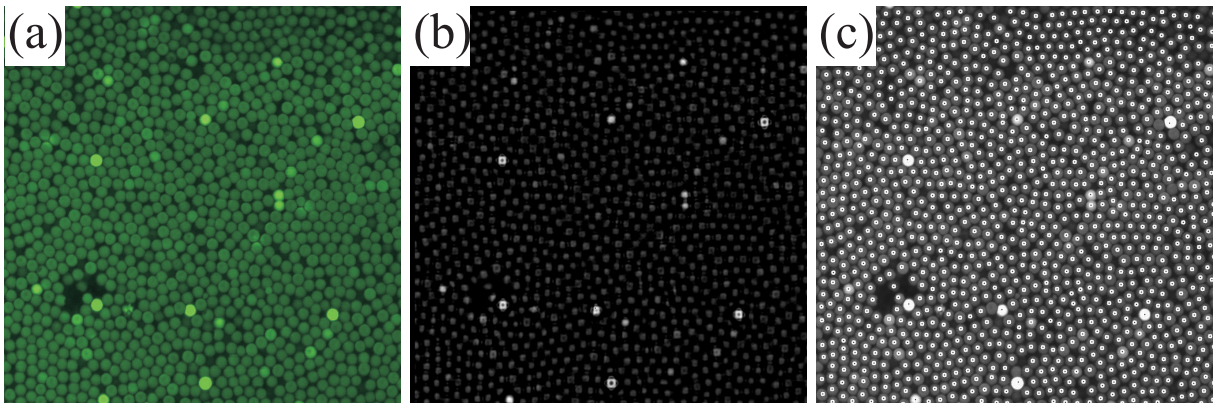

Figure 2.14: An example of the IDL particle tracking routine. (a) shows the experimental snapshot and (b) illustrates the effect of the bandpass filter. (c) gives the tracked particles.

2.9.2 Mathematica routine

In chapter 5 we tracked the coordinates of our particles using a routine written in Mathematica (figure 2.15). Again, the experimental data was read in frame by frame. The images were

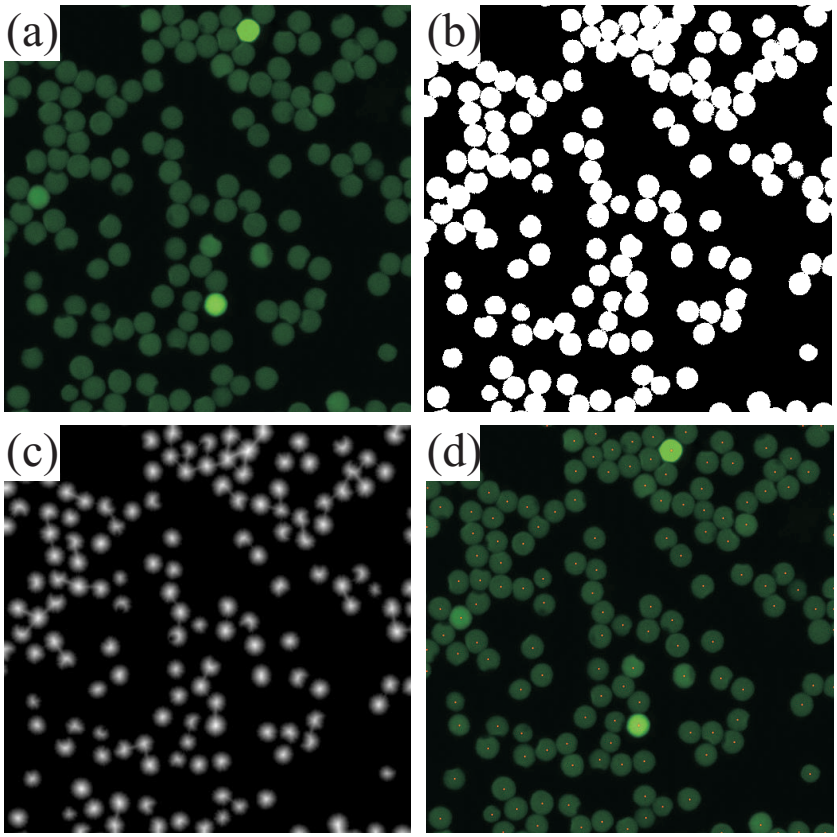

Figure 2.15: An example of the Mathematica particle tracking routine. (a) shows the experimental snapshot which is then binarised and cleaned up (shown in (b)). (c) gives the output from the distance transform, and (d) shows the tracked particles.

converted to binary, and then cleaned up by deleting any components that were smaller than 5 pixels. Next, to find the centres of the particles, we applied a "distance transform", which converted the value of each pixel to the distance of that pixel from the nearest background pixel. Taking the local maxima of this and using the in built command, "ComponentMeasurements" allowed us to pinpoint the centre of each particle. To improve accuracy and avoid any unexpected points, we deleted any coordinates that were closer than 20 pixels, as no two particles could physically be this close together.

Acknowledgements It is a pleasure to thank Stefano Sacanna for continual guidance with the particle synthesis, and Lia Verhoeff and Robert Jacobs for helping with the SEM imaging and AFM, respectively. Michael Juniper and Colin Reynolds are thanked for advice on particle tracking, and Arran Curran is thanked for help with optical trapping.

Chapter 3

Monte Carlo simulations

ABSTRACT

Monte Carlo simulations are used in this work to model and help interpret experiments. In this chapter, a brief history of the origins of the Monte Carlo technique is provided, as well as the details of the specific algorithm used later in this thesis.

3.1 Introduction

Monte Carlo methods were first developed at Los Alamos by Metropolis et al. in 1947, although it is thought that they were independently invented by Fermi almost 15 years earlier [84,85]. This class of stochastic simulation gets its name from its use of random numbers and probabilities, similarly to the roulette wheels used in the casinos of Monaco. In 1953, Metropolis, Rosenbluth, Rosenbluth, Teller and Teller presented the first Monte Carlo simulation of a molecular liquid, and simultaneously introduced the idea of the so-called Metropolis method [86]. This technique incorporates importance sampling with the ability to accept or reject trial moves based solely on the relative probabilities of visiting different points in configuration space, rather than needing to know the absolute probabilities. Both of these processes allow us to gain more information for less computational power and are succinctly explained in more detail by Frenkel and Smit in [87].

Monte Carlo simulations are a useful tool for experimentalists and theorists alike. They allow experimentalists to sample the available parameter space more readily and perform targeted experiments in which the results are expected to be particularly enlightening. Additionally, they allow studies that are not experimentally feasible to be performed. For theorists, simulations provide a platform upon which novel theories may be tested.

Considerable attention has been given to simulating the phase behaviour of hard spheres in bulk [88, 89], and as such this is now thought to be relatively well understood [90]. More complex systems introduce the presence of extra parameters such as boundaries [91], interactions [92,93] or shape anisotropy [94–99]. Whilst all three of these complications are pertinent to the systems explored in this thesis, of particular relevance are simulations examining the effect of the depletion interaction caused by the introduction of polymers or additional small colloidal particles to a colloidal suspension of anisotropic particles [100].

3.2 Algorithm details

Monte Carlo simulations of the experimental systems described in chapter 5 were carried out, treating the colloidal particles as hard, and the polymers as penetrable hard spheres. Using hard

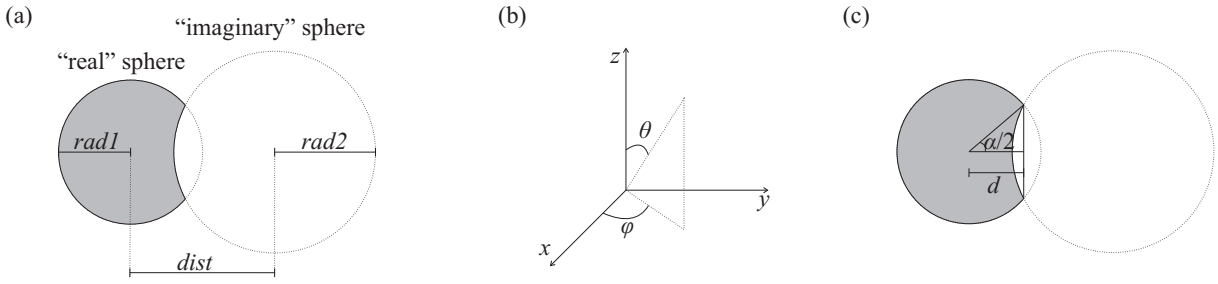

Figure 3.1: (a) Illustration of the description of the dimpled particles. A "real" sphere of radius *rad1* is positioned a distance *dist* away from an "imaginary" sphere of radius *rad2*. The shaded area shows the resultant particle shape. (b) Definitions of the coordinate system used. (c) Definitions of d and α.

particles as a model system allows us to set the interaction potential to be infinite if the distance between two particles, r, is less than a particle diameter, and 0 otherwise. This simplifies the acceptance criteria and means we reject a move only if there is particle-particle overlap. Treating the polymers as penetrable hard spheres means that a polymer may not overlap at all with a colloidal particle or wall, but may overlap fully with another polymer. This model was first introduced by Vrij [49].

The dimpled colloidal particles are described by the intersection of a "real" sphere with an "imaginary" one (figure 3.1(a)), in a similar fashion to the work done in [94, 95, 100]. This allows us to tune the shape of the particles to quite a large degree, as we can alter the radii of both spheres, as well as the distance between their centres. We define the position of each colloidal particle using the three coordinates (x_{real}, y_{real} and z_{real}) of the centre of the real particle, and the two angles (θ and ϕ) describing the relative orientation of the imaginary particle (figure 3.1(b)). The coordinates of the centre of the imaginary particle are then given as,

$$\begin{aligned} x_{imaginary} &= x_{real} + dist \sin\theta \cos\phi \\ y_{imaginary} &= y_{real} + dist \sin\theta \sin\phi \\ z_{imaginary} &= z_{real} + dist \cos\theta, \end{aligned} \tag{3.1}$$

where *dist* is the distance between the centre of the real sphere and that of the imaginary sphere. We attempt to match the relative size and shape of our simulated particles to those in our experimental studies, and the parameters used to describe this, as well as the simulation conditions, are given in table 3.1. To allow us to replicate the quasi-2D confinement enforced by

Parameter	Value
boxsize	20.0
box height for polymers, h	3.0
radius of real sphere, *rad1*	1.0
radius of imaginary sphere, *rad2*	1.0
distance between real and imaginary spheres, *dist*	1.76
radius of polymer, *radp*	1.0
number of equilibration steps	10^5
number of steps	10^5
binsize for $g(r)$ calculations	0.1

Table 3.1: Simulation parameters. The number of steps given here is the average number of steps each particle takes.

gravity in the experiments, we apply periodic boundary conditions in the x and y directions, but implement solid boundaries in the z direction, giving a cell with a height of just a few particle diameters for the polymers, and approximately one particle diameter for the colloidal particles (figure 3.2). Before any measurements are recorded, the system undergoes ($10^5 \times$number of particles) Monte Carlo steps (see table 3.1) to ensure that equilibrium has been reached. This is checked by computing a radial distribution function both immediately before and after the steps contributing towards the measurements are taken, and comparing the two. These are found to be similar (figure 3.3), and thus we confirm that equilibrium is attained.

The first stage of each Monte Carlo step requires particle selection. A particle is chosen at random and may be either a colloidal particle or a polymer. We first describe the algorithm used for a colloidal particle move.

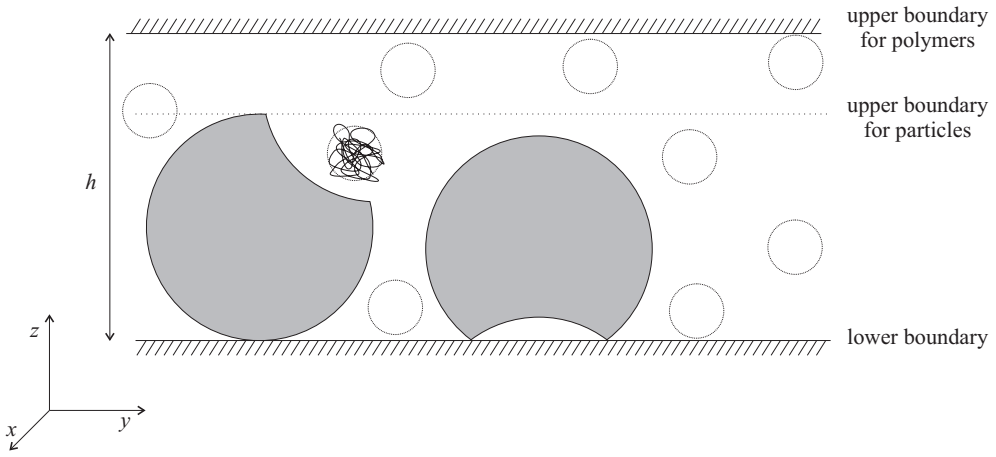

Figure 3.2: Diagram showing the simulation box used. The dimpled colloidal particles are shown in grey, and the polymers are represented by the dotted circles. A cartoon of a polymer chain is added to demonstrate that the polymers are not actually spherical, but are modelled as such.

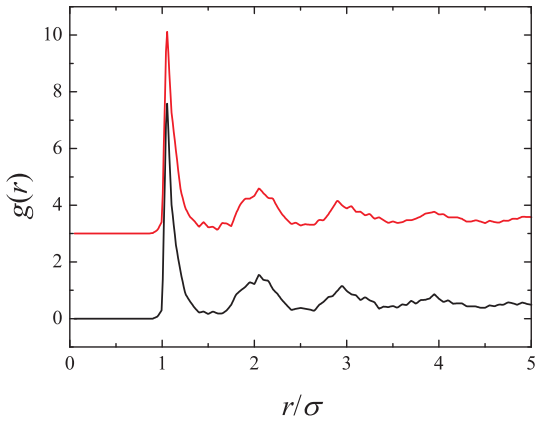

Figure 3.3: Radial distribution functions computed before (black) and after (red) the steps contributing towards the measurements are taken. Simulations were run 10 times for a colloidal volume fraction of 0.5 and a polymer volume fraction of 1, and the average $g(r)$ was calculated. Graphs have been vertically shifted for clarity; σ is the particle diameter.

3.2.1 Moving a colloidal particle

Once a colloidal particle has been selected, we generate new values of x, y, z, θ and ϕ following the general rule,

$$\text{new value} = \text{old value} + \Delta(rand - 0.5), \tag{3.2}$$

where Δ is the maximum step size (specified separately for x and y, z, and θ and ϕ), chosen such that approximately 50% of steps are accepted, and $rand$ are random numbers uniformly distributed between 0 and 1. To simplify matters, we only allow θ_{new} values between 0 and π, and ϕ_{new} values between 0 and 2π. The new position of the imaginary sphere is given using the relationships presented in eq. (3.1). Two overlap checks must then be carried out for each Monte Carlo step: particle-boundary overlap, and particle-particle overlap. The former is considerably more straight-forward than the latter, but before we are able to describe either check, we must present several definitions (see figure 3.1(c)). d is the distance from the centre of the real sphere to the chord of intersection of the real and imaginary spheres, and α is the angle of opening of the dimple. These are explicitly defined as,

$$d = \frac{dist^2 - rad2^2 + rad1^2}{2dist} \qquad \text{and} \qquad \alpha = 2\arccos\left(\frac{d}{rad1}\right). \tag{3.3}$$

As stated previously, we confine the colloidal particles in the z direction, and as such, the

move is rejected immediately if the new z coordinate is less than d or more than $2rad1 - d$. We must then carry out a further particle-boundary overlap check if $d \leq z_{new} < rad1$. In this case, the move is rejected unless the particle has the correct orientation such that it does not pass through the bottom wall of the simulation cell. An easy way to do this is to reject any move that results in $\theta_{new} + \frac{\alpha}{2} < \pi$. However, this is not quite subtle enough, and we must further discard any moves that result in $z_{new} + rad1 \sin\left(\frac{\pi}{2} - \frac{\alpha}{2} - \theta\right) < 0$.

Next, we move onto the particle-particle checks. These closely follow those given in [95], but with some amendments as our particles are thicker than hemispheres. We consider each particle as two separate surfaces: that formed from the real sphere (convex), and that from the imaginary sphere (concave). If either of these two surfaces from one particle (i) overlaps with either of the two surfaces of another particle (j) then we must reject the move, meaning that four checks are required for each particle, as well as two particle-polymer checks. We begin by describing the algorithm used for checking one real surface with another, and then proceed to explain any differences in the remaining overlap checks. Each check may be broken down into three distinct steps.

1. To start, we look at the surfaces of the full spheres, and see whether an intersection between the surfaces exists or not. For an intersection to exist, $|R_i - R_j| < r_{ij} \equiv |\mathbf{r}_j - \mathbf{r}_i| < R_i + R_j$, with R_i and R_j the radii of the two particles being checked, r_{ij} the distance between the centres of the two particles, and $\mathbf{r}_i$ and $\mathbf{r}_j$ the position vectors of the particles. In the case of our real-real checks, $R_i = R_j = rad1$. If the two spheres' surfaces do not intersect, then there is no overlap and we accept the move. Otherwise, we must proceed to the next step.

2. Next, we look at the intersection between a particle surface and the surface of a full sphere. We must do this for both particles involved in the check, i.e. surface i with full sphere j, as well as surface j with full sphere i. We describe the relative positions and orientations of the two surfaces concerned using three angles (figure 3.4):

$$\cos\phi_{ij} = \frac{R_i^2 - R_j^2 + r_{ij}^2}{2r_{ij}R_i} \tag{3.4}$$

$$\cos\omega_{ij} = \frac{\mathbf{u}_i \cdot \mathbf{r}_{ij}}{r_{ij}} \tag{3.5}$$

$$\cos\theta_i = \frac{dist^2 - rad2^2 + rad1^2}{2dist \cdot rad1} \tag{3.6}$$

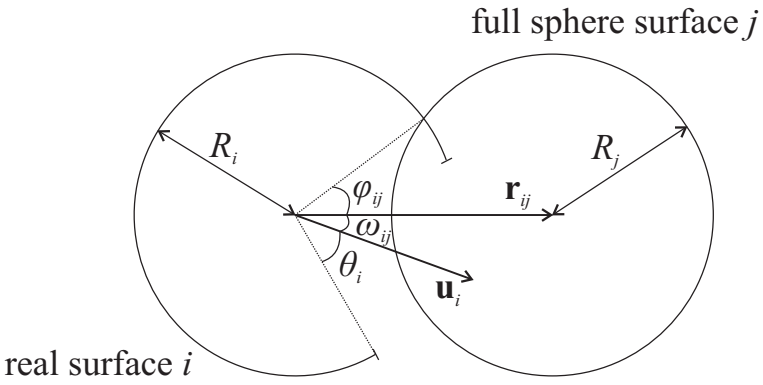

Figure 3.4: Diagram illustrating the angles and vectors required for the first two steps of the overlap checking algorithm. The particle surface of i and the full sphere surface of j are shown, but the same quantities are required for the combination of the particle surface of j and the full sphere surface of i. $\mathbf{r}_{ij}$ is in the plane of the page.

with $\mathbf{u}_i$ the orientation unit vector that goes from the centre of the real sphere to the centre of the imaginary sphere making up particle i. We find that an intersection exists if,

$$|\omega_{ij} + \zeta\phi_{ij}| > \theta_i, \tag{3.7}$$

for $\zeta = 1$ or -1. The intersection between the surface of one particle and the full sphere surface of the other is an arc, and forms part of the circle of intersection between the two spheres. If eq. (3.7) holds for both $\zeta = 1$ and $\zeta = -1$, then this arc is actually a full circle, and we have complete overlap, meaning we must reject the move immediately. On the other hand, if eq. (3.7) is not satisfied for either particle i or particle j (meaning that the arcs do no exist), then there is no overlap and we can accept the move. Finally, if the arcs exist for both particles, but neither is a full circle, then we must continue to the last step of the checking algorithm.

3. In the last step of the algorithm, we check to see whether the two arcs overlap. If so, there must be particle-particle overlap, and the move is rejected. In order to decide whether the arcs overlap or not, we require that two further angles are defined (figure 3.5):

$$\cos\alpha_{ij} = \frac{\mathbf{u}_i^{\perp} \cdot \mathbf{u}_j^{\perp}}{|\mathbf{u}_i^{\perp}||\mathbf{u}_j^{\perp}|} \tag{3.8}$$

$$\cos\gamma_i = \frac{-(\cos\theta_i - \cos\phi_{ij}\cos\omega_{ij})}{\sin\phi_{ij}\sin\omega_{ij}}, \tag{3.9}$$

where $\mathbf{u}_i^{\perp} = -\mathbf{u}_i - (\mathbf{r}_{ij} \cdot -\mathbf{u}_i)\,\mathbf{r}_{ij}/r_{ij}^2$, and expressions subscripted with a j are equivalent

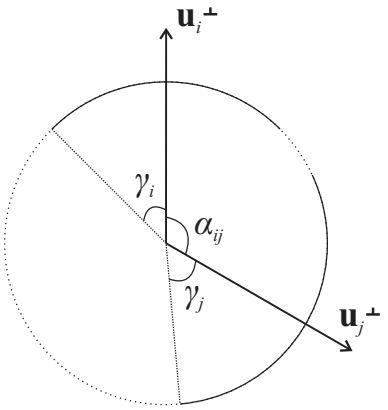

Figure 3.5: Diagram showing the angles and vectors required for step three of the overlap checking algorithm. The dashed circle is the circle of intersection of spheres i and j. The solid lines show the arcs for i and j. $\mathbf{r}_{ij}$ is now perpendicular to the plane of the page.

to those with an i, but for the other particle. There is an overlap between the arcs, and we therefore reject the move, if,

$$\alpha_{ij} < \gamma_i + \gamma_j. \tag{3.10}$$

The inequalities presented in eqs. (3.7) and (3.10) may be evaluated using cosines and sines alone, after performing some simple trigonometry. This means that inverse cosines need not be found [30, 101], saving valuable computing time.

Having discussed the method used for checking two real surfaces, we now move on to describe the differences between the algorithm above and the techniques used for checking the remaining overlaps. When the surface that we are considering is that from the imaginary sphere, there are some slight alterations to the definitions given above. Equation (3.5) becomes,

$$\cos\omega_{ij} = \frac{-\mathbf{u}_i \cdot \mathbf{r}_{ij}}{r_{ij}}, \tag{3.11}$$

and eq. (3.6) is modified to,

$$\cos\theta_i = \frac{dist^2 - rad1^2 + rad2^2}{2dist \cdot rad2}. \tag{3.12}$$

We must also change eq. (3.7), the criteria for the presence of an intersection, and this becomes,

$$|\omega_{ij} + \zeta\phi_{ij}| < \theta_i. \tag{3.13}$$

	$\cos\omega_{ij}$	$\cos\theta_i$	step 2 check	$\cos\gamma_i$
real	eq. (3.5)	eq. (3.6)	eq. (3.7)	eq. (3.9)
imaginary	eq. (3.11)	eq. (3.12)	eq. (3.13)	eq. (3.14)
real (alt.)	eq. (3.11)	cos of eq. (3.15)	eq. (3.13)	eq. (3.9) using eqs. (3.5) and (3.6)

Table 3.2: Summary of the changing definitions for the three different scenarios: a normal real surface, a normal imaginary surface, and an "alternative" real surface.

Finally, when using the surface of the imaginary sphere, we must alter eq. (3.9) to,

$$\cos\gamma_i = \frac{\cos\theta_i - \cos\phi_{ij}\cos\omega_{ij}}{\sin\phi_{ij}\sin\omega_{ij}}. \tag{3.14}$$

Other than the changes listed immediately above, the overlap algorithm for checking two surfaces from imaginary spheres is identical to that for two real surfaces. However, further alterations are introduced when we consider the overlap between one real surface and one imaginary surface. In this case, after ensuring that an intersection between the full sphere surfaces exists, we must calculate the distance between the two real spheres. If this distance is found to be greater than or equal to *dist* then we may use the same method as above, being certain to use the correct definitions for the real and imaginary surfaces. Otherwise, we must employ an alternative technique, as detailed below.

We retain the standard algorithm for the imaginary surface, but change the definitions used for the real surface. Now, we use eq. (3.11) in place of eq. (3.5), and θ_i is found from eq. (3.6) using,

$$\theta_i = \pi - \theta_i^{real}, \tag{3.15}$$

where θ_i^{real} is θ_i from eq. (3.6). We then use eq. (3.13) as the criterion for an intersection to exist. If step three of the checking process is required, we use eq. (3.9) to define γ_i, but take the values of $\cos\omega_{ij}$ and $\cos\theta_i$ from eqs. (3.5) and (3.6). A summary of the various definitions used is given in table 3.2.

The final overlap checks required when a colloidal particle is moved are between the particle and a polymer. There are two of these checks, as we must consider both the real and imaginary surfaces of the colloidal particle. Both of these checks follow the same format, and differ only because of the different definitions used for real and imaginary surfaces (see above). As in the

case of the particle-particle checks, we first measure the distance between the centres of the particles of interest, $r_{ij} \equiv |\mathbf{r}_i - \mathbf{r}_j|$. The move is immediately rejected if $r_{ij} < |R_i - R_j|$, and, similarly to the particle-particle cases, further checks are required if $|R_i - R_j| < r_{ij} < R_i + R_j$. If additional checks are needed, we follow step two given previously, and find $\cos\phi_{ij}$, $\cos\omega_{ij}$ and $\cos\theta_i$ (using eq. (3.4), (3.5), (3.6) or eq. (3.4), (3.11), (3.12)), but only for the colloidal particle, and not the polymer. We then use eq. (3.7) (for the real surface) or eq. (3.13) (for the imaginary surface) to determine if there is overlap, but now the conditions are slightly altered: if the inequality holds for either $\zeta = +1$ or $\zeta = -1$, we reject the move.

3.2.2 Moving a polymer particle

The overlap checks required when a polymer particle is moved are far simpler than those needed when a colloidal particle is selected. Again, we begin each step by generating trial coordinates for the selected particle in a similar fashion to that shown in eq. (3.2), but we use a different value for Δ. Next, we ensure that the polymer is not coincident with the boundaries put in place in the z direction, and as such the move is rejected if the new z coordinate is less than the polymer radius, $radp$, or greater than $h - radp$, where h is the cell height for the polymer particles (figure 3.2). Finally, we check the polymer-particle overlap in an identical fashion to that described at the end of section 3.2.1.

The effectiveness of our algorithm is demonstrated in figure 3.6. A dimpled particle, with

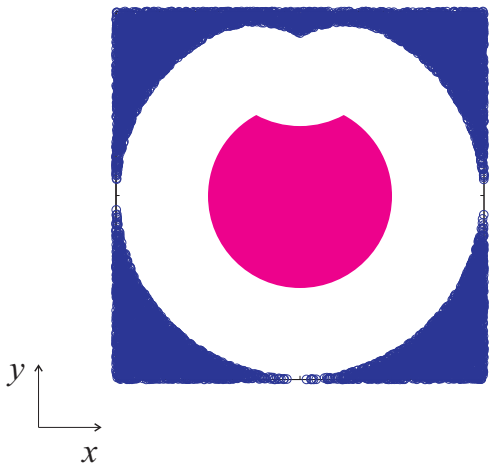

Figure 3.6: Central slice through the xy plane showing the allowed positions of spherical particles around a fixed dimpled particle.

fixed position and orientation, is placed within a small box, while spherical test particles (whose radii are equal to that of the dimpled particle) are inserted into the box. The coordinates of any particle whose position is accepted are recorded and plotted. Figure 3.6 shows the central slice in the xy plane.

Figure 3.7 gives an example snapshot of a system of dimpled particles with polymer after all steps have been completed. Polymer is shown in red and can be seen to have separated somewhat from the colloidal particles, shown in green.

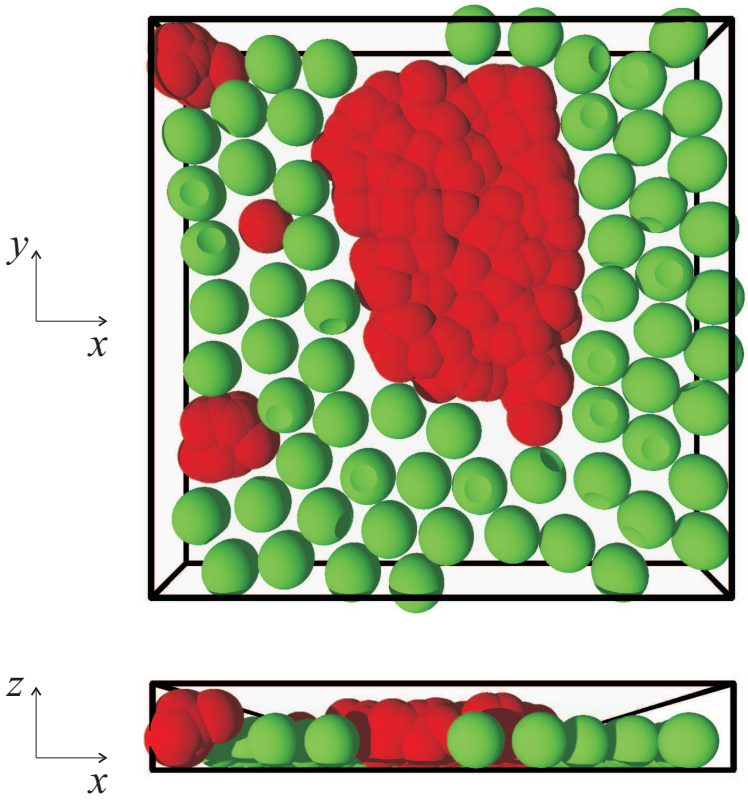

Figure 3.7: Example snapshot of a system of dimpled particles with polymer after all steps have been completed. Polymer is shown in red, and colloidal particles are in green.

Acknowledgements It is a pleasure to thank Matthieu Marechal for guidance with the overlap algorithm.

Chapter 4

Emerging structural disorder in a suspension of uniformly dimpled colloidal particles

ABSTRACT

We study the behaviour of uniformly dimpled colloidal particles in the vicinity of a featureless wall. We use laser scanning confocal microscopy to observe the structures that form in the first layer at the wall for both dimpled colloidal particles and their spherical counterparts. We show that there are notable differences in both the translational and orientational order between the two types of particle. The work illustrates how a small, uniform perturbation in the shape of a particle can lead to disordered structures that develop over time.

4.1 Introduction

The behaviour of anisotropic colloidal particles has received considerable attention recently. Particles whose shapes deviate from spherical demonstrate interesting effects in systems with hard interactions; for example, colloidal bowls displayed various stacked phases [94,95], pentagonal platelets demonstrated frustrated rotator crystals [102], and glasses of anisotropic particles (dicolloids and tricolloids) showed multiple relaxation pathways [103]. The study of such non-spherical particles has become possible by the development of a variety of synthetic techniques. These allow for the production of an extremely wide range of particle shapes including bowls [104], colloidal "molecules" [20] and ice-cream cones [105]. See references [19,23,25–27,29] for recent reviews.

Boundary conditions are known to have a strong effect on the ordering of colloidal particles. The behaviour of spherical particles against both flat [106] and structured boundaries [107–110] has been studied, but far less attention has been given to non-spherical particles at walls. These boundaries amplify the effect of non-sphericity; for example, randomly anisotropic "polyhedral" particles, with a shape polydispersity of 12%, showed signatures of hexatic structure, whereas equivalent spherical particles remained crystalline [111].

In this chapter, we consider the behaviour of uniformly anisotropic colloidal particles, whose shape differs subtly from that of a sphere by the inclusion of a well-defined dimple. Similar particles have been studied in confinement in wedge-shaped cells [112], and through multi-layer deposition [113]. Here, we probe the effect of non-sphericity on particle ordering at a single structureless wall by comparing to an equivalent system of spherical particles. We follow how the disorder in the systems develops over time to gain an insight into the mechanism through which the particles relax and reorient themselves.

We will start by describing the experimental details in section 4.2. In section 4.3 we will present and discuss our results, and we will conclude in section 4.4.

4.2 Experimental details

In this chapter we use both the spherical and dimpled particles described in chapter 2. Both particles had a diameter of 2.56 μm and a polydispersity of 4%, as determined by static light scattering. The dimples were found to be approximately 1.3 μm across and 200 nm deep, as determined by scanning electron microscopy and atomic force microscopy, respectively.

In order to observe the structural behaviour of the colloidal particles, samples with a volume fraction $\phi_c \approx 0.01$ were prepared by diluting stock solutions with deionised water. The sample cell was made of a small (10 mm in diameter) glass vial which had been cut in half across the width, glued onto a coverslip and subsequently plasma-cleaned to ensure that the particles did not stick to the wall. Particles were allowed to sediment completely before any measurements were taken. According to the sedimentation velocity provided in eq. (2.2), particles should be completely sedimented approximately one hour after sample preparation, but a delay of 48 hours was used for all experiments unless otherwise stated to allow stable structures to be reached. The samples contained approximately 15 layers of particles, where the gravitational length was 0.2 μm. Each sample had a colloid area fraction of approximately 0.7 (see table 4.1). After sedimentation, the layer closest to the bottom wall was observed using a Zeiss LSM 5 Exciter confocal microscope, equipped with a 63× oil immersion objective. Each dataset consisted of 100 frames, with each frame containing approximately 3000 particles. The 2D coordinates of the colloidal particles were tracked using standard image analysis routines (see section 2.9) [82].

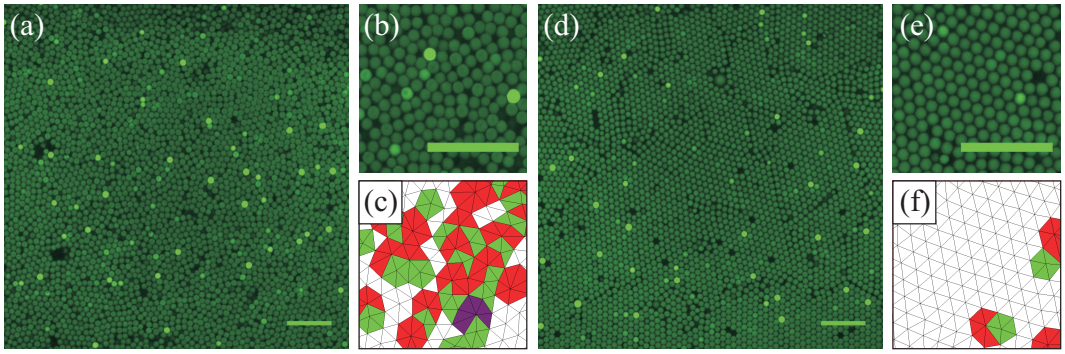

Figure 4.1: Confocal microscopy images of first layers of dimpled (a and b), and spherical particles (d and e). (a) and (d) show the full frame, while (b) and (e) give a zoomed in area. (c) and (f) show the Delaunay triangulations corresponding to (b) and (e), respectively, and indicate the particles whose coordination is not sixfold. The colours used are: fourfold - blue, fivefold - green, sevenfold - red, eightfold - purple. All scale bars are 20 μm.

	Spherical	Dimpled
area fraction	0.72	0.69
ξ_t/σ	2.5	1.2
ξ_o/σ	12.6	1.6
ψ_6	0.82	0.61

Table 4.1: Area fractions, correlation lengths, ξ_t and ξ_o, and the local hexagonal order parameter, ψ_6, for spherical and dimpled particles. σ is the particle diameter.

4.3 Results and discussion

Typical confocal microscopy images of the sedimented dimpled particles and spheres are shown in figures 4.1(a,b) and (d,e), respectively. It is clear, even from inspection by eye, that the anisotropy in shape of the dimpled particles induces a disruption of the hexagonal structure. This is further illustrated by the Delaunay triangulations shown in figures 4.1(c) and (f). Here, the defects (caused by particles not having sixfold coordination) are shown in colour. Clearly, there are many more defects in a system of dimpled particles than in one of spherical particles. To quantify this effect, we study both the translational and orientational order using the radial distribution function, $g(r)$, the bond-orientational correlation function, $g_6(r)$, and the local bond-orientational order parameter, ψ_6 [111]. These quantities are defined as [12, 114–116]:

$$g(r) = \frac{1}{\rho}\left\langle \sum_{i}^{N}\sum_{j\neq i}^{N} \delta[\mathbf{r} - \mathbf{r}_j + \mathbf{r}_i] \right\rangle, \tag{4.1}$$

and

$$g_6(r) = \langle \psi_6^*(0)\psi_6(r)\rangle, \tag{4.2}$$

with

$$\psi_6(r_i) = \frac{1}{N}\sum_{j}^{N} \exp\left[6i\theta(r_{ij})\right], \tag{4.3}$$

where ρ is the average particle number density, N is the number of nearest neighbours of particle i, and $\theta(r_{ij})$ is defined as the angle between the vector connecting particles i and j and an arbitrary axis. For convenience, the average of the absolute value of $\psi_6(r)$ is referred to as ψ_6. For a perfectly crystalline system of hexagonally packed particles, we would expect a ψ_6 value of 1, and any value lower than this illustrates a decrease in the local hexagonal order. In order

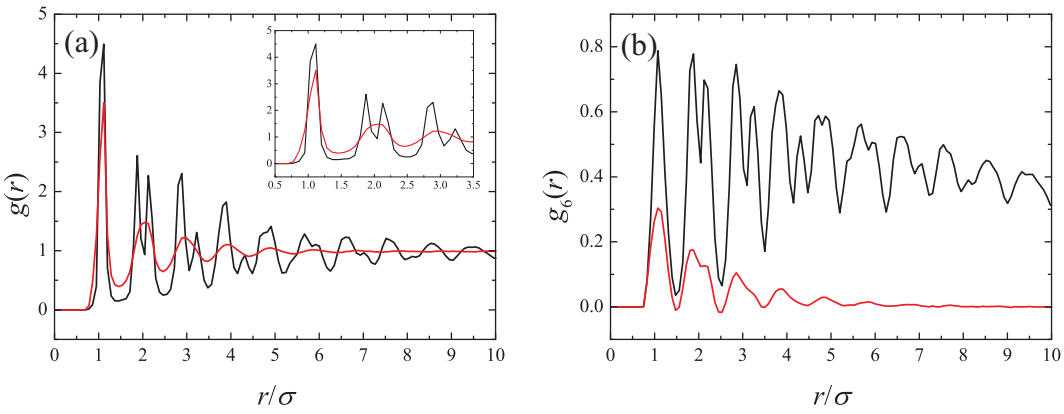

Figure 4.2: (a) Radial distribution functions, and (b) bond-orientational correlation functions of the spherical (black) and dimpled (red) particles. All data presented here were recorded at least 48 hours after sample preparation.

to avoid seeing effects due to the edge of the image in the $g(r)$, we calculate a second radial distribution function for a set of random coordinates placed within a box of the same dimensions as the experimental image. We then divide the real $g(r)$ by the one formed from the random coordinates, thus eliminating any false information pertaining to the lack of periodic boundaries in experiments. It should be noted that the effect of any grain boundaries in the polycrystalline systems has been neglected. Inclusion of such grain boundaries would be expected to cause a decrease in the global order seen in the system, but only by a small amount. Due to the small size of the domains in the dimpled particles in particular, it was not possible to study single crystalline regions, and thus all grain boundaries were ignored.

As can be seen from a comparison of the radial distribution functions of the spherical and dimpled particles (figure 4.2(a)), the longer ranged order that is present in the former case is significantly suppressed in the latter. This is shown by both an increase in the speed at which the radial distribution function decays, and a decrease in the splitting of the peaks. The diminished splitting seen for dimpled particles is due to the outer coordination shells being less well defined than for the spherical case, indicating weaker ordering. We also see an increased peak width for the dimpled particles for similar reasons. Particularly interesting is the small broadening of the left hand side of the first peak in the $g(r)$ for the dimpled particles. This is caused by the convex side of one particle fitting into the concave side of another. By fitting the envelope of the radial distribution function, we are able to determine the translational correlation length, ξ_t (envelope of $g(r) \propto \exp[-r/\xi_t]$) [111]. This gives an idea of the range over which translational order extends, and is found to be larger for the spherical particles than for the dimpled particles

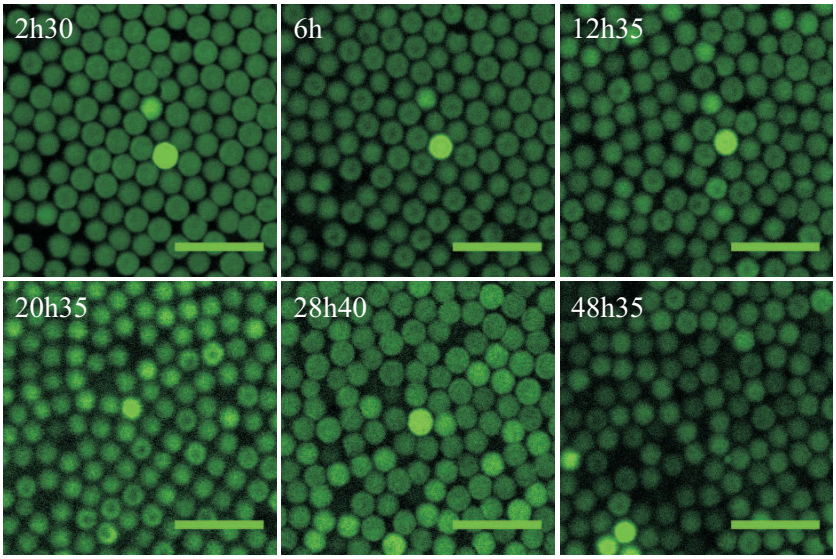

Figure 4.3: Confocal microscopy images of the same area of dimpled particles at intervals within the first 48 hours of sample preparation. The images here are slices through the centres of the particles, and thus the dimples are not clearly visible. The area fractions of the samples remain relatively constant over time. The intensity of the images decreases with time due to photo-bleaching. Scale bars are 10 μm; times are with respect to sample preparation.

(see table 4.1). It should be noted, however, that ξ_t is not particularly large in either case, and certainly does not constitute long range translational order.

The bond-orientational correlation functions (figure 4.2(b)) also illustrate a lower level of order in the system of dimpled particles, as can be seen by the faster decay of $g_6(r)$, and the decrease in the splitting of the peaks, just as in the radial distribution functions. To give a clearer indication of the size of the crystalline domains in the systems, we can use the orientational correlation length, ξ_o, found by fitting the envelope of the bond-orientational correlation function (envelope of $g_6(r) \propto \exp[-r/\xi_o]$) [111]. ξ_o is found to be significantly lower for the dimpled particles (see table 4.1). Both of these observations are clearly an effect of the dimple disrupting the hexagonal packing seen for the spherical particles, and are further corroborated by the decrease in local hexagonal order (quantified by ψ_6) shown by the dimpled particles (see table 4.1).

One might expect that order would develop over time, as particles would feel the effect of the pressure of the upper layers. With the spherical particles this is indeed the case; however, perhaps counter-intuitively, this is not seen in a system of dimpled particles. Instead, directly after sedimentation, a much more crystalline configuration is seen, which becomes disordered over time and settles to a more structurally liquid-like state within 48 hours (figure 4.3). Im-

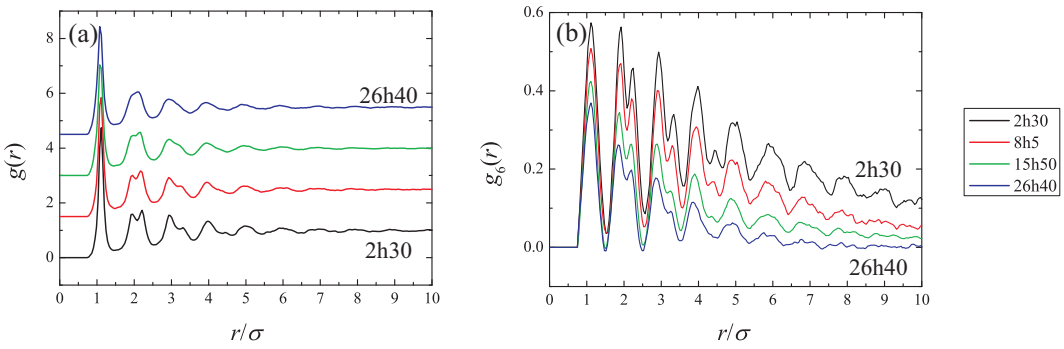

Figure 4.4: (a) Radial distribution functions, and (b) bond-orientational correlation functions of the dimpled particles, recorded at intervals during the first 48 hours after sample preparation. The former have been shifted vertically for clarity.

portantly, the number density of the particles in the samples remains relatively constant over time (figure 4.5(c)). Again, we are able to quantify this decrease in order by calculating the $g(r)$, ψ_6 and $g_6(r)$ of the sample at various different times. From figure 4.4(a), we can see that the splitting seen initially in the peaks of the $g(r)$ diminishes significantly as time goes on, as does the range over which we see translational order. A similar effect is seen in figure 4.4(b), where now the faster decay of $g_6(r)$ signifies a system with decreasing crystallinity. Finally, from

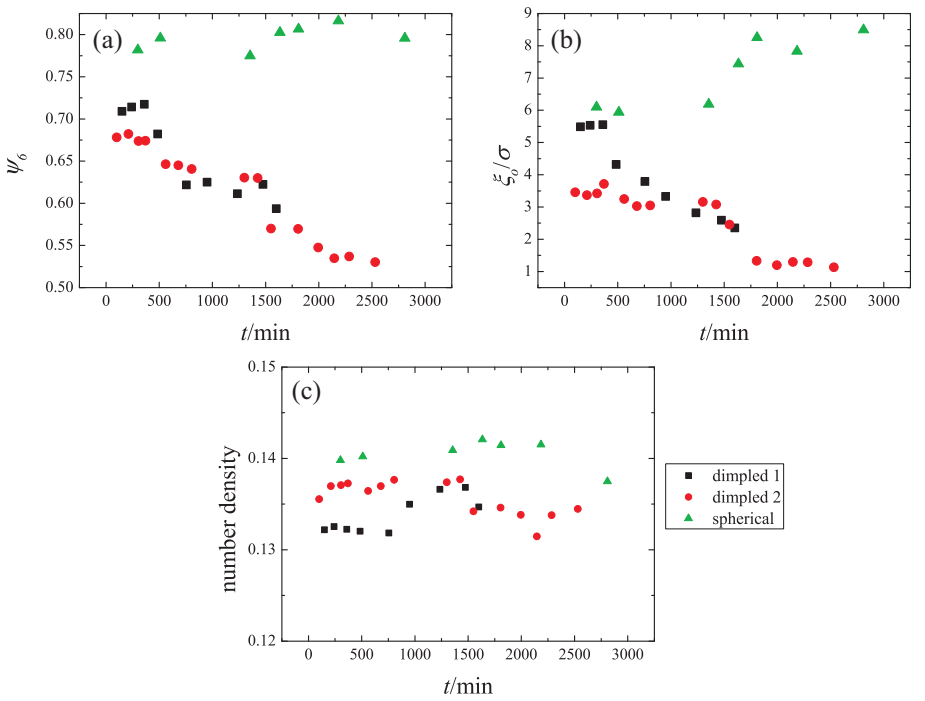

Figure 4.5: (a) ψ_6 as a function of time, (b) ξ_o as a function of time, and (c) number density as a function of time for both the dimpled and spherical particles during the first 48 hours after sample preparation. The two symbols for the dimpled particles represent two different experiments.

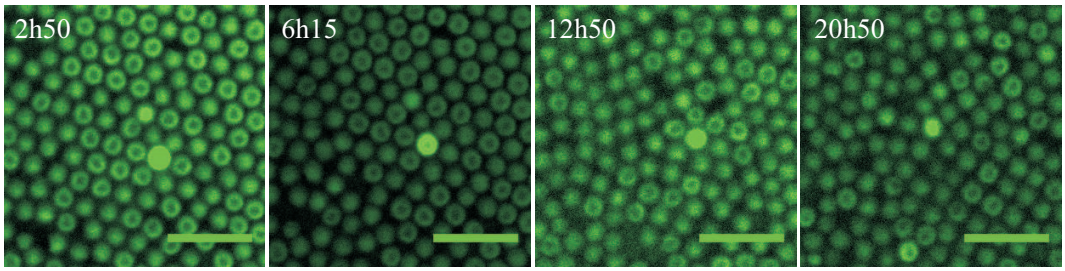

Figure 4.6: Confocal microscopy images of the same area of dimpled particles at intervals within the first 48 hours of sample preparation. The images here are slices that illustrate the presence of dimples, appearing as dark spots. The intensity of the images decreases with time due to photo-bleaching. Scale bars are 10 μm; times are with respect to sample preparation.

figure 4.5(a), we see a clear decrease in the value of the local bond-orientational order parameter as a function of time. However, the same parameter remains fairly constant for the spherical particles.

We are able to obtain additional information about the structural disorder over time by looking at the translational and orientational correlation lengths, ξ_t and ξ_o, respectively. The translational correlation length is very low for both the spherical and dimpled particles, and as such does not noticeably decay over time. The orientational correlation length, however, provides us with more information: ξ_o for the dimpled particles decreases over time, illustrating that the structural disorder reduces the size of the crystalline domains; yet, conversely, ξ_o increases with time for the spherical particles, as the pressure from the upper layers improves crystallinity (see figure 4.5(b)).

In order to rationalise this behaviour, we identify the particles for which the dimple is facing down. By imaging slices through the samples in the z direction (i.e. parallel to gravity), we can locate such particles, as they appear to have a dark spot towards the bottom of the cell (see figure 4.6). The link between the fraction of particles that are "dimple-down" and the amount of local hexagonal order (as quantified by ψ_6) is shown in figure 4.7. Here, we see that a larger fraction of dimple-down particles corresponds to a higher ψ_6. From this it is apparent that the decrease in crystallinity over time is linked to dimples rotating away from the wall.

To try and determine the cause of this change, we varied the colloidal volume fractions used, resulting in new systems with $\phi_c \approx 0.001$ ("dilute") and $\phi_c \approx 0.03$ ("concentrated"). We can estimate the total number of layers of particles in each of the three systems and we find that in the original case (where $\phi_c \approx 0.01$), we have approximately 15 layers, in the dilute

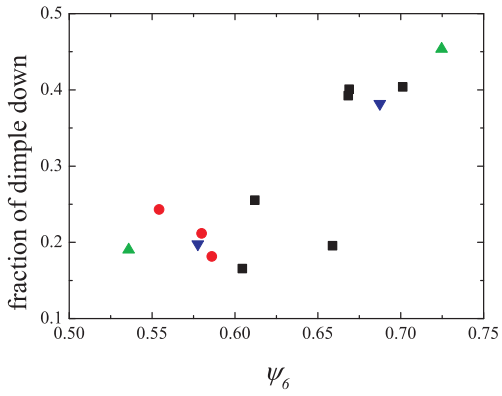

Figure 4.7: The fraction of particles that are oriented with their dimple facing down (i.e. to the bottom wall of the sample cell) as a function of the local bond-orientational order parameter. Different symbols represent different experiments.

case we have approximately two layers, and in the concentrated case we have approximately 50 layers. As can be seen in figure 4.8, the amount of order (as quantified by ψ_6) decreases as the number of layers of particles increases. We also see a more rapid disruption of order as our systems become more concentrated. The only change in the system is the pressure experienced by the first layer due to the upper layers, and thus we speculate that by rotating away from a dimple-down orientation, the system is able to better accommodate this pressure, despite the fact that this leads to a disordered state. The average nearest neighbour distance between particles remains fairly constant over time, but the spread of these distances increases. We thus further hypothesise that particles in the disrupted state have slightly more space to move in and hence this state is entropically more favourable. When the particles are in the dimple-down state, they look and behave like spheres in the plane parallel to the wall. This agrees with the observation that the systems with spherical particles show much more crystalline order.

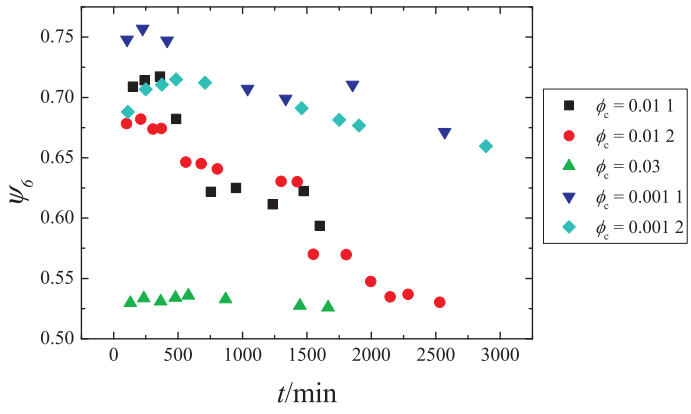

Figure 4.8: ψ_6 as a function of time for systems of the dimpled particles of various concentrations during the first 48 hours after sample preparation.

4.4 Conclusions

We have shown that uniform shape anisotropy greatly affects the ordering of particles close to a wall. In particular, we have used confocal microscopy and real-space image analysis to demonstrate that the presence of a small, well-defined dimple on an otherwise spherical particle suppresses both the translational and orientational order seen for an equivalent spherical particle. We have characterised the systems' order using the radial distribution function, the bond-orientational correlation function, and the local bond-orientational order parameter. Within the first 48 hours of sample preparation, a decrease in the crystallinity of the first layer is seen for the dimpled particles, along with a transition from particles facing dimple-down (and thus behaving as a sphere in the plane of observation) to those with their dimples in the plane of the image, without an increase in particle number density. We hypothesise that this reorientation is driven by the pressure from the upper layers, despite leading to a structurally disordered state. This hypothesis may better be tested by computer simulations in the spirit of Dijkstra et al. [94, 95].

Our findings illustrate the profound role of boundary conditions in amplifying the differences between spherical and non-spherical particles, here illustrated by the simplest possible boundaries. The coupling between more complex, geometrically structured walls and particle anisotropy is expected to be very rich, may lead to novel frustrated or ordered states, and thus deserves further attention.

Acknowledgements This work was done in collaboration with Roel Dullens and Stefano Sacanna. It is a pleasure to thank Michael Juniper for useful discussions.

Chapter 5

Probing the effect of shape anisotropy on depletion induced interactions against a single planar wall

ABSTRACT

We study the effect of particle shape anisotropy on depletion interactions in a monolayer of colloidal particles at a single featureless wall. To this end, we use systems of both uniformly dimpled spheres and isotropic spherical particles with non-adsorbing polymer, specifically xanthan and poly(ethylene oxide). We employ laser scanning confocal microscopy and real-space analysis, as well as Monte Carlo simulations, to investigate the structures formed for a variety of systems. We show that many contributing factors affect the particles' behaviour, the most prominent of which being the supplementary peak splitting seen in the radial distribution function for a system of dimpled particles when a small polymer is added and the suspension is at sufficient ionic strength.

5.1 Introduction

Since the theoretical description of depletion interactions by Asakura and Oosawa in the 1950s [47,48], considerable attention has been given to suspensions of colloidal particles and depletants, both in experiments and simulations (see [46] and the references therein).

Systems of isotropic particles with depletion induced attractions have been studied in detail (for example, [117–120]), but particles that are anisotropic in shape are much less frequently seen in the literature, despite leading to interesting phenomena. It has been shown that depletion interactions instigate bundle formation in suspensions of colloidal rods [121], and stacking of colloidal platelets can be controlled by tuning the ratio of depletant size to surface roughness [122]. Additionally, polyhedral "rock" particles form structures of low fractal dimension in a solution with added depletant, compared to the locally dense regions found with their spherical counterparts [123].

The presence of boundaries in systems of spherical colloidal particles and depletants has been shown to provide rich behaviour. A planar wall may cause depletion induced crystallisation to occur at much lower colloidal concentrations than in the equivalent bulk setups [124, 125], and terraced surfaces allow control of particle motion through depletion interactions [126]. The addition of particle shape anisotropy to a system with both bounding surfaces and polymer induced attractions is expected to lead to further intriguing phenomena.

Depletion induced interactions in systems of uniformly dimpled colloidal particles have been studied in Monte Carlo simulations without the presence of a solid boundary, using nanoparticles as a depletant [100]. In the aforementioned work, the focus was on the effect of particle shape and depletant density. In this chapter we use both experiments and Monte Carlo simulations to additionally study the effect of the size and nature of the depletant, as well as the concentration of the colloidal particles. Importantly, we examine the behaviour of a monolayer of colloidal particles against a single featureless wall.

We will start by outlining the theoretical background behind this work in section 5.2, including the calculations of the magnitudes of both the depletion attractions (section 5.2.1) and the double layer repulsions (section 5.2.2). In section 5.3, we detail the experimental setup, and present and discuss the experimental results. Similarly, in section 5.4 we describe the

simulation parameters used, and relate the results to those found experimentally. Finally, we conclude in section 5.5.

5.2 Theory

We begin by considering the interparticle interactions within our experimental systems in order to predict more explicitly the behaviour expected.

5.2.1 Depletion attractions

According to the Asakura-Oosawa-Vrij (AOV) model [48, 49], the strength of the depletion interaction, $U_{dep}(d)$, in a system of ideal polymers is proportional to the overlap volume, $V_{ov}(d)$, of the depletion zones surrounding each particle,

$$U_{dep}(d) = -n_p k_{\mathrm{B}} T V_{ov}(d), \tag{5.1}$$

with d the separation between particles, n_p the number density of depletants, k_{B} Boltzmann's constant, and T the temperature. Using this relationship we are able to compare the magnitudes of the depletion interactions for the three configurations of interest: i) the dimpled particles in chain formation, ii) the dimpled particles in dimple-down formation, and iii) the spherical particles (figure 5.1). All configurations lie against a planar surface. To simplify the calculations involved, we find the overlap volumes at zero separation only, i.e. we remove any dependence on particle separation, we assume that the radius of curvature of the dimple is equal to that of the particle, and we model both the particles and depletion zones as having sharp edges, as in chapter 3. Ignoring the rounding of the depletion zones is expected to cause a slight discrepancy in the computed overlap volume, but the calculation of such a rounded volume is beyond the scope of this thesis. We vary the depletant size to additionally investigate the role of the polymer radius of gyration on structure formation. Care is taken that the overlaps never extend into one another (i.e. only pairwise interactions are used), which only happens at depletant sizes larger than those used in our experiments. It should be noted here that any structure formation driven by the presence of additional salt in the solution is not included in this calculation, as at zero separation, the double layer repulsion is independent of ionic strength [127]. Further detail on

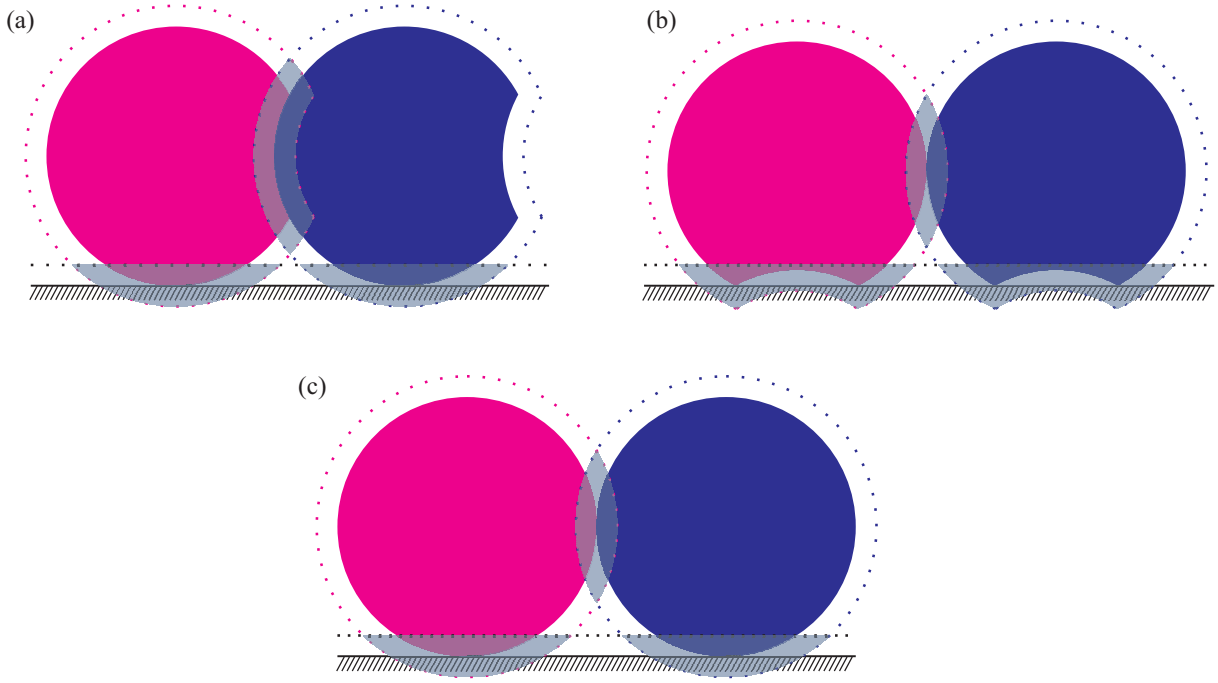

Figure 5.1: Diagram showing the overlap of the depletion zones for the three configurations of interest: (a) dimpled particles in chain formation, (b) dimpled particles in dimple-down formation, and (c) spherical particles. The depletion zones are shown with dashed lines, and the overlap is designated by the grey shaded areas.

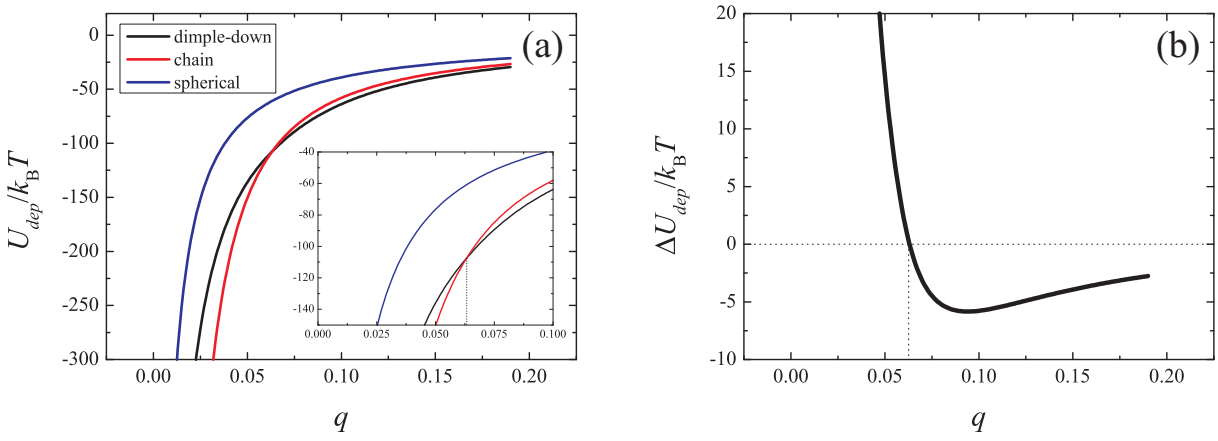

Figure 5.2: (a) Depletion interaction energy, U_{dep}, in terms of k_BT versus size ratio, $q = R_g/R$, for the three configurations of interest with a polymer volume fraction of 0.5. The inset gives a close up of the energies for small polymer sizes, and highlights the crossover from chain formation to dimple-down configuration. (b) ΔU_{dep}, the difference in the depletion interaction energy between the dimple-down and chain configurations. This clearly highlights the point at which the dimple-down arrangement becomes more favourable.

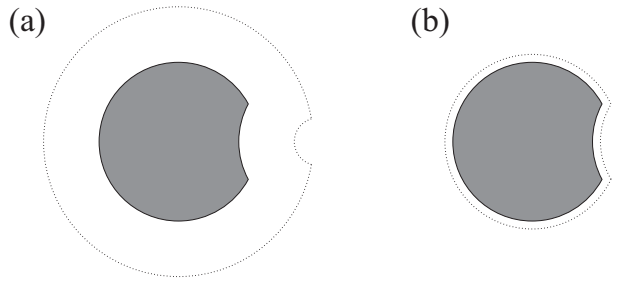

Figure 5.3: Diagram illustrating the depletion zones (with sharp edges) for (a) a polymer with a large radius of gyration, and (b) a polymer with a small radius of gyration. It can be seen that the depletion zone in (b) more closely mirrors the particle shape.

the calculations performed are given in the appendix.

The results are presented in figure 5.2 for a system with a polymer volume fraction of 0.5. It can be seen that the magnitude of the depletion attraction for the spherical particles is always less than that for either configuration of dimpled particles. This is due to the smaller particle-particle and particle-wall overlap. When comparing the two possibilities for the dimpled particles, we see that at small depletant sizes, chain formation is preferred, but for polymers with a size ratio, $q = R_g/R$ (with R the particle radius), larger than approximately 0.06, it is energetically more favourable for the particles to be dimple-down. We can rationalise this by considering the shapes of the depletion zones with different sized polymers (figure 5.3). Chain formation is promoted by the complementary particle-particle overlap, as the convex side of one particle fits precisely into the concave dimple of another. We can see that with a small polymer, the depletion zone more closely mirrors the particle shape, and thus the effect of the dimple is more evident, and we find that chain formation is more favourable.

5.2.2 DLVO theory

In the 1940s, Derjaguin and Landau [44] and Verwey and Overbeek [45] illustrated that colloidal stability is governed by the interplay between attractive van der Waals forces, and repulsive double layer interactions. Van der Waals attractions can be assumed to be unaffected by the addition of the small amounts of salt used in this work [45] and hence the interparticle attraction will remain constant. Conversely, electrical double layer repulsions stem from the overlap of the inhomogeneous layer of ions from solution surrounding each charged particle. The thickness of

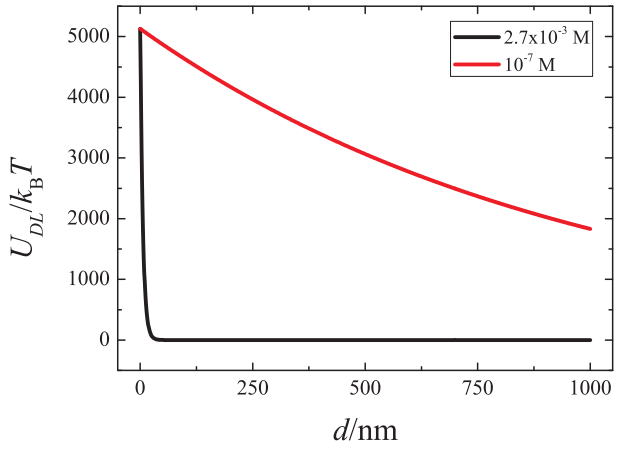

Figure 5.4: Double layer repulsion as a function of interparticle separation for systems with and without salt. When salt is present, the double layer repulsion decays far more rapidly.

this layer is given by the Debye length, κ^{-1}:

$$\kappa^{-1} = \left(\frac{\epsilon_0 \epsilon_r k_\mathrm{B} T}{2e^2 N_A I} \right)^{\frac{1}{2}}, \tag{5.2}$$

where ϵ_0 is the vacuum permittivity, ϵ_r is the relative permittivity of the medium, e is the elementary charge, N_A is Avogadro's number, and I is the ionic strength of the electrolyte in mol m^{-3}. In the limit $d \gg \kappa^{-1}$, the double layer repulsion between two spheres is approximated as,

$$U_{DL}(d) = 64\pi k_\mathrm{B} T R N_A I \kappa^{-2} \tanh^2 \left(\frac{e\psi_0}{4k_\mathrm{B}T} \right) \mathrm{e}^{-\kappa d} \tag{5.3}$$

with ψ_0 the surface potential of the particles [128]. From the literature, we know that ψ_0 for our particles is approximately 70 mV [50], and we can therefore plot the strength of the double layer repulsion as a function of interparticle separation for a given salt concentration. We approximate that our particles are spherical, as the small deviation from sphericity is expected to have a negligible effect. Figure 5.4 shows the double layer repulsion for NaCl concentrations of 2.7×10^{-3} M and 10^{-7} M, corresponding to typical systems with and without salt, respectively. As explained in section 2.2.1, the colloidal solutions used in experiment have a non-zero counter-ion concentration, and hence, in reality, the double layer repulsion when there is no salt present is less extreme than predicted in figure 5.4, and the plot is instead used to demonstrate, qualitatively, the effect of additional salt.

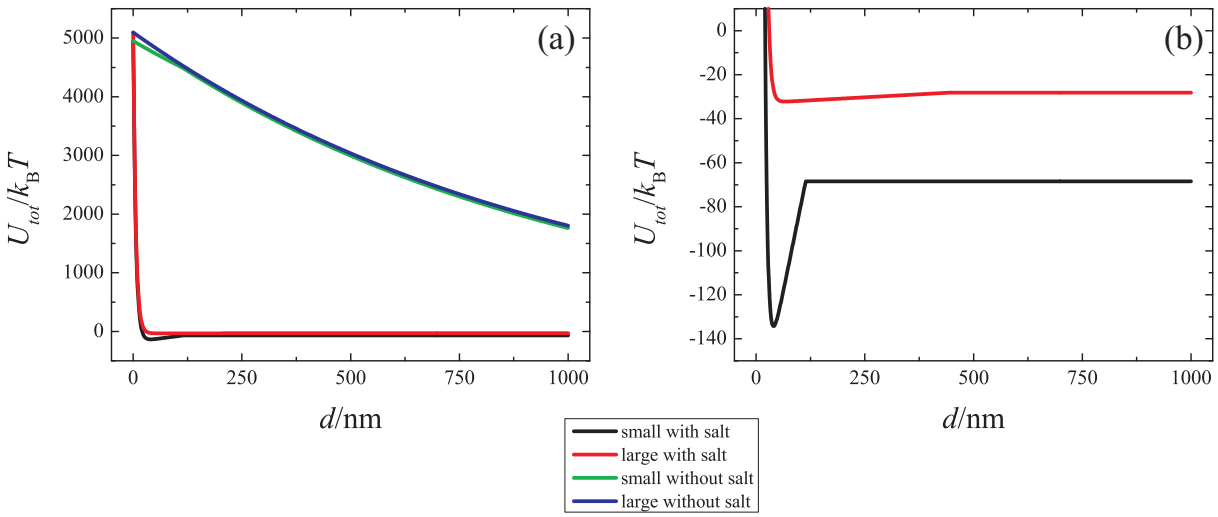

Figure 5.5: (a) Approximate total forces as a function of interparticle separation for systems with and without salt at two different polymer sizes. (b) The effect of depletion at small separations when salt is present. The polymer volume fraction is 0.5, and both particle-particle and particle-wall depletion interactions are included, as in figure 5.2.

5.2.3 Total forces

Finally, in order to assess the total forces on the system, we must compare the magnitudes of the attractive and repulsive forces. It is clear from above that there are four depletant systems to address: a small polymer without salt, a small polymer with salt, a large polymer without salt, and a large polymer with salt. Figure 5.2 indicates that we should use the dimple-down configuration when calculating the depletion attraction for a system with a large polymer, and that chain formation should be assumed for small polymer systems. We combine the depletion attraction, assuming a linear dependence on particle separation, with the double layer repulsion from figure 5.4 to compute the net interparticle interaction. We note that the depletion interaction remains constant at separations larger than $2R_g$, as only wall-particle overlap remains. This is shown in figure 5.5. We see that the total force on the particle is repulsive when there is no salt present, but that the introduction of additional charges in the system allows depletion to have more effect.

5.3 Experiments

5.3.1 Experimental setup

Similarly to the previous chapter, we used the dimpled and spherical particles synthesised from the same batch of seed droplets, as described in chapter 2. These had a diameter of 2.56 μm and a polydispersity of 4%, as measured by static light scattering. The dimpled particles had a dimple of width $\sim$ 1.3 μm and depth $\sim$ 200 nm, as determined by scanning electron microscopy and atomic force microscopy, respectively. As before, the particles were suspended in deionised water, but in this work, various polymer solutions were added to effect a depletion interaction in our systems. Specifically, we used solutions of xanthan, poly(ethylene oxide) (PEO), and PEO with NaCl as depletants. The xanthan and PEO solutions were prepared according to the methods outlined in chapter 2, and salt was added to some of the PEO systems to screen the charges of the particles, and thereby allow a closer approach of the particles and improve the overlap of depletion zones. It should be noted that the xanthan solution described in chapter 2 also contains NaCl.

As detailed in section 2.4, the gravitational length of the colloidal particles used in this chapter was 0.2 μm, and hence, after approximately two hours, all particles had sedimented onto the base of the container. This allowed us to study the quasi-two-dimensional behaviour of the colloid-polymer mixtures, by using gravity to form a colloidal monolayer. It should be noted that the polymers did not feel the gravity in the same way due to their negligible buoyant mass, and hence remained unaffected by the direct influence of the gravitational field.

Multiple solutions of colloid-polymer mixtures were prepared in order for us to study the effect of the concentration of both colloidal particles and polymer in the system. Due to the sedimentation of the particles, the variables of interest were the colloidal *area* fraction and the polymer *volume* fraction. In this work, colloidal area fractions of $\phi_c^a \approx 0.1$, 0.3 and 0.5 were used, along with polymer volume fractions of $\phi_p \approx 0$, 0.5 and 1. As the samples used were actually three-dimensional in nature, stock solutions of both colloidal particles and polymers were diluted with deionised water such that $V_{tot} = V_1 + V_2 + V_{\mathrm{H_2O}}$, $V_1 = V_{tot}(4R/3h)(\phi_c^a/\phi_c^b)$, and $V_2 = V_{tot}(\phi_p/\phi_p^b)$, with V_{tot} the total volume of each sample, V_1 the volume of stock colloidal solution used, V_2 the volume of stock polymer solution used, $V_{\mathrm{H_2O}}$ the volume of water used,

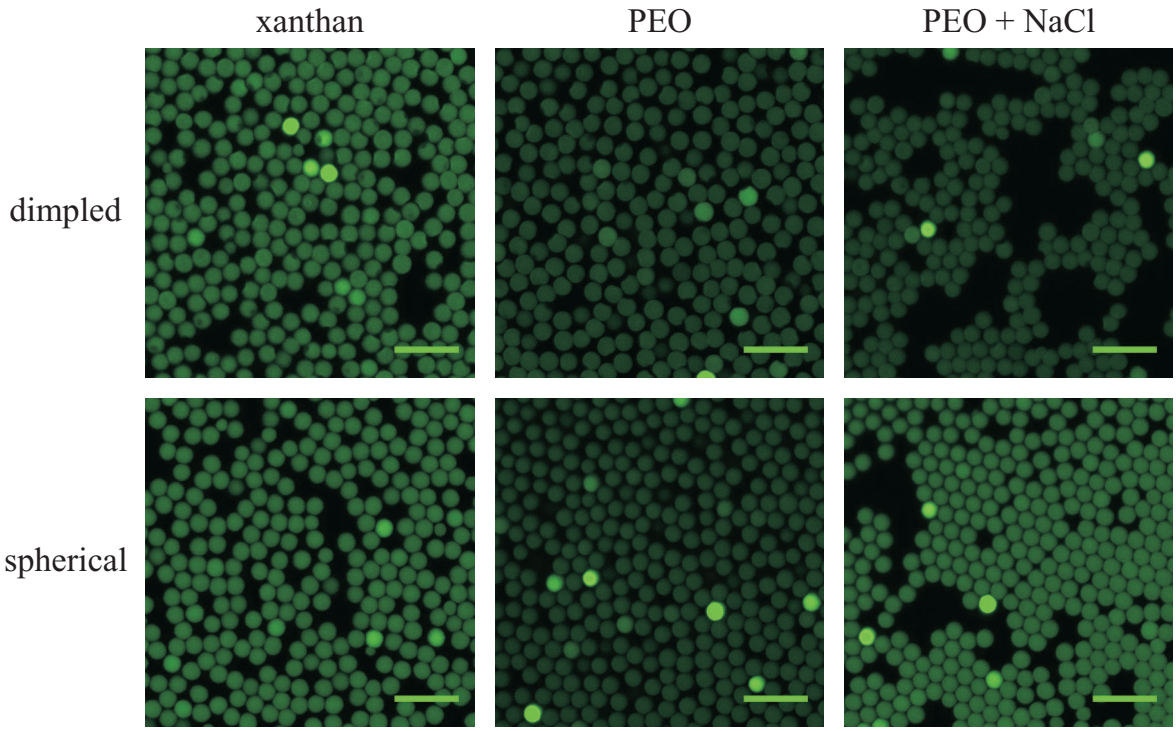

Figure 5.6: Confocal microscopy images of the various systems investigated. Shown are images of each depletant system with both spherical and dimpled particles. ϕ_c^a and ϕ_p are both 0.5, and scale bars are 10 μm.

h the height of the sample, and ϕ_c^b and ϕ_p^b the volume fractions of the stock colloidal solution and polymer solution, respectively. When additional salt was required, a 0.1 M NaCl solution was added using the ratio, $V_{\mathrm{NaCl}} = V_2/2$, with V_{NaCl} the volume of salt solution. As described in chapter 2, the sample cell used was a small (10 mm in diameter) bottomless glass vial, which had been glued onto a coverslip and subsequently plasma-cleaned to prevent any particles from sticking to the wall. A sample volume of 200 μl was used, which corresponded to a sample height of approximately 2.5 mm. Samples were left to sediment completely to form a monolayer, which was then observed using a Zeiss LSM 5 Exciter confocal microscope fitted with a 63× oil immersion objective. For each sample, movies of 150 frames were recorded, where each frame was 51.2 μm × 51.2 μm in size. The 2D coordinates of each particle were then found using the Mathematica tracking routine outlined in chapter 2.

5.3.2 Results and discussion

Example experimental snapshots are provided in figure 5.6. In order to determine the effect of particle shape anisotropy, depletant, and colloid and polymer concentrations on the behaviour

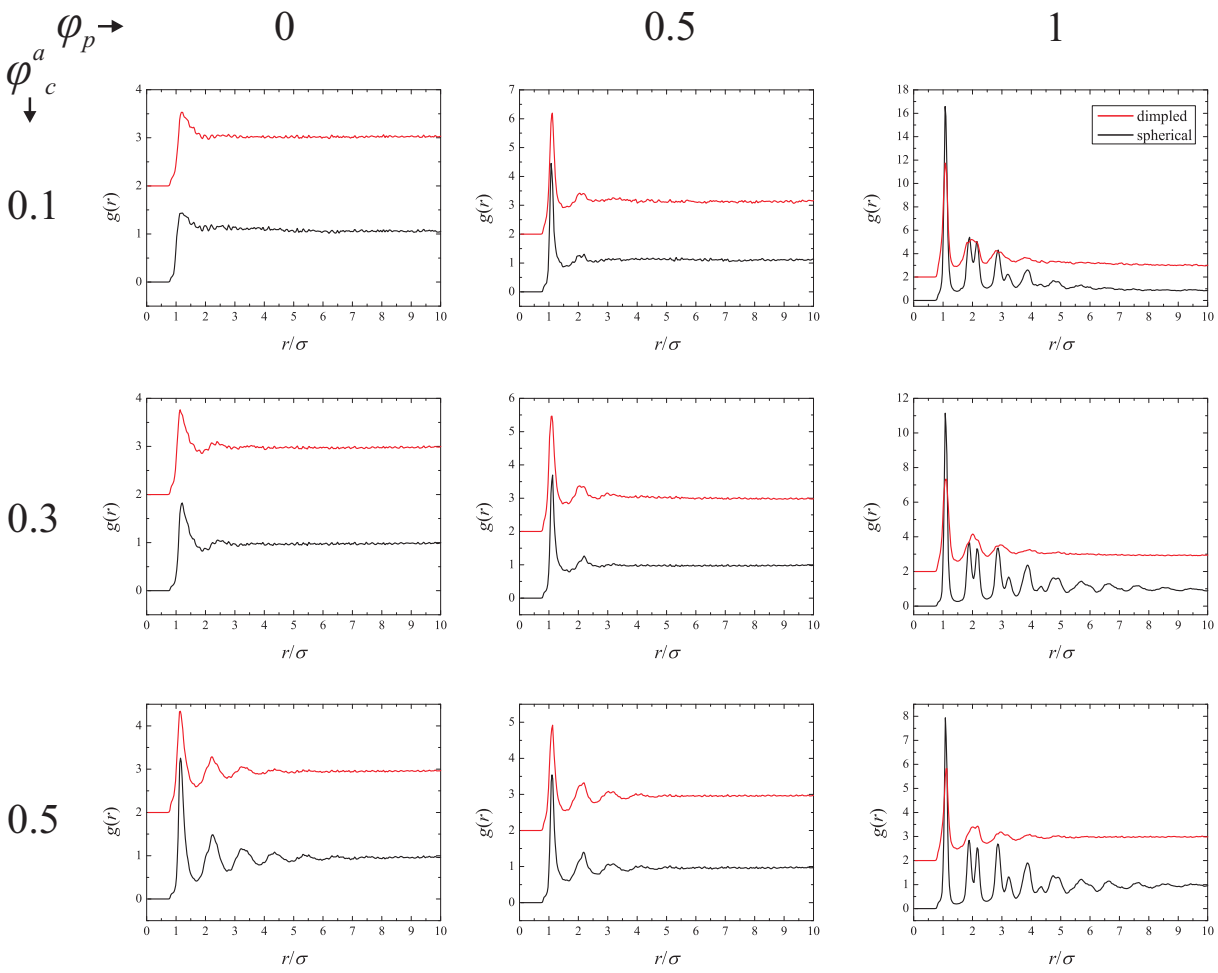

Figure 5.7: Radial distribution functions for both dimpled (red) and spherical (black) particles at various colloid and polymer concentrations. The polymer used is xanthan, with a radius of gyration, R_g, of 222 nm. Plots have been shifted vertically for clarity.

of depletion induced assembly at a planar wall, we compute the radial distribution functions, $g(r)$, for each system studied, similarly to chapter 4. Initially, we compare the $g(r)$s calculated for spherical and dimpled particles at different area fractions, keeping the depletant system the same. Figures 5.7, 5.8, and 5.9 illustrate this for the three polymer systems of xanthan (R_g = 222 nm), PEO (R_g = 57 nm), and PEO plus NaCl (R_g = 57 nm, with added charge screening), respectively.

Looking firstly at figure 5.7, we see that for both particle shapes, the translational order (which is qualified by $g(r)$) becomes longer ranged as we increase both the colloidal area fraction and the polymer volume fraction. This is demonstrated by an increase in the number of peaks and a slower $g(r)$ decay. Both of these trends are to be expected: as we increase the number of particles present, we see more translational ordering. Similarly, we know from eq. (5.1) that

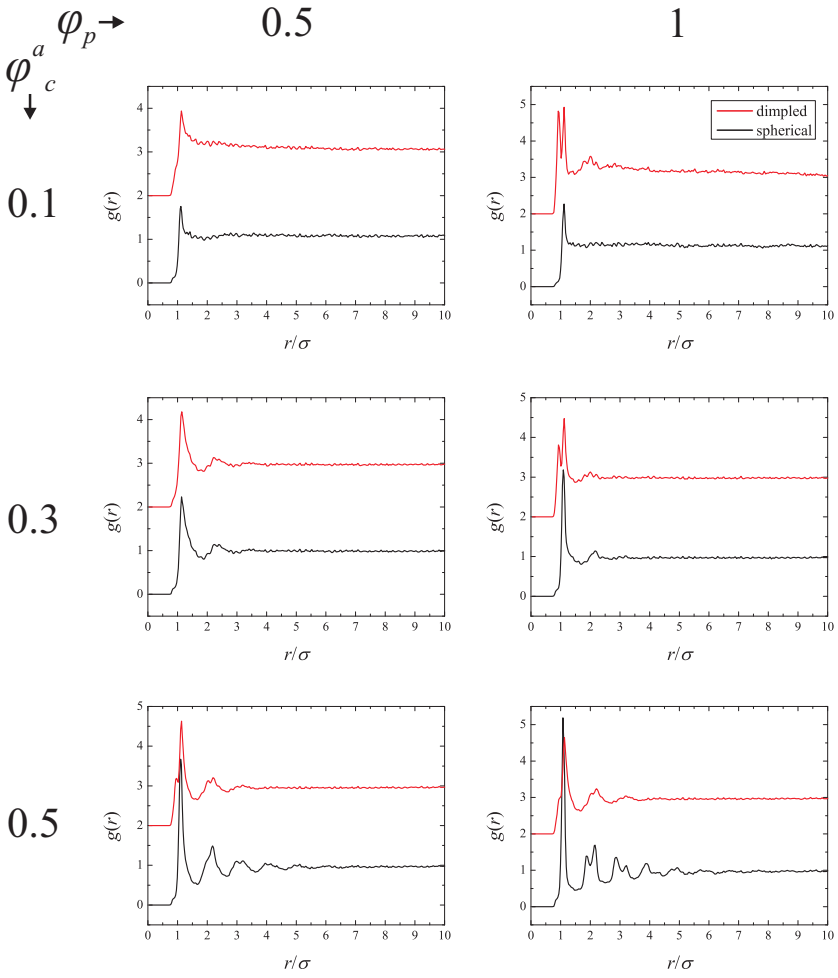

Figure 5.8: Radial distribution functions for both dimpled (red) and spherical (black) particles at various colloid and polymer concentrations. The polymer used is PEO, with a radius of gyration, R_g, of 57 nm. Plots have been shifted vertically for clarity.

the strength of the depletion interaction is directly proportional to the number of depletants in the system. Therefore as we increase the polymer concentration, the particles are drawn more closely to one another via depletion attractions, and hence an increase in ordering is seen.

The second observation that can be seen from figure 5.7 is that more translational ordering is found for the spherical particles than the dimpled particles. This feature is particularly prominent at high polymer concentrations, where the particles are driven more closely together through depletion interactions. These findings clearly mirror those from chapter 4 and stem from the disruption of order due to particle shape anisotropy.

Figures 5.8 and 5.9 tell a similar story to figure 5.7 and simply demonstrate that the trends observed are not specific to the type of depletant used.

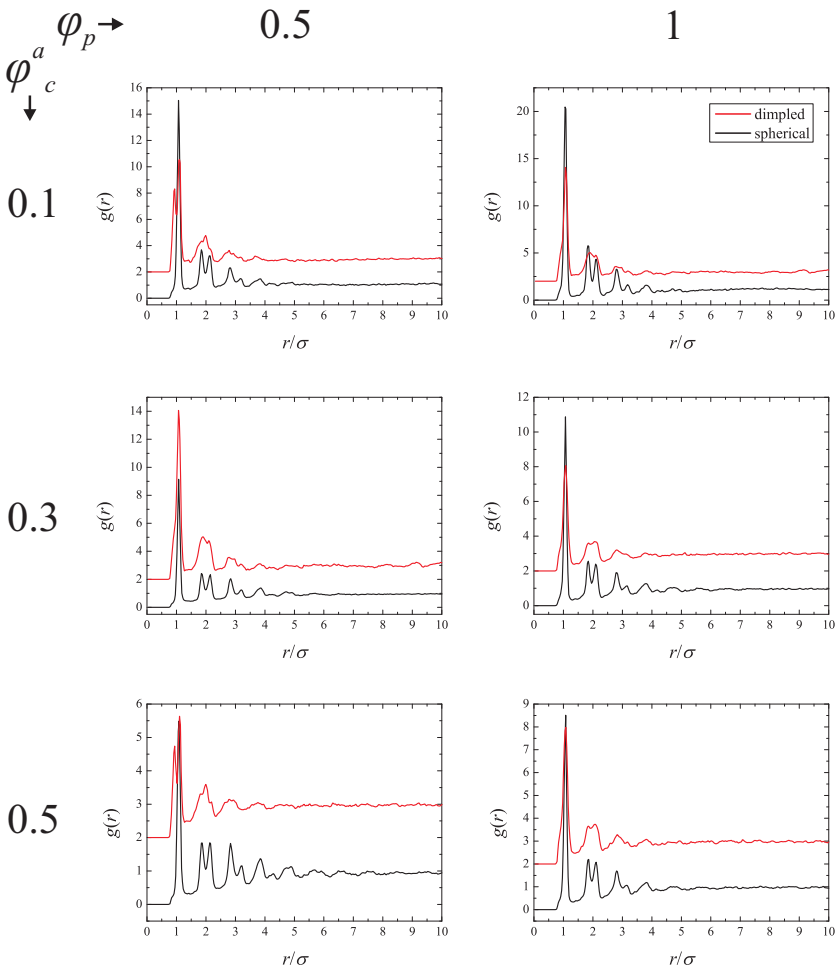

Figure 5.9: Radial distribution functions for both dimpled (red) and spherical (black) particles at various colloid and polymer concentrations. The polymer system used is PEO with NaCl, with a radius of gyration, R_g, of 57 nm and added charge screening. Plots have been shifted vertically for clarity.

We next turn our attention to the effect of the depletant system used on particle assembly. Consider first figure 5.10: we present the radial distribution functions for the spherical particles at various colloid and polymer concentrations with each of the three depletant systems. As before, as both the colloidal area fraction and the polymer volume fraction are raised, we see an increase in translational ordering, demonstrated by a slower decay of the radial distribution function and by an increase in the number of peaks. Additionally, we find that systems containing PEO plus NaCl and those containing xanthan show the most translational order, followed by PEO without salt. This trend can be readily explained using figure 5.5. Here, we have a small polymer with salt (PEO plus NaCl), a large polymer with salt (xanthan), and a small polymer without salt (PEO). When salt is present, there are more charges in solution and thus the double layers are screened from one another, and the interparticle repulsions are lessened. This means

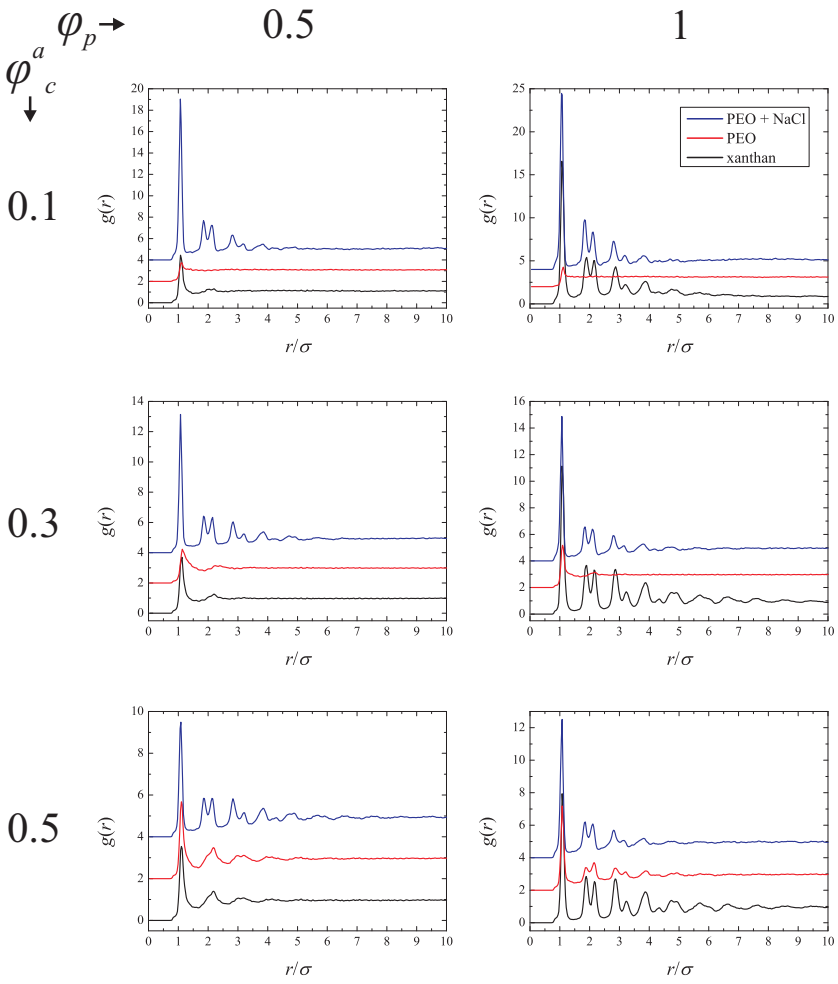

Figure 5.10: Radial distribution functions for spherical particles at various colloid and polymer concentrations using xanthan (black), PEO (red), and PEO plus NaCl (blue). Plots have been shifted vertically for clarity.

that particles are able to approach one another more closely in a solution with added salt, and we see more translational ordering.

Similarly to figure 5.10, figure 5.11 shows the radial distribution functions for various colloid and polymer concentrations with each depletant system, this time for the dimpled particles. We see the same general trends as for the spherical particles, but now there is an interesting additional observation: in a number of systems, the first peak in the $g(r)$ is split into two. This is particularly prominent for the PEO plus NaCl experiments at a polymer volume fraction of 0.5, and is never seen for the systems with xanthan. The splitting of the peak is caused by the convex part of one dimpled particle slotting into the concave part of another - described as chain formation above. Following the theory presented in section 5.2.1, we would indeed expect to see a crossover from the dimple-down configuration, where the particles effectively

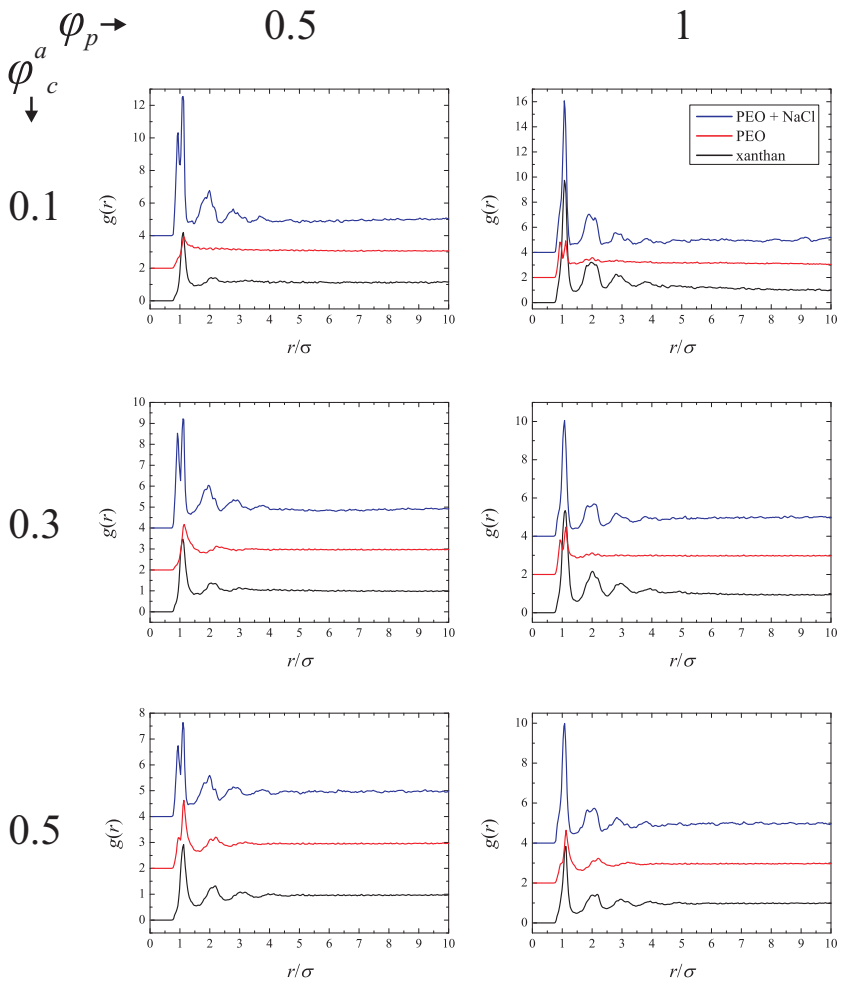

Figure 5.11: Radial distribution functions for dimpled particles at various colloid and polymer concentrations using xanthan (black), PEO (red), and PEO plus NaCl (blue). Plots have been shifted vertically for clarity.

behave as spheres in the plane of observation, to chain formation as the polymer size decreases. The radius of gyration of xanthan is such that we expect the dimple-down configuration to be preferable, but PEO is small enough that chain formation is predicted. This effect is enhanced by the closer interparticle approach allowed in a solution with additional salt. We speculate that the peak splitting is not seen at higher polymer volume fractions for the PEO plus NaCl system as the depletion attraction is too strong to keep the particles in a monolayer, and instead, a 3D system is formed. This is corroborated by a much smaller measured area fraction than expected for the most concentrated systems, and is perhaps indicative of phase separation into a colloid-rich liquid phase and a polymer-rich gas phase [129], potentially before sedimentation is even complete.

We are able to gain further information from the radial distribution functions of the dimpled

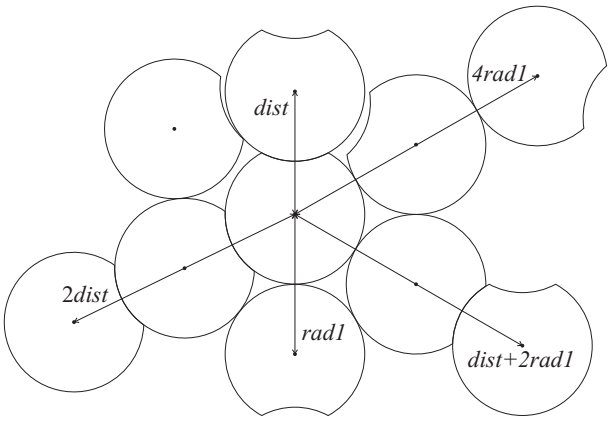

Figure 5.12: Sketch explaining the expected positions of the peaks for the dimpled particles.

particles by identifying the positions of the splittings of the peaks [130]. Using the nomenclature from chapter 3, we expect to see peaks at both $r = dist$ and $r = 2rad1$. Additionally, we expect the second main peak to be split at $r = 2dist$, $r = dist + 2rad1$, and $r = 4rad1$ (see figure 5.12). Figure 5.13 shows the radial distribution functions for all three PEO plus NaCl systems with $\phi_p = 0.5$, and we can clearly see that the splittings occur in the same place for each colloidal area fraction. The first peak is split at 2.4 µm and 2.8 µm, corresponding to a particle radius of 1.4 µm and a dimple depth of 0.2 µm. Further peaks would therefore be expected at 4.8 µm, 5.2 µm and 5.6 µm, and are in fact found at 4.6 µm, 5.1 µm and 5.6 µm. These results are not only consistent amongst themselves, but are also in agreement with our measurements of particle radius and dimple depth, allowing us to assert that chain formation is occurring.

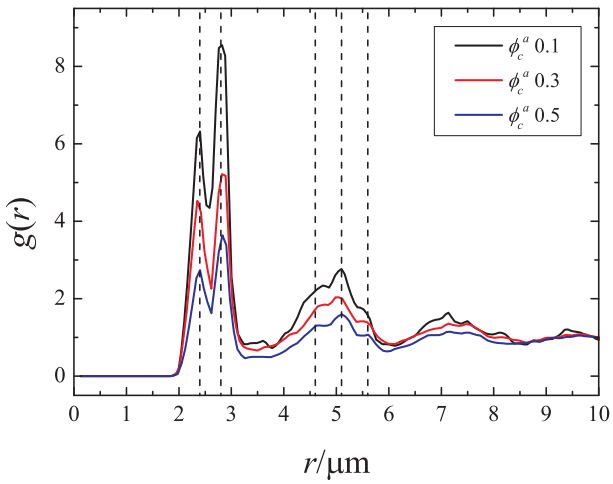

Figure 5.13: Radial distribution functions for dimpled particles for all three PEO plus NaCl systems with $\phi_p = 0.5$. Dashed lines denote the positions of the peaks.

5.4 Simulations

5.4.1 Simulation parameters

Simulations following the algorithm outlined in chapter 3 were carried out to model the systems studied in experiment. Colloidal area fractions, ϕ_c^a, of 0.1, 0.3 and 0.5 were once more used, along with polymer volume fractions, ϕ_p, of 0, 0.5 and 1, although for the simulations, the polymer radius was set to be equal to the particle radius. This was a compromise put in place due to the use of simplified algorithms and the limited computing capacity available to us. Similar and more sophisticated work has been done by Ashton et al. [100, 130].

In addition to the method provided in chapter 3, a radial distribution function was calculated after every (10×number of particles) steps after equilibration to tie in with the analysis of the experimental work. The final $g(r)$ produced was an average of these.

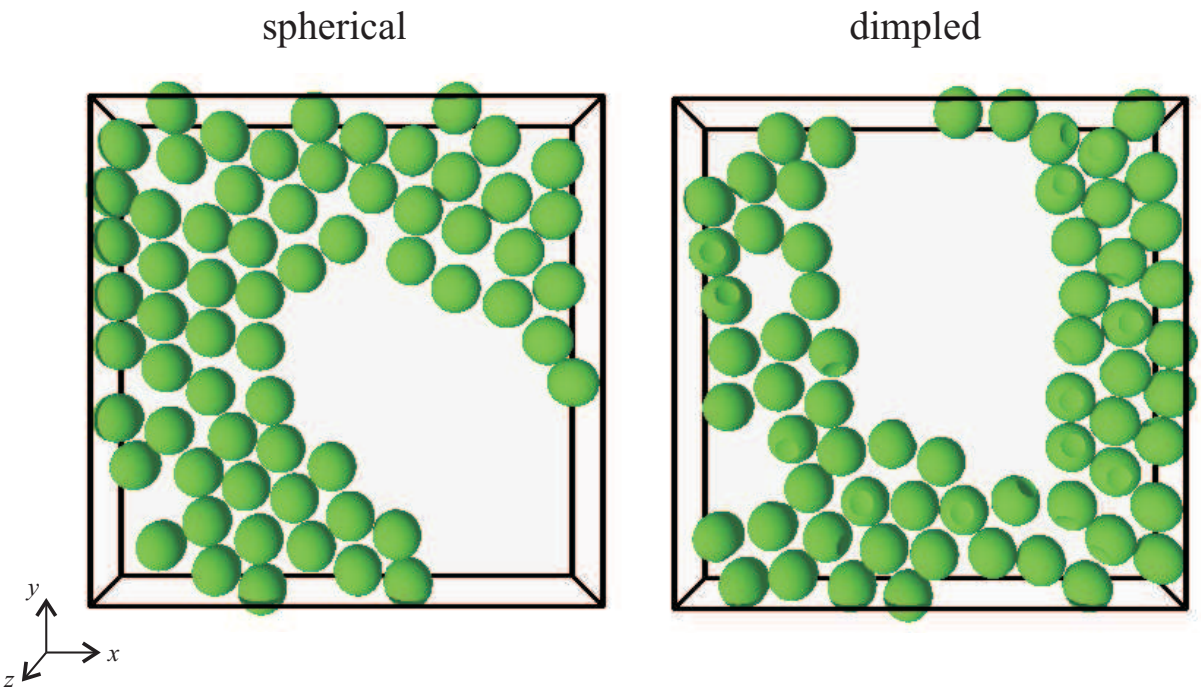

Figure 5.14: Example snapshots of the simulation boxes after all steps have been taken. Images are from below, as in the experimental case. The polymer particles are not shown to make the colloidal particles easier to see. Here, $\phi_c^a = 0.5$ and $\phi_p = 1$.

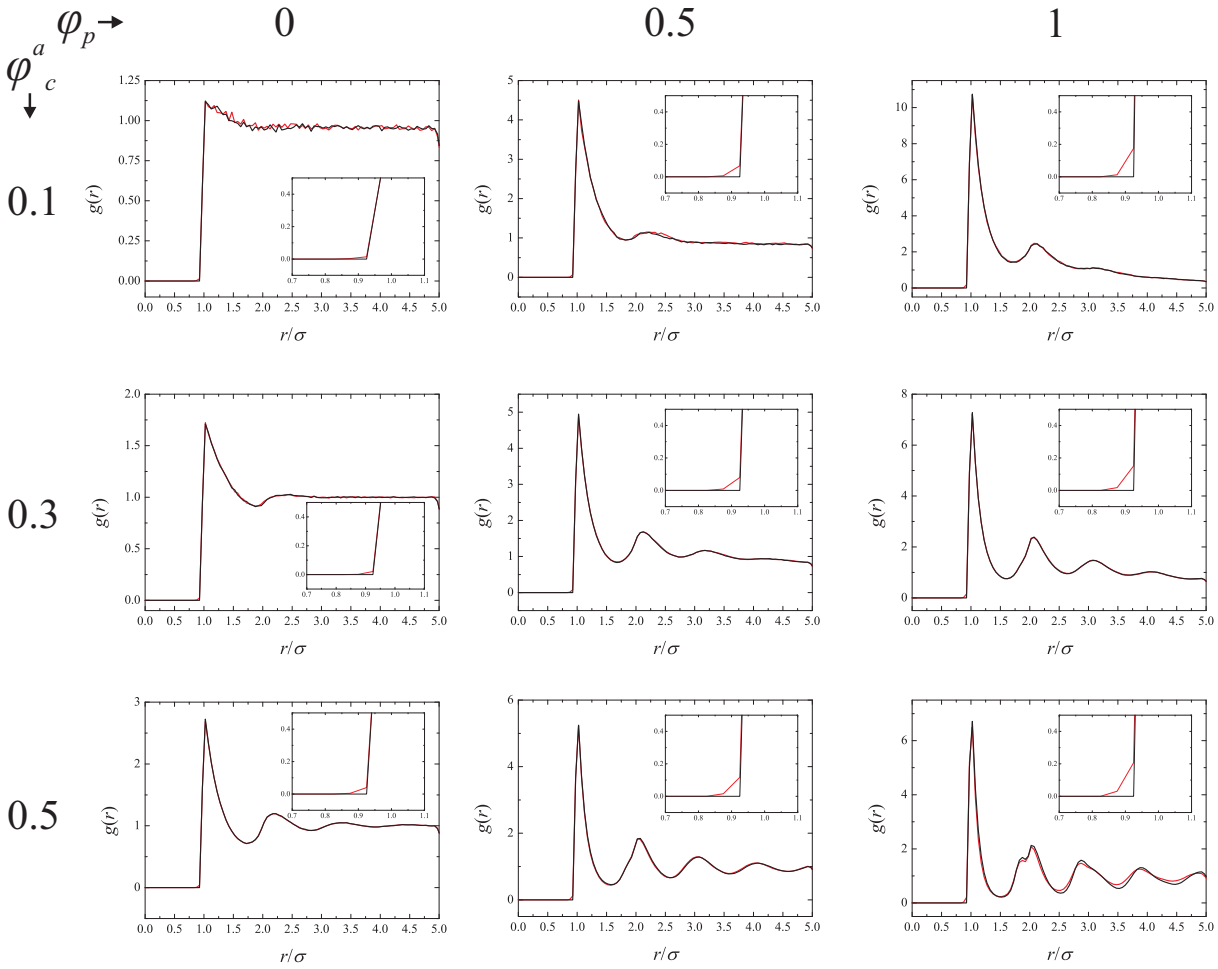

Figure 5.15: Simulated radial distribution functions for both dimpled (red) and spherical (black) particles at various colloid and polymer concentrations. The inset for each graph highlights the left hand side of the first peak, where we see a slight shoulder for the dimpled particles.

5.4.2 Results and discussion

Example snapshots of the simulations are given in figure 5.14. As for the experimental work, radial distribution functions were computed for each system simulated and are shown in figure 5.15. We see that the general trend of increasing translational order with colloid and polymer concentration is still followed, but it is clear that there is very little difference between the behaviour of the dimpled and spherical particles. This deviation from the findings of the experimental work is not unexpected due to the much smaller particle:polymer size ratio - in the simulations this ratio is 1, whereas experimentally we use both 22.5 and 5.8. From figure 5.3 we know that a larger polymer induces a much less shape specific depletion zone around each particle, and hence less differentiation between the two particle shapes is expected with such a small size ratio. One interesting difference to note, however, is the presence of a small shoulder in the radial

distribution functions for the dimpled particles - this is highlighted in the insets of figure 5.15. This shoulder is due to the convex side of one particle fitting into the concave side of another particle, meaning that the interparticle separation is slightly smaller than the particle diameter. This effect becomes more apparent as we increase both the colloid and polymer concentrations due to closer particle packing and increased overlap of depletion zones. This is equivalent to the splitting of the first peak seen for the experimental systems, but the effect is diminished somewhat simply due to the smaller size ratios involved in the simulations. Finally, we see in figure 5.15 that the radial distribution functions do not always tend exactly to 1. This is due to finite size effects because of the small box size used.

5.5 Conclusions

The effect of particle shape anisotropy, depletant, and colloid and polymer concentration on depletion interactions at a single planar wall has been studied using confocal microscopy and real-space image analysis. We have shown that each of these variables contributes to the particles' behaviour, as characterised by the radial distribution function. Increasing the concentrations of both colloidal particles and polymers in the systems results in more translational ordering for all depletants and particle shapes. Additionally, increasing the depletant size leads to an enhancement in particle ordering, as does the presence of charge-screening salt. The inclusion of a small, well-defined dimple on an otherwise spherical particle suppresses the translational order seen for an equivalent spherical particle, and in the right conditions, can lead to supplementary peak splitting in the radial distribution function, due to complementary overlap of particles' depletion zones. This effect has been further corroborated by basic Monte Carlo simulations, in which a shoulder is visible on the left hand side of the first peak of the radial distribution function.

Due to the limitations in computing power and algorithm complexity in the present work, direct comparison between simulation and experiment has not been possible. As such, it would be of great interest to develop the computational methods used to enable greater correspondence between the two in the future.

Acknowledgements It is a pleasure to thank Douglas Ashton, Robert Jack and Nigel Wilding for useful discussions.

Chapter 6

Depletion induced binding of lock and key colloids

ABSTRACT

We study the depletion induced binding of lock and key colloids in a quasi-two-dimensional system at a single featureless wall. The dependence of these interactions upon depletant size and concentration, lock particle shape, and both lock and key concentration is probed using confocal microscopy and a variety of qualitative and quantitative real-space analysis techniques. We show that the inclusion of a lock particle cavity, whose shape and size is complementary to those of the key particle, significantly favours binding behaviour, which is further improved by using a depletant consisting of a small polymer and charge-screening salt.

6.1 Introduction

As synthetic techniques in colloid science have progressed, it has become possible to create a wide range of novel colloidal particles [19,23–27,29,31,131]. These vary enormously in characteristics such as shape, size and surface chemistry, and have received considerable attention due to their potential technological applications. Of particular note over recent years have been colloidal particles that are able to spontaneously self-assemble into interesting and useful structures, with the main focus being on creating a photonic band gap crystal [34–36,43,112,113,132–135].

As is common in many areas of science, colloidal particles can also be used to mimic phenomena observed in nature. One way in which this is done is through the development of particles whose shapes mirror those of molecules such as water and ammonia [20].

The work presented here is inspired by another natural phenomenon: we use colloidal systems and self-assembly to imitate the shape specificity seen in enzymes. In 1894, Fischer proposed that enzymes would preferentially bind to substrates whose shape was complementary to that of the active site - this became known as the "lock and key" model [136]. Using spherical colloidal particles as "keys" and the dimpled colloidal particles designed by Sacanna et al. [50, 51] as "locks", we are able to utilise depletion induced attractions to emulate the specific binding interactions predicted by enzyme behaviour. More explicitly, we investigate the effect of depletant size and concentration, lock particle shape, and both lock and key concentration on the lock-key binding behaviour of a binary system in a monolayer at a single featureless wall. Similar work has been carried out by Sacanna et al. [50], but here the particle concentration and shape were not explicitly probed.

We begin by describing the theoretical background behind lock-key binding in section 6.2. We then provide the experimental details in section 6.3, and present and discuss the results in section 6.4. Finally, we conclude in section 6.5.

6.2 Theory

In order to investigate the expected lock-key binding behaviour, we here follow Sacanna et al. [50] and consider the equilibrium reaction, $L + K \rightleftharpoons LK$, as shown in figure 6.1. We can use the

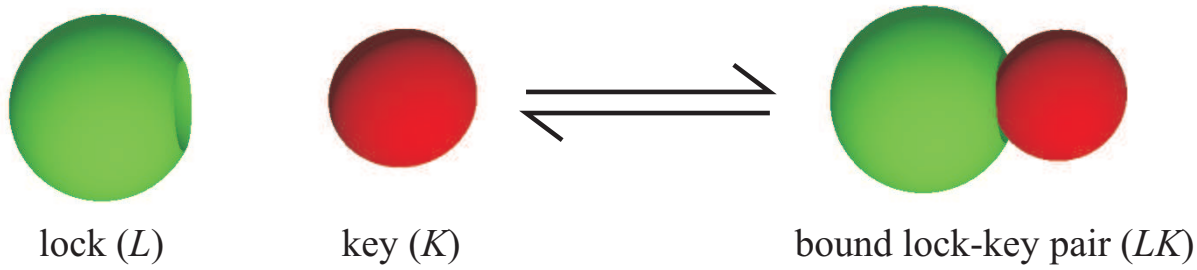

Figure 6.1: The equilibrium between the dimpled "lock" particles and the small spherical "key" particles.

law of mass action to write,

$$\frac{[LK]}{[L^f][K^f]} = K_{eq}, \tag{6.1}$$

with $[LK]$, $[L^f]$ and $[K^f]$ the number densities of bound lock-key pairs, free locks and free keys, respectively, and K_{eq} the equilibrium constant [137]. Further information can be extracted following the model presented in [50], which gives an explicit expression for K_{eq}:

$$\frac{N_{LK}}{N_L^f N_K^f} = \frac{K_{eq}}{V} = \frac{C}{V} \mathrm{e}^{-\frac{E_b}{k_\mathrm{B}T}}, \tag{6.2}$$

with N_X the number of species X, V the volume (in this case taken to be the area of the image multiplied by the gravitational length of the large particles, which was approximately 200 nm), C a prefactor, and E_b the binding energy. It is clear therefore, from eq. (6.2), that for a given polymer size and lock particle shape, there is a direct link between the equilibrium constant, which may be found by fitting the experimental data, and the binding energy, which we may calculate.

The calculation of the binding energy is done following Sacanna et al. [50]. We begin by computing the total interaction energy between a lock and key pair, given by the sum of the electrostatic repulsion and the depletion attraction, similarly to chapter 5. The former is defined as,

$$U_{el}(d) = E_{el} \mathrm{e}^{-d\kappa}, \tag{6.3}$$

with d the interparticle separation and $E_{el} = 64 k_\mathrm{B} T \rho \kappa^{-1} A_{el} \tanh^2\left(\frac{e\psi_0}{4k_\mathrm{B}T}\right)$, where k_B is Boltzmann's constant, T is the temperature, ρ is the salt concentration in mol m^{-3}, κ^{-1} is the Debye

screening length (defined in eq. (5.2)), e is the elementary charge, ψ_0 is the surface potential of the particles, and $A_{el} = 2\pi\kappa^{-1}\frac{R_L R_K}{R_L+R_K}$, with R_L the radius of the lock particle, and R_K the key particle radius. The above is strictly for spherical particles, but, as in chapter 5, we assume a negligible deviation due to the dimple. For the case of dimpled locks, we may write the depletion attraction as,

$$U_{dep}(d) = E_{dep}\left(1 - \frac{d}{2R_g}\right), \tag{6.4}$$

where $E_{dep} = -k_{\mathrm{B}}Tn_pV_{ov}(0)$ with R_g the polymer radius of gyration, n_p the polymer number density, and $V_{ov}(0)$ the overlap volume of the depletion zones at zero separation, found using arguments presented in the appendix. When considering the depletion attraction between two spherical particles, we are no longer required to assume a linear decay and instead we may write,

$$U_{dep}(d) = -k_{\mathrm{B}}Tn_pV_{ov}(d), \tag{6.5}$$

with,

$$V_{ov}(d) = \frac{\pi\left(d-2R_g\right)^2\left(d^2+4d\left(R_g+R_K+R_L\right)+4\left(3R_KR_L+R_g\left(R_K+R_L\right)\right)\right)}{12\left(d+R_K+R_L\right)}. \tag{6.6}$$

The total interaction energy, $U_{tot}(d)$, for lock and key binding is thus,

$$U_{tot}(d) = U_{el}(d) + U_{dep}(d), \tag{6.7}$$

and the binding energy is simply given by eq. (6.7) evaluated at its minimum.

6.3 Experimental details

In order to study depletion induced binding in a binary mixture of particles, suspensions of the small spherical particles, hereafter known as "keys", were used, combined with either the large spherical particles, or the large dimpled particles acting as the "locks". All particles used were those described in chapter 2. The larger particles had a diameter of 2.56 μm, and a polydispersity of 4%, as measured by static light scattering. The dimple was found to be $\sim$ 1.3 μm wide and $\sim$ 200 nm deep, as determined by scanning electron microscopy and atomic force microscopy,

respectively. The small spherical particles had a diameter of 1.72 μm, and a polydispersity of 5%, as measured by static light scattering. These dimensions meant that the smaller spherical particles fitted well into the cavities of the dimpled particles, leaving us with "lock and key" colloids, as described by Sacanna et al. [50, 51]. Similarly to the work presented in chapter 5, the colloidal particles were suspended in deionised water and a polymer was added to induce depletion interactions between the particles - in this case xanthan and poly(ethylene oxide) (PEO), both with additional salt (NaCl), were prepared as outlined in chapter 2 and used.

As in chapter 5, we studied the quasi-two-dimensional behaviour of the particles, and thus had to wait for at least two hours after sample preparation to ensure that all the particles had sedimented before any observation could take place. It should be noted that, as detailed in section 2.4, the gravitational lengths of the lock and key particles were 0.2 μm and 0.7 μm, respectively. This meant that while both types of particles fell to the bottom of the container, the keys were not completely prevented from diffusing upwards to effect lock-key binding.

Numerous samples were prepared in order to allow us to investigate the role of particle shape, depletant size and concentration, and both the absolute and relative concentrations of the two different colloidal particles on the depletion interactions of binary colloidal suspensions. Once more, the variables of interest were the colloidal *area* fractions, and the polymer *volume* fraction. Polymer volume fractions of $\phi_p \approx 0$, 0.25, 0.5 and 0.75 were used, and multiple colloidal area fractions (ϕ_l^a for the lock particles and ϕ_k^a for the keys) were employed, ensuring that the total colloidal area fraction was never more than 0.5, i.e. $\phi_l^a + \phi_k^a \leq 0.5$.

As in previous chapters, the samples were contained within a homemade cell made from a small (10 mm in diameter) bottomless glass vial, which had been glued onto a glass coverslip and subsequently plasma-cleaned to prevent any particles from sticking to the walls. Each sample had a volume of 200 μl, implying that the corresponding sample height was approximately 2.5 mm. Samples were left to sediment completely, forming a monolayer on top of the coverslip, which was then observed using a Zeiss LSM 5 Exciter confocal microscope, equipped with a 63× oil immersion objective. Two laser channels were used to separately excite the two different dyes used in the large and small particles, allowing for more convenient image analysis. It was found that the dye for the key particles was less tightly bound than anticipated, and as such reflection was used rather than fluorescence to observe the particles. This meant that only the very centres of the particles were seen, but this had no effect on our image analysis routines.

For each sample, movies of 150 frames were recorded, where each frame was 51.2 μm × 51.2 μm in size. The 2D coordinates of each particle were then found using standard image analysis routines (see section 2.9) [82], with additional steps to split the experimental image into the two independent laser channels.

6.4 Results and discussion

In order to probe the depletion induced binding of binary colloidal suspensions, we must first provide a definition for what constitutes a bound lock and key pair. This is done by introducing a centre-to-centre distance criteria: if the coordinates of the centres of the lock and key particles are within a certain distance of each other (in this case 2 μm, as the sum of the two radii is 2.14 μm), then the pair is classified as "bound". This method provides us with a relatively high degree of accuracy but is not completely foolproof, and may cause some keys to be labelled as bound, when in fact they are just close to the corresponding lock particle (figure 6.2). This is due to the slight polydispersity of the samples, and the minor imperfections in the tracking algorithm caused by the particle shape anisotropy.

Once the bound lock and key pairs have been identified, we may quantify the binding behaviour in two ways. Firstly, we can plot the fraction of bound key particles against the ratio of keys to locks. This will allow us to compare the trends seen for different polymer concentrations, depletant sizes and lock particle shapes. However, in order to gain a fuller understanding of the binding we must account not only for the relative concentrations of colloidal particles, but also for the total number, as this could have an effect on the system's behaviour. A three-dimensional plot is thus created, containing information pertaining to the number of

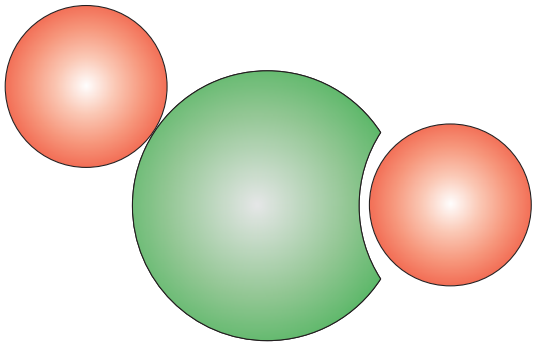

Figure 6.2: An example of a dimpled lock particle with two potentially bound keys.

lock particles, the number of key particles, and the fraction of bound keys.

The model presented in section 6.2 is used to fit the data presented in the 3D plots to give a value of the equilibrium constant, K_{eq}. As explained previously, this should be linked to the calculated binding energy, and we expect to find that a larger value of K_{eq} corresponds to a more favourable binding energy.

We can further qualify the binding behaviour of the lock and key mixtures by computing a mixed binary radial distribution function. This is similar to that used in chapters 4 and 5, but now we find the distance between the lock and key particles, rather than that between two like particles.

6.4.1 Polymer concentration

We begin by investigating the role of polymer concentration on the depletion induced binding of lock and key colloidal particles. In this case, only dimpled lock particles are used, and the polymer employed is PEO with NaCl. This depletant system was chosen as it was shown in chapter 5 to provide the most shape selective behaviour. Typical experimental snapshots for various polymer concentrations are given in figure 6.3. These illustrate both the upper and lower limits of the ratio of the number of keys (N_K) to the number of locks (N_L). In each image, the key particles are circled, where green circles indicate keys that are bound to lock particles (a bound pair is as described above), and red circles designate free key particles. These images immediately provide three important results: (a) as we increase the concentration of polymer, the depletion interaction becomes stronger, leading to more ordering in the system; (b) more lock-key binding occurs as we raise the polymer concentration; and (c) as we increase the ratio of N_K to N_L, the fraction of key particles that are bound to lock particles decreases. Figure 6.4 illustrates these trends further.

We know from chapter 5 that the strength of the depletion interaction is directly proportional to the number, and therefore concentration, of depletants. This explains why an increase in both general ordering, and lock-key binding is seen as the polymer concentration increases. An exception to this pattern is when $\phi_p = 0.75$. Figure 6.4 shows much less lock-key binding than would be expected in this case, and we rationalise this by speculating that the depletion interaction is now too strong and induces clustering in three dimensions, and thus not all parti-

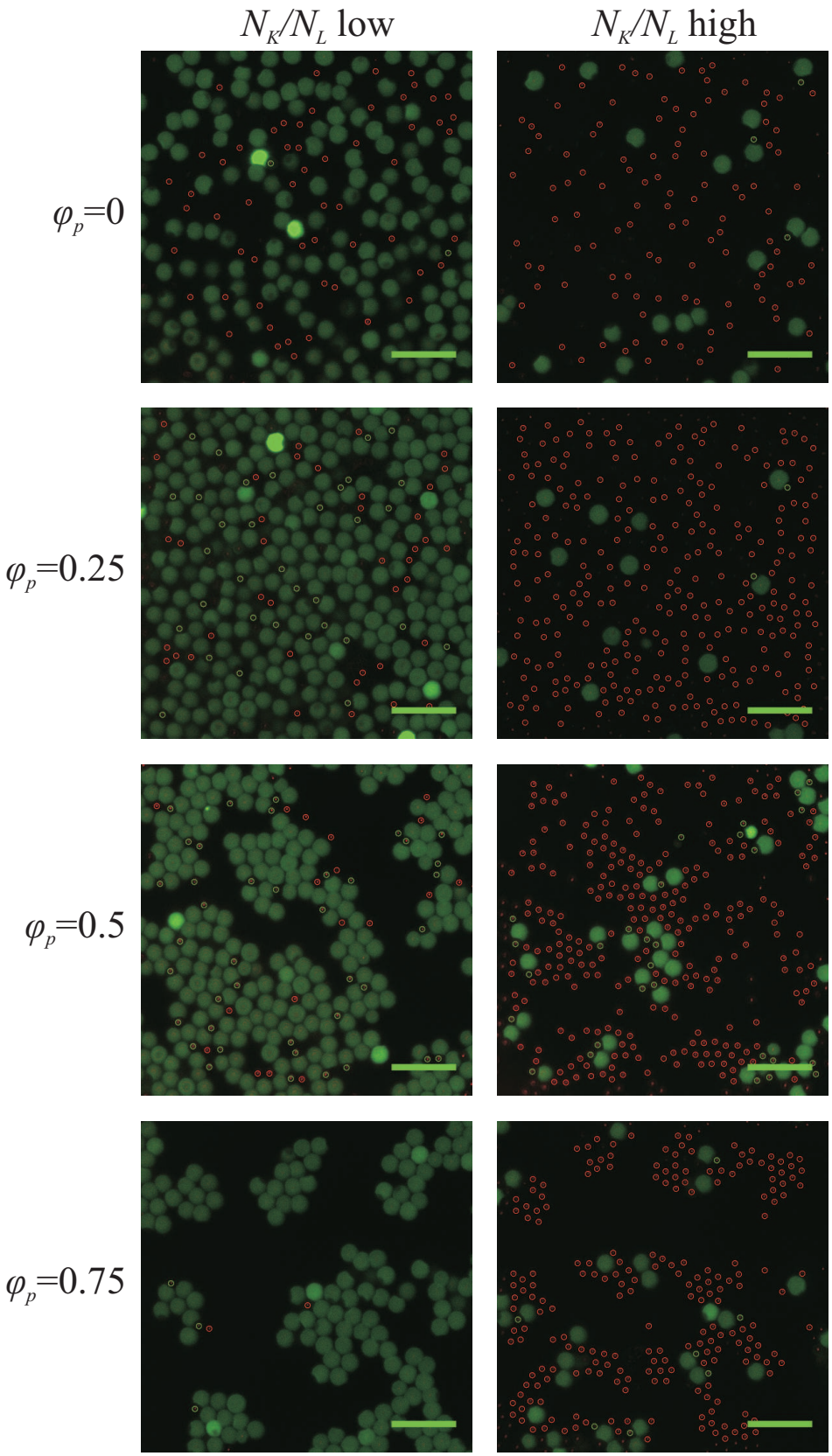

Figure 6.3: Typical confocal images of dimpled lock particles with key particles at various concentrations of PEO and NaCl. Both the upper and lower limits of N_K/N_L are shown and bound keys are indicated by green circles. Scale bars are 10 μm.

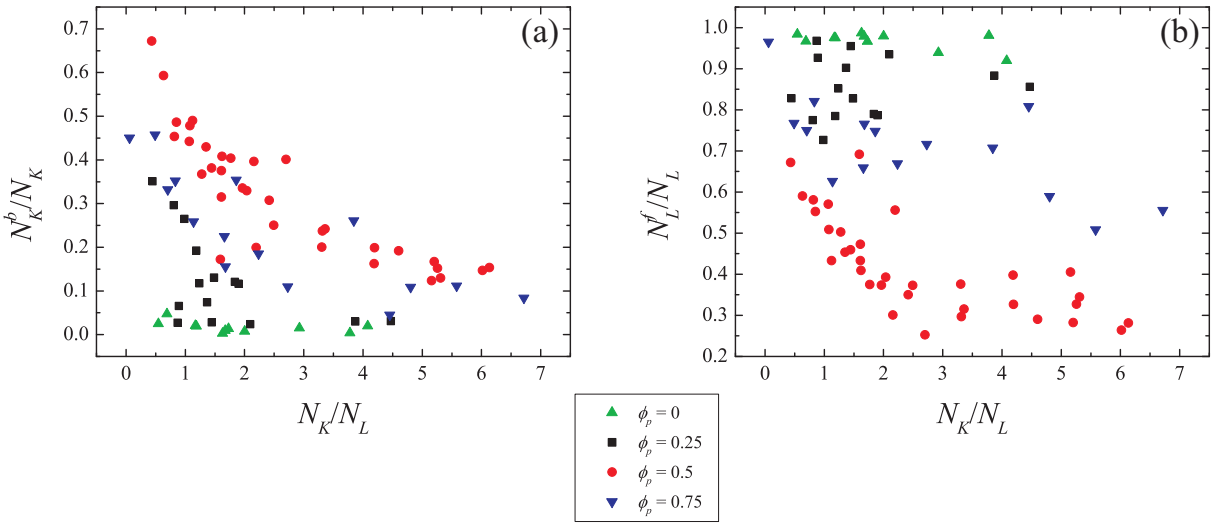

Figure 6.4: (a) The fraction of bound key particles (N_K^b/N_K), and (b) the fraction of free (unbound) lock particles (N_L^f/N_L), both as a function of the ratio of the number of key particles to lock particles for various different polymer concentrations. Free locks are found separately to the bound keys, just in case more than one key is found to be bound to one lock.

cles are visible in the plane of observation. A similar effect is seen in chapter 5. For this reason, all data acquired when $\phi_p = 0.75$ is hereafter dismissed.

An explanation for the observation that the amount of lock-key binding seen decreases as the ratio of keys to locks increases, regardless of polymer concentration, is provided by examining the images in figure 6.3. At low values of N_K/N_L there are few key clusters, and instead the keys are sparsely and relatively evenly distributed throughout the sample meaning there is ample opportunity for binding. Conversely, in the limit of high N_K/N_L values, the keys form large clusters, meaning that fewer particles are available for binding to locks.

We further corroborate our findings using mixed binary radial distribution functions (see figure 6.5). It is clear once more that at both high and low values of N_K/N_L, an increase in polymer concentration leads to a slight increase in translational ordering, as demonstrated by a slower decay of the radial distribution function. We also see that a split in the first peak of the radial distribution function becomes more prominent as the polymer concentration increases, particularly when the ratio of keys to locks is low. This is indicative of lock-key binding and is caused by the small key particle fitting into the cavity of the dimpled lock particle.

Finally, figure 6.6 presents the three-dimensional plots giving the number of locks, the number of keys and the fraction of bound keys for each polymer concentration. These plots

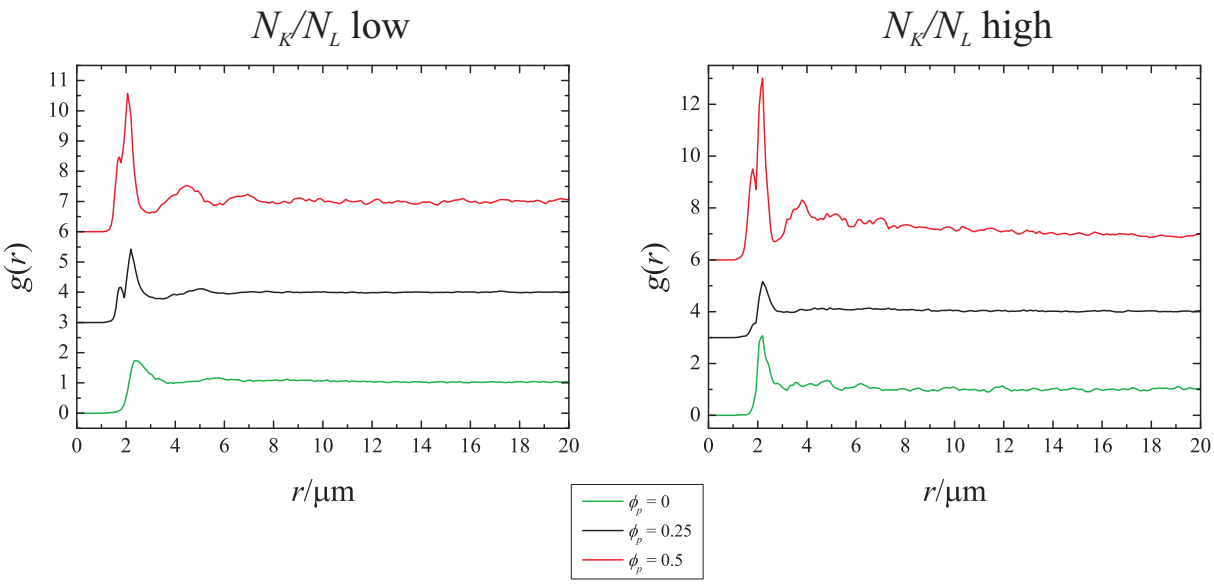

Figure 6.5: Mixed binary radial distribution functions for each polymer concentration at the upper and lower limits of N_K/N_L. Graphs have been vertically shifted for clarity.

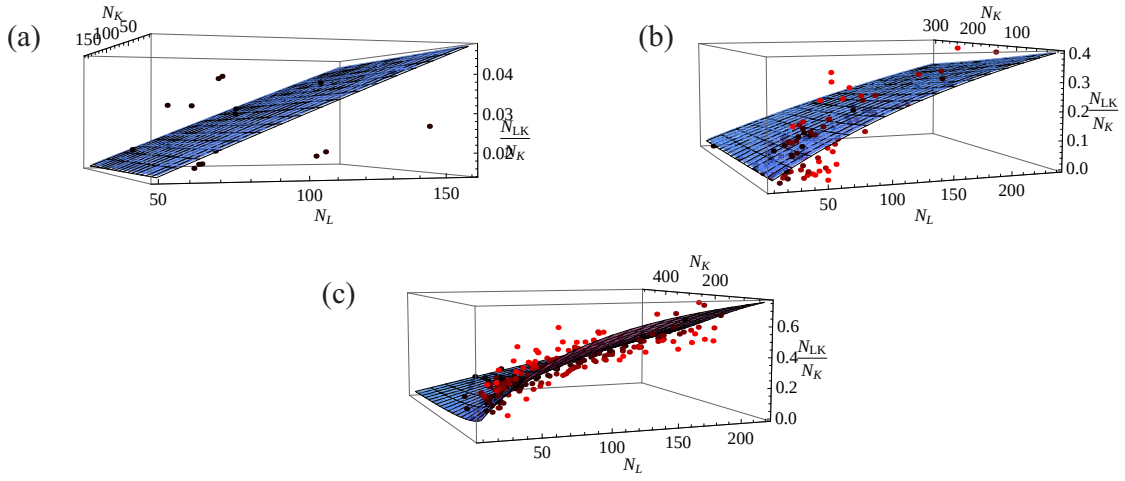

Figure 6.6: The number of locks, the number of keys, and the fraction of bound keys for dimpled locks and PEO at a volume fraction of (a) $\phi_p = 0$, (b) $\phi_p = 0.25$, and (c) $\phi_p = 0.5$. The surfaces give the mathematical fit of the experimental data points to the model presented in section 6.2.

ϕ_p	K_{eq}/V(experimental)	E_b/k_BT (calculated)
0	0.0003	0
0.25	0.0028	-12.14
0.5	0.0152	-37.07

Table 6.1: Values for the equilibrium constant and binding energy for various concentrations of PEO with dimpled lock particles.

indicate that it is the number of locks, and not keys, that has the greater effect on the number of bound lock-key pairs. Using the model outlined in section 6.2, we are able to both calculate the predicted binding energy, E_b, and fit the experimental data points to obtain a value for the equilibrium constant, K_{eq}. These values are given in table 6.1, and reinforce our findings that the degree of lock-key binding increases with polymer concentration.

6.4.2 Polymer size

We next turn our attention to the effect of polymer size on the binding behaviour of suspensions of lock and key colloids. Once more, only dimpled lock particles are used, but now either xanthan or PEO, both with additional NaCl, are utilised as depletants at a fixed concentration of $\phi_p = 0.5$. Figure 6.7 provides example experimental snapshots of the systems under investigation at both extremes of N_K/N_L. Again, the keys designated as bound are highlighted with green circles. As in the previous section, we see that the amount of lock-key binding decreases as the ratio

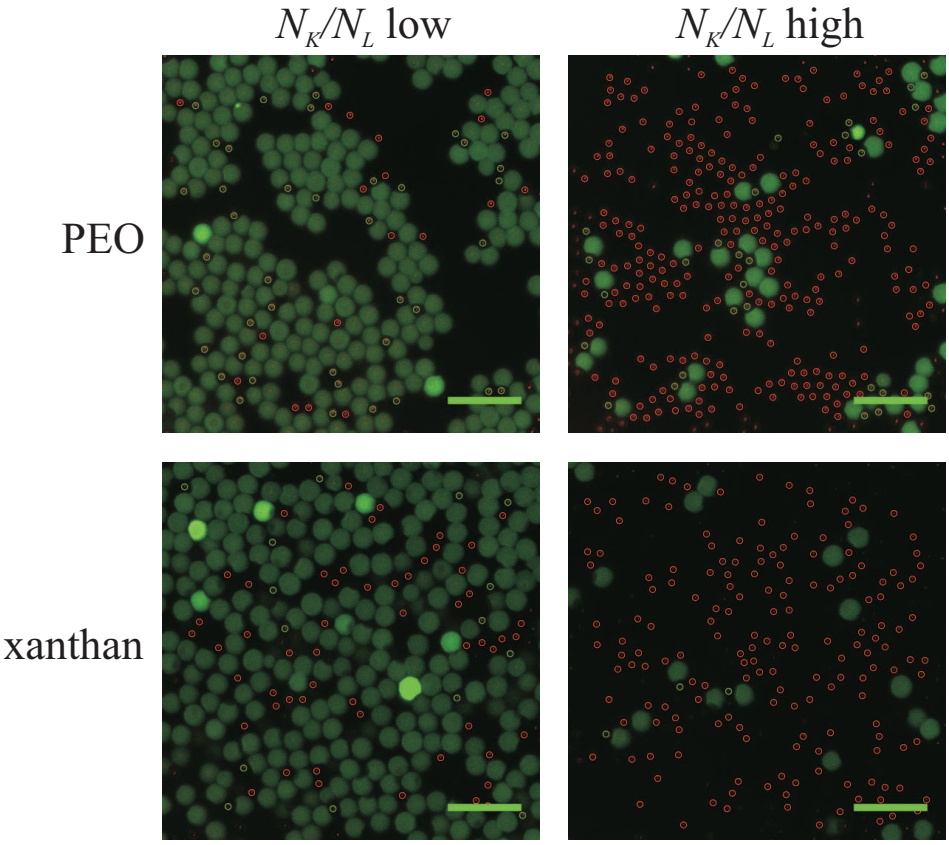

Figure 6.7: Typical confocal images of dimpled lock particles with key particles and either xanthan or PEO as a depletant at a concentration of $\phi_p = 0.5$. Both the upper and lower limits of N_K/N_L are shown and bound keys are indicated by green circles. Scale bars are 10 μm.

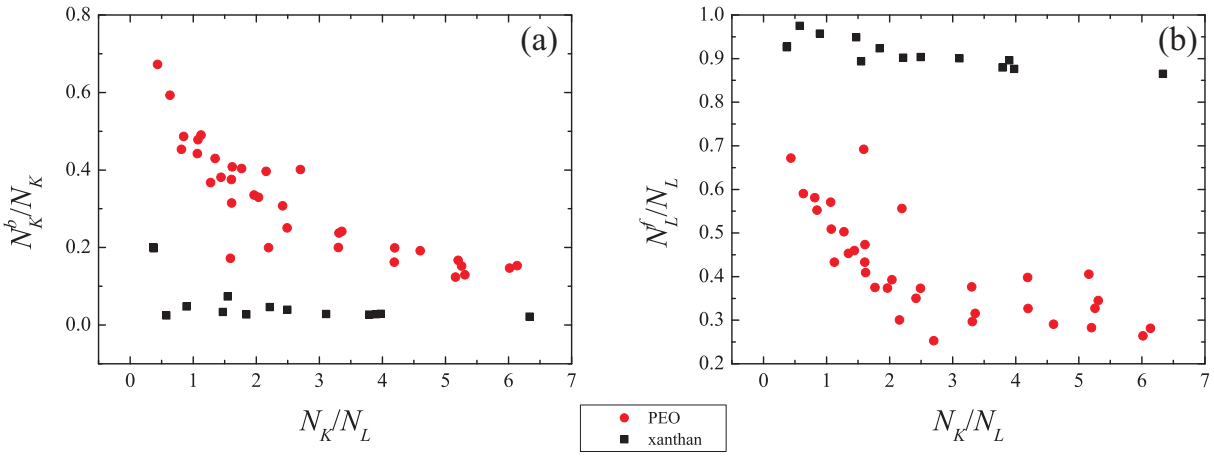

Figure 6.8: (a) The fraction of bound key particles (N_K^b/N_K), and (b) the fraction of free (unbound) lock particles (N_L^f/N_L), both as a function of the ratio of the number of key particles to lock particles for PEO and xanthan at $\phi_p = 0.5$. The free locks are found separately to the bound keys, just in case more than one key is found to be bound to one lock.

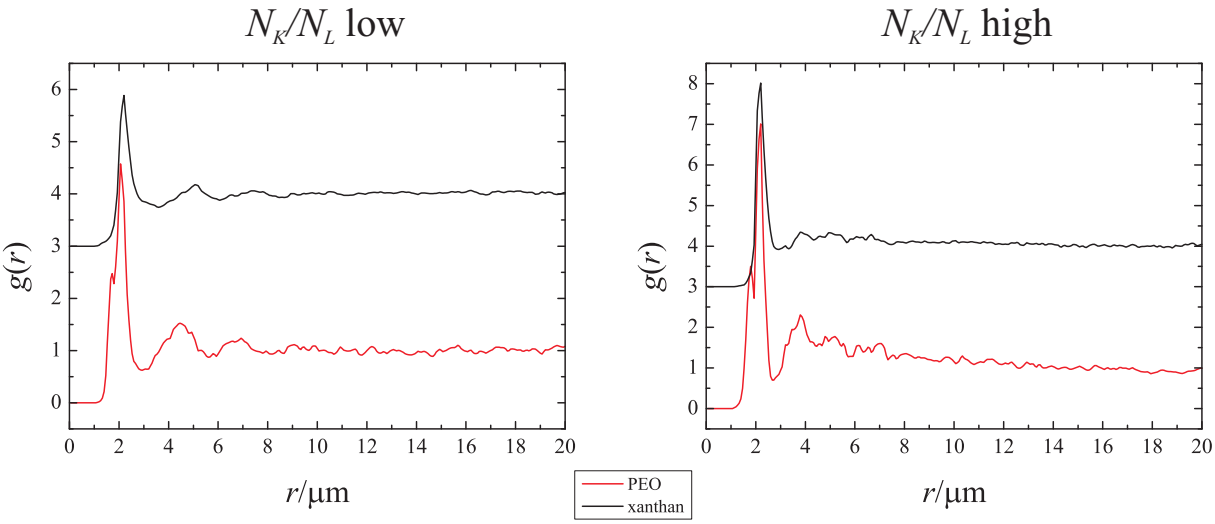

Figure 6.9: Mixed binary radial distribution functions for each depletant (both at $\phi_p = 0.5$) at the upper and lower limits of N_K/N_L. Graphs have been vertically shifted for clarity.

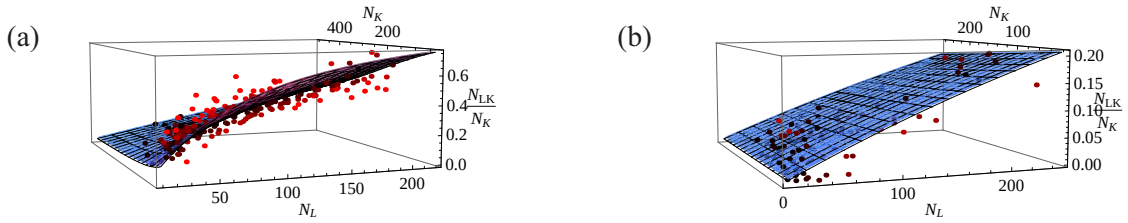

Figure 6.10: The number of locks, the number of keys, and the fraction of bound keys for dimpled locks and (a) PEO, and (b) xanthan, both at $\phi_p = 0.5$. The surfaces give the mathematical fit of the experimental data points to the model presented in section 6.2.

Polymer	K_{eq}/V(experimental)	$E_b/k_{\mathrm{B}}T$ (calculated)
PEO	0.0152	-37.07
xanthan	0.0011	-7.54

Table 6.2: Values for the equilibrium constant and binding energy for systems of dimpled lock particles using PEO and xanthan.

of keys to locks increases. Additionally, we find that the degree of ordering within the system, and more importantly the extent of the lock-key binding, is less for xanthan than for PEO. This is further illustrated by considering the fraction of both bound keys and free locks, as in figures 6.8 and 6.10, and the mixed binary radial distribution functions given in figure 6.9. The latter show that there is more overall ordering for a system with PEO, as well as more lock-key binding, demonstrated by the slower $g(r)$ decay and the presence of a split first peak, respectively. Once more, we are able to obtain values for the equilibrium constant and binding energy (see table 6.2); these corroborate our results and show that binding is much more likely for a system with PEO than one with xanthan. We may rationalise this behaviour by considering the shape of the depletion zone surrounding a dimpled particle generated by each of the two polymers under investigation (see figure 5.3). As discussed in chapter 5, a smaller polymer forms a depletion zone which more closely mirrors the shape of the particle, and hence we would expect that the spherical keys will be able to "feel" the cavity of the lock particles more strongly in a suspension of PEO, rather than xanthan.

6.4.3 Particle shape

Finally, we consider the effect of the shape of the lock particles on lock-key binding. Here, we use both the dimpled and spherical "lock" particles, along with PEO at a fixed concentration of $\phi_p = 0.5$. As in previous sections, we investigate the binding behaviour using experimental snapshots (figure 6.11), and by measuring the fraction of bound keys and free locks (figures 6.12 and 6.14). The mixed binary radial distribution function is also computed (figure 6.13).

Figure 6.11 demonstrates that while the overall order is relatively similar for both lock particle shapes, there is a significant increase in lock-key binding when the dimpled particles are used. This increase in binding is also apparent in figures 6.12 and 6.14, and is highlighted in figure 6.13 by a splitting of the first peak. We also see a much smaller equilibrium constant (and hence less favourable binding energy) for the binding of spherical particles than for the dimpled

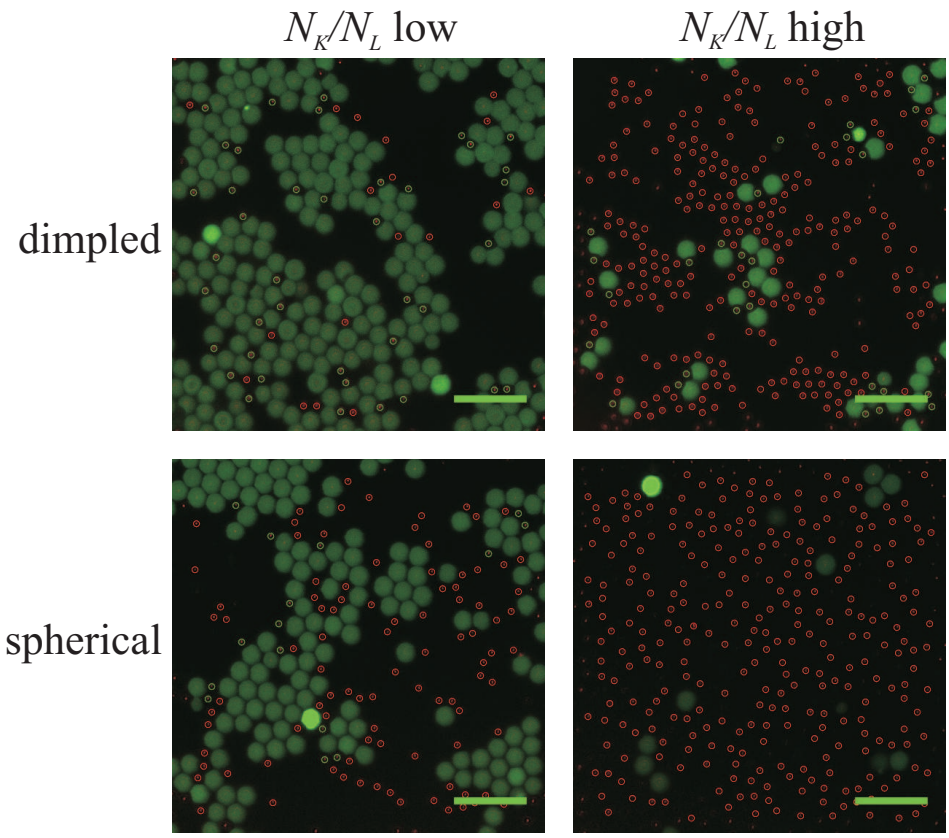

Figure 6.11: Typical confocal images of both dimpled and spherical lock particles with keys and PEO at a concentration of $\phi_p = 0.5$. Both the upper and lower limits of N_K/N_L are shown and bound keys are indicated by green circles. Scale bars are 10 μm.

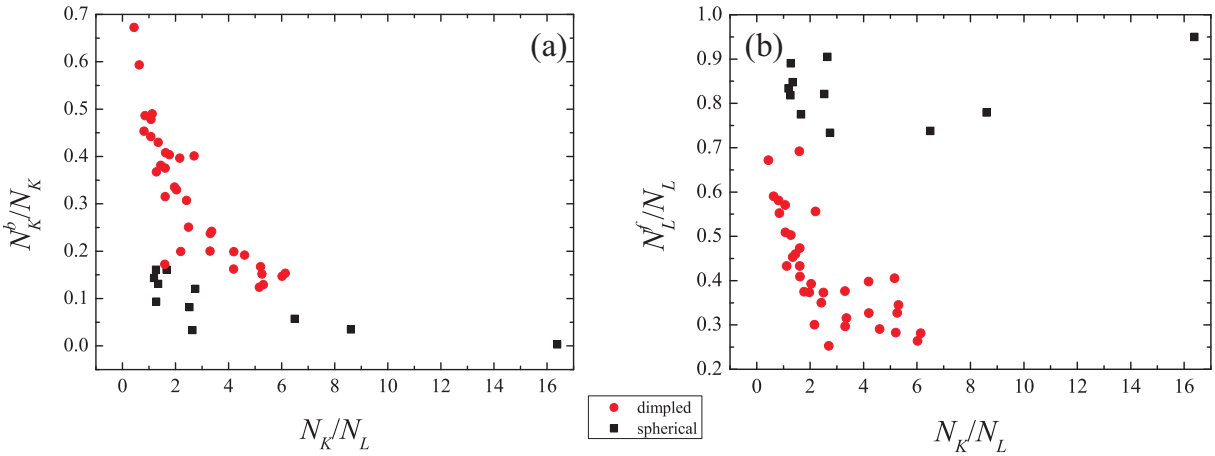

Figure 6.12: (a) The fraction of bound key particles (N_K^b/N_K), and (b) the fraction of free (unbound) lock particles (N_L^f/N_L), both as a function of the ratio of the number of key particles to lock particles for dimpled and spherical locks with PEO at $\phi_p = 0.5$. The free locks are found separately to the bound keys, just in case more than one key is found to be bound to one lock.

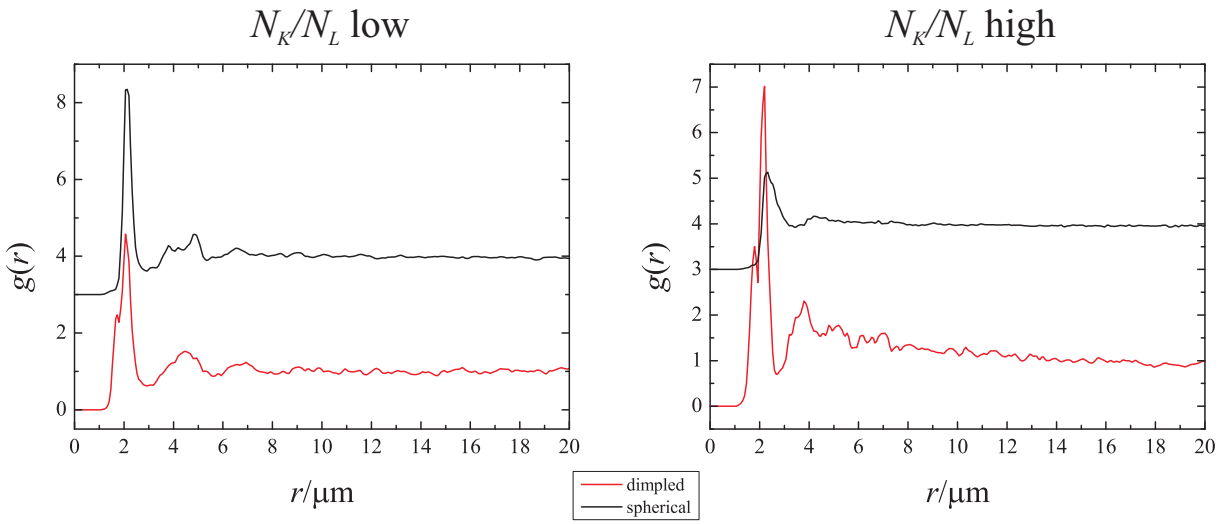

Figure 6.13: Mixed binary radial distribution functions for dimpled and spherical locks with PEO at $\phi_p = 0.5$ at the upper and lower limits of N_K/N_L. Graphs have been vertically shifted for clarity.

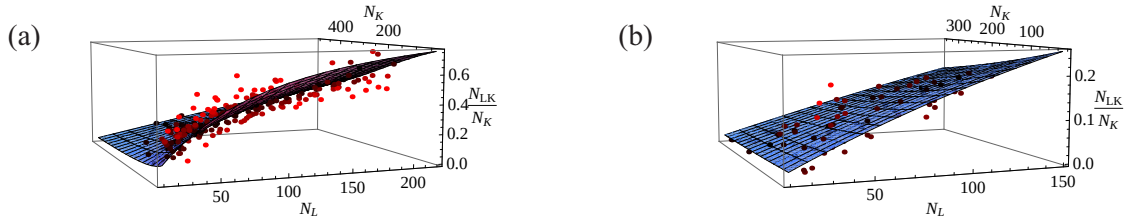

Figure 6.14: The number of locks, the number of keys, and the fraction of bound keys for (a) dimpled locks, and (b) spherical locks, both with PEO at $\phi_p = 0.5$. The surfaces give the mathematical fit of the experimental data points to the model presented in section 6.2.

particles. These observations are to be expected: unlike the dimpled particles, the spherical particles have no cavity in which to house a key, and as such the only binding we see originates from the slight errors in the way we define whether or not a key is bound to a lock, as described at the beginning of section 6.4.

Lock shape	K_{eq}/V(experimental)	E_b/k_BT (calculated)
dimpled	0.0152	-37.07
spherical	0.0024	-3.59

Table 6.3: Values for the equilibrium constant and the binding energy for systems of dimpled and spherical lock particles using PEO.

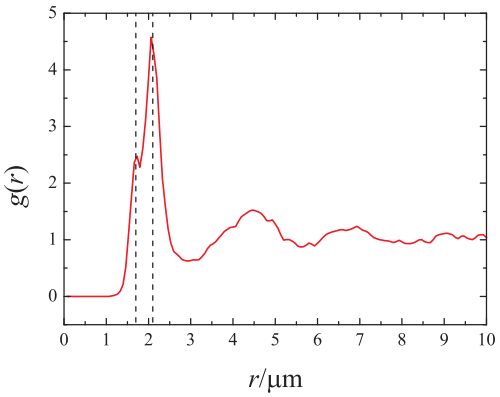

Figure 6.15: Mixed binary radial distribution function for dimpled locks with PEO at $\phi_p = 0.5$ at lower limit of N_K/N_L. Dashed lines show the position of the peaks.

6.4.4 Calculation of dimple depth

In the cases when binding is seen, we are able to extract a further piece of information from the mixed binary radial distribution function by finding the position of the splitting in the first peak. We expect the first main peak to be at $r = R_L + R_K$, with R the radius, and the subscripts L and K denoting locks and keys, respectively, and the shoulder to be at $r = R_L + R_K - 2dimp$, with $dimp$ the depth of the dimple. Figure 6.15 shows an example radial distribution function, in this case for the dimpled locks with PEO at $\phi_p = 0.5$ and low N_K/N_L. Here, we find that the main peak is at $r = 2.1$ μm, and the shoulder is at $r = 1.7$ μm. The position of the main peak is in very good agreement with the measurements of particle size carried out with static light scattering, and we are lead to calculate that the depth of the dimple is 200 nm. This, too, is consistent with previous measurements carried out to characterise the particles.

6.4.5 Self-interactions

In addition to the lock-key binding energies presented above, the lock-lock self-interactions were also computed. Table 6.4 compares the two.

We find that, in all cases, the binding energy between two locks is greater than that between a lock and a key. This is due to the larger overlap volumes generated when the second particle fits more precisely into the cavity of the first. However, the binding of two locks is restricted somewhat by the necessity of having two particles in the correct orientation, rather than just one.

Polymer	ϕ_p	Lock shape	$E_b/k_\mathrm{B}T$ (mixed)	$E_b/k_\mathrm{B}T$ (self)
PEO	0	dimpled	0	0
PEO	0.25	dimpled	-12.14	-22.24
PEO	0.5	dimpled	-37.07	-65.78
xanthan	0.5	dimpled	-7.54	-9.66
PEO	0.5	spherical	-3.59	-4.42

Table 6.4: Values for the lock-key and lock-lock binding energies for systems of dimpled and spherical lock particles using PEO and xanthan at various concentrations.

6.5 Conclusions

The depletion induced binding behaviour of lock and key colloids has been investigated using confocal microscopy and real-space image analysis. The effect of lock particle shape, as well as colloid concentration, and depletant size and concentration has been observed and characterised by counting the number of bound lock-key pairs as well as computing the mixed binary radial distribution function. The equilibrium constant for the binding reaction has also been found by modelling the experimental data with a law of mass action. We have shown that the degree of binding increases as the ratio of keys to locks decreases, due to a more even distribution of key particles across the whole field of view at low ratios, compared to the key clusters found at higher ratios. Additionally, the concentration and size of depletants has a marked effect on lock-key binding, with the highest fraction of bound keys being found for a high concentration of small polymer particles. Finally, we confirm that a small deviation in shape away from spherical leads to a large difference in depletion induced binding behaviour.

Acknowledgements We thank Michele Ceriotti for helpful discussions regarding the theoretical fit of the data.

Chapter 7

Direct measurement of depletion induced forces using optical trapping

ABSTRACT

We directly measure the depletion induced force between lock and key particles at contact using optical tweezers. The effect of depletant size and concentration is studied, as well as the shape specificity of the interparticle interaction. The latter is of particular interest and is probed by controlling the initial configuration such that three scenarios are possible: a dimpled lock particle with a key residing within the cavity, a dimpled lock particle with a key not inside the cavity, and a spherical particle with a key. We demonstrate that the magnitude of the depletion induced force is closely linked to the overlap volume between the particles, and as such is greatest when the key is held within the dimple of the lock and the polymer concentration is high. We further show that the experimental results are in semi-quantitative agreement with our theoretical predictions.

7.1 Introduction

The behaviour of colloidal systems is governed by interparticle interactions, and as such it is of utmost importance to characterise these as fully as possible. Measurements of colloidal forces have been recorded using a variety of techniques [128, 138], including surface force apparatus [139], atomic force microscopy [140,141], total internal reflection microscopy [142,143] and optical tweezers [73]; we will use the latter.

The use of optical tweezers in directly measuring colloidal forces is widespread in the literature. In many cases, one colloidal particle is held within a stationary trap, while a second particle is brought closer in small steps. At each point the particles' deviation from the equilibrium trap position is recorded, and from this, the interparticle force may be calculated [144–152]. An alternative method requires the use of "blinking" optical tweezers: two particles are held at a fixed separation, the traps are then extinguished, and the subsequent motion is monitored [153–155]. Another approach uses an optical line tweezer to confine the two particles in two dimensions, while recording the free motion in the third dimension [156,157]. In all three cases, the colloidal interaction as a function of particle separation is recovered. These techniques may also be applied to systems with additional external interactions, such as those in an electric field [158] or in the presence of depletants [159].

In this chapter, we directly measure the depletion induced force between the lock and key particles described in chapter 6. It should be noted here that both the dimpled particles and the large spherical particles are referred to as "locks", even though only the former may exhibit true lock-key binding. The dependence upon depletant size and concentration is probed, but of particular interest is the shape specificity of the interparticle interaction. Since the particles used are anisotropic in shape, we are no longer able to decouple their rotational and translational motion, and as such, experiments that require the traps to be brought together, as outlined above, are not feasible. Line tweezers are also not suitable, as the optical forces would prevent the cavity in the dimpled particle from lying along the line trap, hence precluding any lock-key binding. Instead, we begin in a configuration where the lock and key particles are touching, and subsequently increase the trap separation. We systematically vary the trap strength and monitor the point at which lock-key separation occurs, which ultimately gives us a measure for the depletion force between the particles at contact. The beauty of this technique is that the

initial orientation of the particles may be controlled, and factors such as the viscous drag need not be considered.

This chapter is structured as follows. We will begin by presenting the theoretical background behind this work in section 7.2, including the models used for the forces due to optical traps and due to depletion interactions. In section 7.3, we outline the experiments performed, the results of which are given in section 7.4. Finally, we conclude in section 7.5.

7.2 Theory

In this chapter, we directly measure the depletion induced force between lock and key particles using optical trapping. A simple force balance is used to model the interactions in the system, as illustrated in figure 7.1(a). An optical trap containing the key particle is moved away from the lock particle (held within a second, stationary trap) to provide a force to counter that produced by both the depletion interaction and the stationary trap. The force due to the viscous drag of the key particle is not considered, as this is only non-zero once the key has been pulled away from the lock. Additionally, the force due to the DLVO interaction is believed to be negligible in comparison to both the depletion and trapping forces. By calculating the forces felt by the key particle due to the optical traps at the point at which lock-key separation first occurs, we

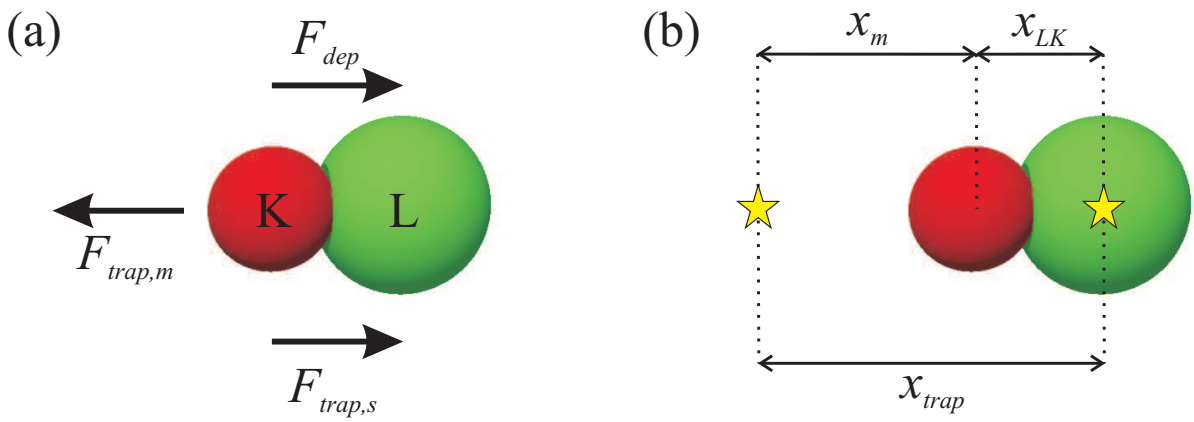

Figure 7.1: (a) Schematic showing the forces in play during the experiments. The depletion attraction, F_{dep}, and stationary trap, $F_{trap,s}$, act to hold the lock and key particles together, while the moving trap, $F_{trap,m}$, results in an opposing force to separate the particles. (b) Definitions of the lengths used. x_{trap} is the distance between the two traps (denoted by stars), x_m is the distance between the key and the moving trap, and x_{LK} is the distance between the lock and the key.

are able to obtain an approximate measure of the depletion interaction.

7.2.1 Optical forces

The potential of a single optical trap, $U_{trap}(x)$, is modelled as a simple parabola [160, 161] and can thus be written as,

$$U_{trap}(x) = \frac{1}{2}kx^2, \tag{7.1}$$

with k the trapping stiffness and x the distance from the centre of the trap. The force felt by a particle due to the presence of an optical trap is then given by,

$$F_{trap} = -\frac{\mathrm{d}U_{trap}(x)}{\mathrm{d}x} = -kx. \tag{7.2}$$

In the situation described in figure 7.1, the key particle feels the effect of both the moving and the stationary traps - the moving trap acts to separate the lock and key particles, while the stationary trap holds them together. We may calculate the total optical force acting on the key particle at the point of lock-key separation by considering the contributions from both traps present, remembering that they are acting in opposition,

$$F_{trap,tot} = F_{trap,s} - F_{trap,m} = -kx_{LK} + kx_m = -k(x_{LK} - x_m), \tag{7.3}$$

with $F_{trap,s}$ the force due to the stationary trap, $F_{trap,m}$ the force due to the moving trap, x_{LK} the distance between the centre of the lock and the centre of the key (i.e. the distance between the key and the centre of the stationary trap), and x_m the distance between the key and the centre of the moving trap (see figure 7.1(b)). Both traps are of the same stiffness, k.

7.2.2 Force due to the depletion interaction

Similarly to chapter 6, we may model the depletion interaction between a lock and key pair to provide a theoretical comparison to our experimental data. As we are able to measure only the force, not the potential, due to depletion, we relate the potentials given by eqs. (6.4) and (6.5) for dimpled and spherical locks, respectively, to forces using the relation $F = -\frac{\mathrm{d}U}{\mathrm{d}d}$. The

approximations used during the derivations of these potentials will be discussed in section 7.4. We recall that d is the separation between particle surfaces, but here we rewrite the forces in terms of the centre-to-centre separation, x_{LK}, and obtain,

$$F_{dep,d} = -\frac{k_{\mathrm{B}}Tn_pV_{ov}(R_L + R_K)}{2R_g}, \tag{7.4}$$

for the dimpled locks with keys, and,

$$F_{dep,sp} = \frac{k_{\mathrm{B}}Tn_p\pi}{4x_{LK}^2}\left(2R_g + R_K + R_L - x_{LK}\right)\left(2R_g + R_K + R_L + x_{LK}\right)\left(\left(R_K - R_L\right)^2 - x_{LK}^2\right), \tag{7.5}$$

for the spherical particles with keys, with k_{B} Boltzmann's constant, T the temperature, n_p the polymer number density, $V_{ov}(R_L + R_K)$ the overlap volume at contact, R_g the polymer radius of gyration, R_L the lock particle radius, and R_K the key particle radius. At the point of particle contact, $x_{LK} = R_L + R_K$, and eq. (7.5) simplifies to,

$$F_{dep,sp} = -4\pi k_{\mathrm{B}}Tn_p\left(\frac{R_gR_KR_L\left(R_g + R_K + R_L\right)}{\left(R_L + R_K\right)^2}\right). \tag{7.6}$$

7.3 Experimental details

Similarly to the previous chapter, a combination of small, spherical "key" particles and larger "lock" particles was used. As explained in chapter 2, the keys had a radius of 0.86 μm and a polydispersity of 5%, as measured by static light scattering. Large dimpled and spherical particles (both termed "locks") were used in this work, and both had a radius of 1.28 μm with a polydispersity of 4%, again determined by static light scattering. The dimpled particles were found to have a cavity of depth $\sim$ 200 nm, and width $\sim$ 1.3 μm, as measured by atomic force microscopy and scanning electron microscopy, respectively. These dimensions allowed for the complementary fitting of the keys into the dimpled locks. All systems were suspended in deionised water, and, as in previous chapters, various polymer solutions were added to generate a depletion attraction, namely xanthan and poly(ethylene oxide) (PEO), both with additional salt (NaCl).

Samples consisting of key particles and either dimpled or spherical lock particles were

prepared at very low colloidal volume fractions ($\phi_c < 10^{-5}$). To these, polymer solutions were added allowing us to investigate systems containing PEO with $\phi_p = 1$, 1.5, 2, 2.5, and 3, and xanthan with $\phi_p = 3$. The sample cell was constructed using a microscopy slide, two strips of double-sided sticky tape, and a small (22 mm × 22 mm) glass coverslip. The sticky tape formed a narrow channel which was filled using capillary action, and the cell was sealed with Araldite. All glass was plasma-cleaned before the cell was constructed to prevent the particles sticking to the walls.

In order to probe the strength of the depletion induced force between lock and key particles, two optical traps were generated using the system described in section 2.8. One lock particle and one key particle were held in the traps at an initial separation of 2 μm, to ensure that the two particles were touching. As shown in figure 7.2, three starting configurations were possible: a dimpled lock with a bound key, a dimpled lock with an unbound key, and a spherical lock with a key. Here, we use the term "bound" to describe the case of a key particle that is residing in the cavity of the lock particle, and "unbound" is used otherwise. The trap containing the key particle was moved away from the lock particle in steps of 10 nm at a rate of 60 steps per second over a total distance of 3 μm (corresponding to a velocity of less than one particle radius per second), and an image containing both particles was taken at each step. The experiment was then reset and repeated multiple times while systematically varying the current supplied to the laser, which in turn altered the laser power. The power delivered to the laser setup was found to depend linearly on the current, as expected. The current corresponding to the lowest laser power at which it was possible to separate the key from the lock was recorded. If the

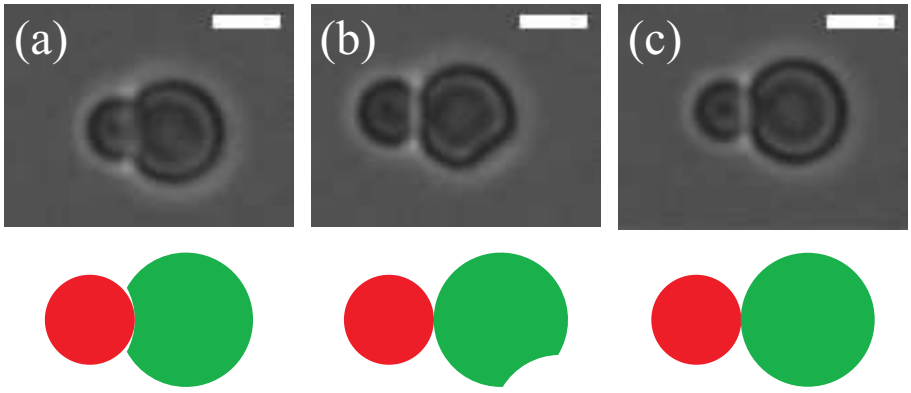

Figure 7.2: Experimental snapshots (top row) and 2D sketches (bottom row) illustrating the three possible starting configurations. When using dimpled lock particles it is possible to start in either the (a) bound or (b) unbound configuration. Spherical lock particles are also used as shown in (c). Scale bars are 2 μm.

trap strength was such that the key was pulled away from the lock, the interparticle separation was found as a function of time using particle tracking methods similar to those presented in section 2.9.2.

To provide a quantitative measurement of the depletion induced force, it was necessary to characterise the potential energy of a single optical trap. To do this, a key particle was held in a trap and its centre of mass coordinates were recorded over 10^6 frames at a frame rate of approximately 1500 frames per second. The probability distribution of these coordinates may be related to the trap potential, as $P(x) \propto \exp\left(-U_{trap}(x)/k_{\mathrm{B}}T\right)$ [162–168]. Using eq. (7.1), we model the optical potential as parabolic, and thus a fit of $-2k_{\mathrm{B}}T\ln\left(P(x)\right)$ against x provides us with a value of k. Similarly to the main lock-key separation experiment, this characterisation was carried out at various laser powers, as controlled by the current.

7.4 Results and discussion

Experimental snapshots are given in figure 7.3. These clearly indicate the two possible outcomes of each experiment: either the key is pulled away from the corresponding lock, or the lock and

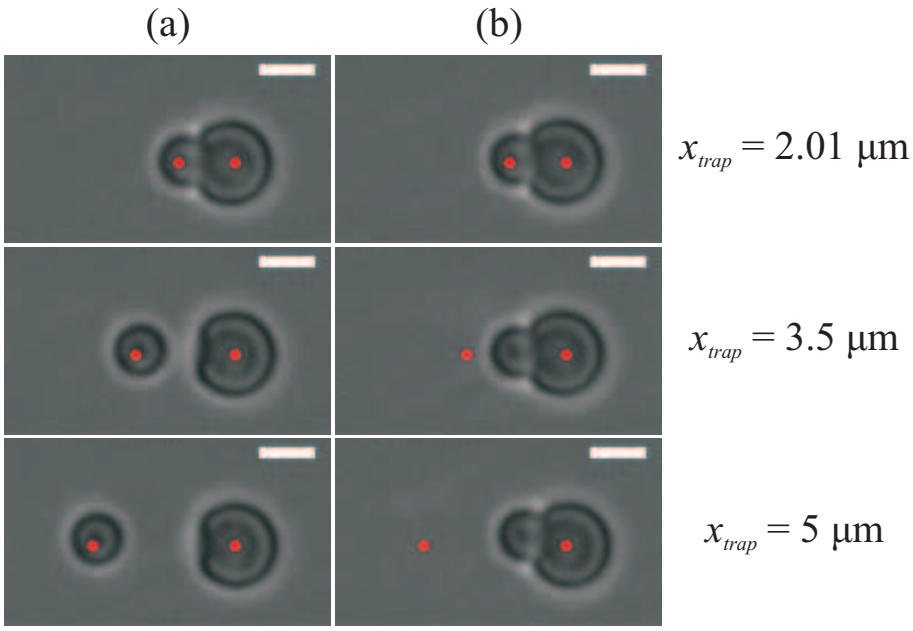

Figure 7.3: Experimental snapshots for both possible scenarios: either (a) the key is pulled away from the corresponding lock, or (b) the lock and key remain held together. The red dots indicate the position of the traps, and x_{trap} is the trap separation (see figure 7.1(b)). Scale bars are 2 μm.

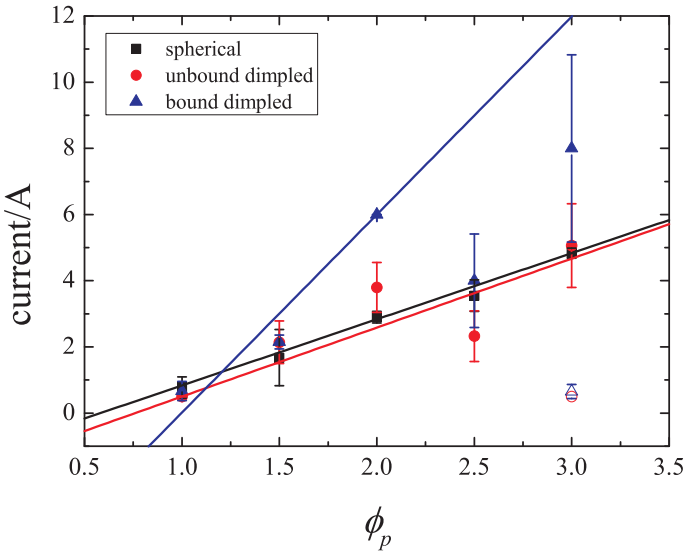

Figure 7.4: Lowest current required for lock-key separation as a function of polymer concentration for the three possible configurations. Filled symbols represent data obtained with PEO, and empty symbols denote those measured with xanthan. Error bars are from repeated experiments. Solid lines show linear fits to the data.

key remain held together. As explained in section 7.2, in order to determine the strength of the depletion induced force, we consider only the cases in which the lock and key are separated using the weakest trap possible.

The relationship between polymer concentration and the lowest current required to separate the lock and key particles is given in figure 7.4 for bound dimpled locks, unbound dimpled locks and spherical locks. We note that the data fits do not pass through the origin, and thus demonstrate semi-quantitative trends only. This plot shows that in all cases, the current needed to pull the particles apart increases with polymer volume fraction. This agrees with the fact that the depletion interaction scales with the number density of polymers, as explained in chapters 5 and 6. Additionally, we find that the current required for separation for unbound dimpled locks and spherical locks is similar, while a larger current is necessary for bound locks. This suggests that the depletion induced force between a bound lock and key pair is stronger than for the unbound case, which is to be expected due to the complementary fitting of the keys into the cavity of the dimpled locks, resulting in a greater overlap volume. An unbound dimpled lock is expected to behave similarly to a spherical lock as the shape felt by the key particle is the same in both cases.

Figure 7.4 also demonstrates the effect of polymer size on the magnitude of the force due

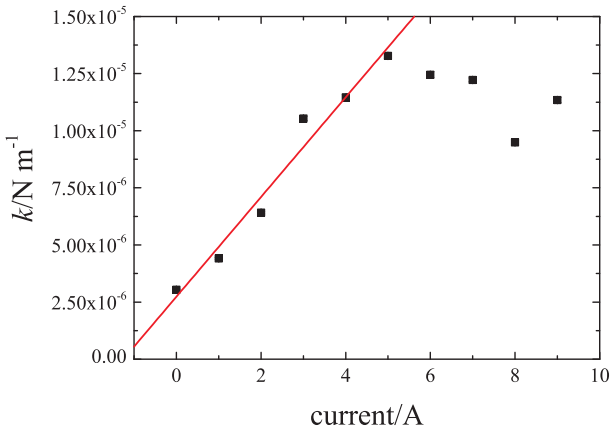

Figure 7.5: Trapping stiffness, k, as a function of current. The red line represents a linear fit to the data up to a current of 5 A.

to depletion. When xanthan (R_g = 222 nm) is used as a depletant, a much smaller current is required to separate the lock and key particles than when PEO (R_g = 57 nm) is used. Figure 5.2 shows that the depletion attraction becomes weaker as the polymer radius of gyration increases, provided the polymer volume fraction remains constant, and our observations are in agreement with this.

In order to obtain a semi-quantitative measure of the depletion induced force between the locks and keys, we refer to section 7.2 and see that more information is required: namely the trapping stiffness, k, at each laser power, and the distances, x_m and x_{LK}, between the key particle and both the moving trap and the lock particle, respectively, at the point of lock-key separation.

Figure 7.5 shows how k varies with the laser current. It can be seen that up to 5 A, the trapping stiffness is linearly dependent upon current and, in turn, laser power, as expected [168]. At higher currents, the particle is held so tightly within the trap that the deviations from the equilibrium position are too small to resolve, and thus we get an apparent plateau in trapping stiffness. From figure 7.4 we find that, for the majority of experiments, a current of 5 A or less was used, and hence we determine the relationship between stiffness and current using only the data points within the linear regime.

Plots of the centre-to-centre lock-key separation, x_{LK}, as a function of time are shown in figure 7.6 for dimpled bound locks, dimpled unbound locks and spherical locks at various polymer concentrations. Included in these plots is a line showing the separation between the

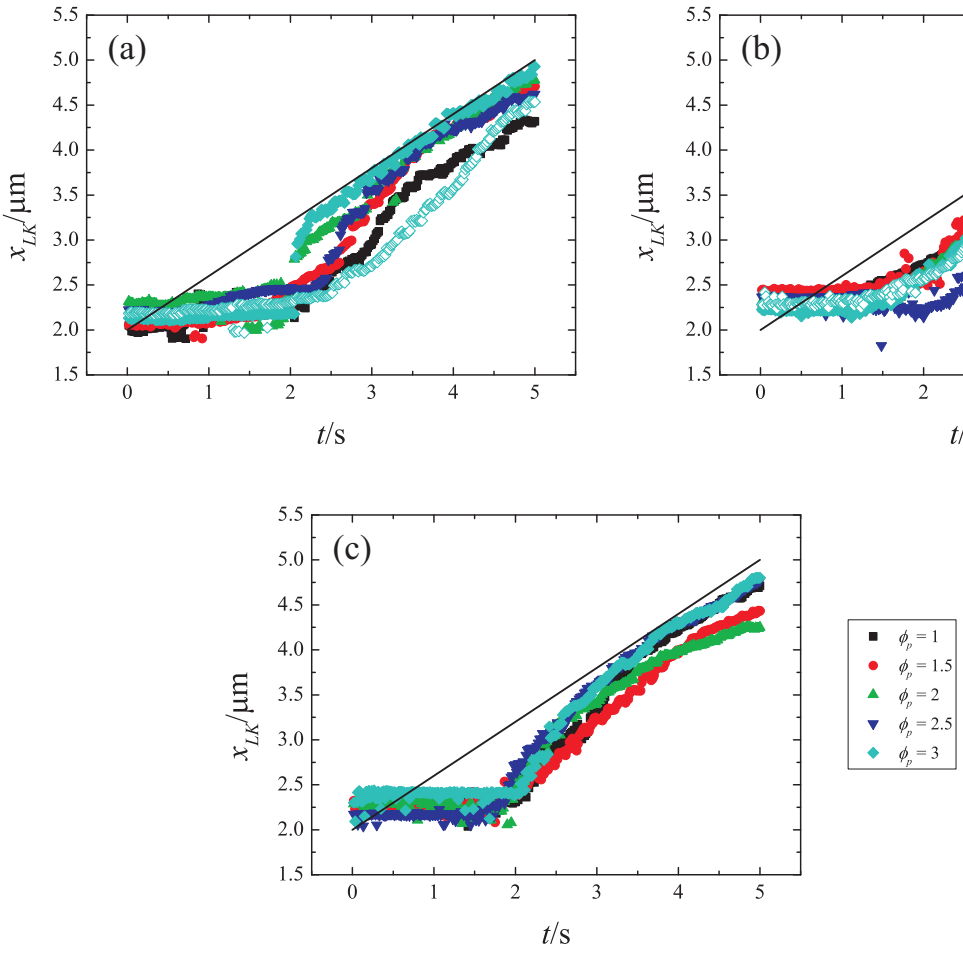

Figure 7.6: Centre-to-centre lock-key separation, x_{LK}, as a function of time, t, for (a) bound dimpled locks, (b) unbound dimpled locks, and (c) spherical locks at various polymer concentrations. The solid black line represents the separation between the moving and stationary traps, x_{trap}. Filled symbols represent data obtained with PEO, and empty symbols denote those measured with xanthan.

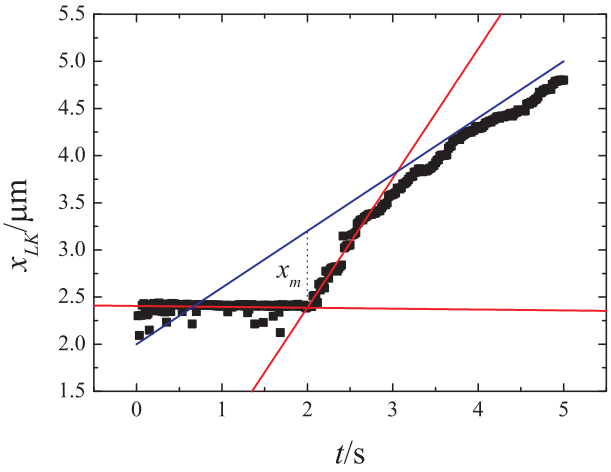

Figure 7.7: An example of locating the breakaway point by finding the sudden change of gradient in a plot of lock-key separation, x_{LK}, against time. The red lines show linear fits to the data either side of the gradient change, and the blue line represents the separation between the moving and stationary traps, x_{trap}.

moving and stationary traps. The point at which the key breaks away from the lock is clearly visible as the sudden change in gradient, and we identify this point more precisely by fitting two straight lines either side of the gradient change - the crossover of these lines thus gives us the breakaway point, as illustrated in figure 7.7. The distance between the key particle and the moving trap at the point of lock-key separation, x_m, is then found, as indicated by the dotted line in figure 7.7. Clearly, the gradient of the line itself also provides us with information about the velocity of the key particle as it is pulled away from the lock. However, due to the presence of polymer, it is not trivial to relate this velocity to a viscous force [169, 170], and as such this analysis is not considered here.

Using the information from figures 7.4, 7.5 and 7.6, plus the expression for the optical force given in eq. (7.3), we are able to calculate the total force opposing that from the depletion interaction, and thus, the force caused by depletion itself. It should be noted that we are unable to say anything explicitly about the depletion potential. Figure 7.8 shows this for dimpled bound locks, dimpled unbound locks, and spherical locks at various polymer concentrations. Although the data are somewhat scattered, and the data fits do not pass through the origin, the trends seen in figure 7.4 are still apparent here in the linear data fits. It is clear from these that the force due to the depletion interaction increases with polymer concentration, as expected due to the known relationship between the depletion attraction and the polymer number density given in chapters 5 and 6. We also find that the depletion force is similar for the two unbound cases

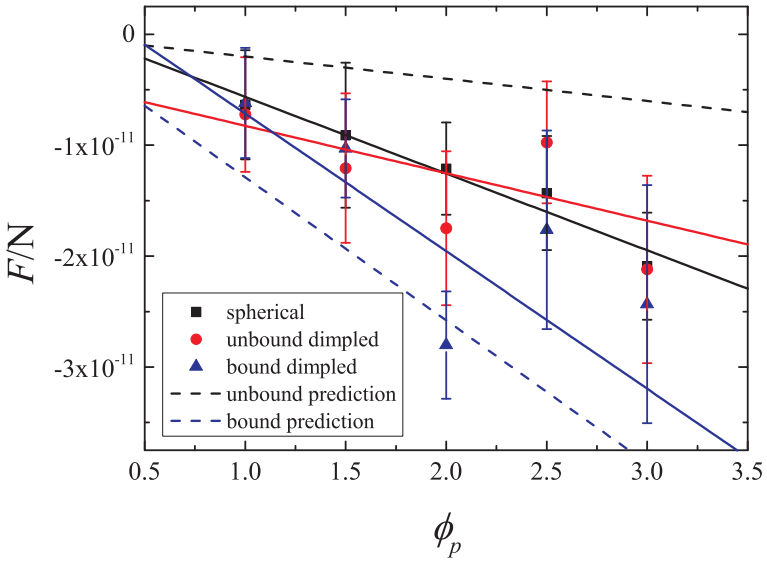

Figure 7.8: Force due to the depletion interaction between lock and key pairs as a function of polymer concentration for the three possible configurations. Error bars are from repeated experiments. Solid lines show linear fits to the data, while dashed lines indicate the forces predicted theoretically.

(i.e. dimpled and spherical locks), and is considerably larger when the lock and key particles are bound together. As explained previously, this is due to the increase in overlap volume provided by the complementary fitting of the key into the lock particle cavity.

Using the models outlined in section 7.2.2, we are able to predict the force due to the depletion attraction for all the systems studied experimentally. These predictions are shown by the dashed lines in figure 7.8, and we find reasonable agreement between theory and experiment. In particular, we see that the gradients of the theoretical prediction lines follow closely those of the linear fits to the experimental data.

Several assumptions are used to produce the theoretical models, and as such some deviation from the measured values is to be expected. Specifically, the depletion interaction between a dimpled bound lock and a key is modelled as having a linear dependence on interparticle separation, as explained in chapter 6. Also, the polymers are treated as ideal, and while the colloid-polymer size ratio is such that this should not have a large effect, some divergence from the theoretical predictions can be ascribed to this [17, 171]. The underlying DLVO potential of the system has been ignored, which could be another source of error. Additionally, in converting the measured current supplied to the laser system to a force, we assume that the potential of each optical trap is parabolic. This has been shown to break down when the particle is positioned far

from the centre of the trap, as is the case in this work, and the potential is considered to have an increased stiffness [161, 163, 172, 173]. We expect further deviations due to both the interference of the two traps with one another, and the scattering of the laser light caused by the particles themselves.

7.5 Conclusions

The force caused by the depletion induced interaction between lock and key particles has been directly measured using optical trapping. Three different configurations have been studied: a dimpled lock with a key particle bound within the cavity, a dimpled lock with an unbound key, and a spherical lock with an unbound key. We have shown that the depletion force acting to hold the particles together is similar for the two unbound cases, and is significantly larger when the lock-key particle shape compatibility is invoked, due to the increase in overlap volume in this state. Additionally, for all configurations, we have demonstrated that the interparticle force becomes stronger as the concentration of polymer increases, and that a smaller polymer results in a stronger depletion interaction. Finally, we have modelled the experimental data with theoretical predictions for the depletion induced force and found reasonable semi-quantitative agreement, despite the use of several assumptions.

This work could be further developed by considering the aforementioned assumptions. For example, following Juniper et al., the optical landscape could be fully mapped to enable a more precise description of the forces due to the traps [163]. A more robust description of the depletion interaction could be considered, by taking into account its non-linear dependence upon particle separation and the non-ideality of the polymers. Finally, terms corresponding to the DLVO potential and friction forces could be included. As well as considering the assumptions, experimental alterations could be made to allow the depletion potential to be probed, as well as the depletion induced force.

Acknowledgements This work was done in collaboration with Arran Curran. Michael Juniper is thanked for helpful discussions.

Summary

In this thesis we investigate the behaviour of uniformly dimpled colloidal particles, and study how they differ from their spherical counterparts. The first chapter provides an overview of the usefulness of colloidal systems, and details how the addition of complexity allows us to create novel particles that lead to interesting applications for a range of topics from fundamental physics to drug delivery. A brief background of the interactions between colloidal particles is presented, and the system used in this work is introduced.

In chapter 2 we provide detailed information regarding the synthesis of both the colloidal particles and the polymers used throughout this thesis. We discuss the methods required to prepare samples suitable for study using static light scattering, laser scanning confocal microscopy and optical tweezing. The benefits of such techniques are given, as well as an overview of their operation, and the image analysis routines used to extract data from the experiments are outlined. Similarly, in chapter 3 we extol the merits of Monte Carlo simulations as a tool for experimentalists and theorists alike, and present the specific algorithm used in this work.

In chapter 4 the marked effect of uniform shape anisotropy on structures formed in the first layer of colloidal particles at a single featureless wall is demonstrated. Using the radial distribution function, the bond-orientational correlation function, and the local bond-orientational order parameter, we show that a single well-defined dimple on an otherwise spherical particle inhibits both the translational and orientational order seen for an equivalent spherical particle. The particles' behaviour is monitored over time, and a decrease in the crystallinity of the system is observed within the first 48 hours of sample preparation. Additionally, a pressure-driven reorientation of the dimpled particles is seen, resulting in the dimples residing in the plane of the image, with no increase in particle number density.

In chapter 5 we introduce non-adsorbing polymer into our system in order to induce a depletion attraction. The dimensionality of the system is reduced to quasi-two, and the behaviour of the colloid-polymer mixture in a monolayer at a flat wall is characterised by the radial distribution function. We investigate the effect of particle shape and concentration, as well as polymer size and concentration, and show that, in the right conditions, particle shape anisotropy can manifest itself in the form of supplementary peak splitting in the radial distribution function, due to complementary overlap of the particles' depletion zones. Basic Monte Carlo simulations are used to corroborate this observation.

Following on from chapter 5, an extra layer of complexity is added to the problem in chapter 6. Small spherical particles are introduced, resulting in a binary colloidal mixture, which allows us to study the depletion induced binding behaviour of so-called "lock and key" colloids. Once more, we probe the effect of lock particle shape and concentration, as well as polymer size and concentration, and quantify our observations by counting the number of bound lock-key pairs, computing the mixed binary radial distribution function, and calculating the equilibrium constant for binding. We show that the inclusion of a lock particle cavity, whose shape and size is complementary to those of the key particle, significantly favours binding behaviour, which is further improved by using a depletant consisting of a small polymer and charge-screening salt.

In chapter 7 the depletion induced force between lock and key particles is directly measured using optical trapping. Contrary to the majority of similar work in the literature, we start with the two particles held in contact by two individual traps, gradually separate the traps, and record the lowest laser power at which the key may be pulled away from the lock. We find that the depletion force is significantly larger when the key is held within the cavity of the lock, due to the larger overlap volume in this configuration. Raising the polymer concentration also results in an increase in the strength of the depletion force. The experimental data is modelled with theoretical predictions, and semi-quantitative agreement is found.

Appendix A

Calculating the volume of the overlap of depletion zones

A.1 Lock-lock overlaps

Here, we provide the details for calculating the volume of the overlap of the depletion zones around dimpled and spherical particles, as used in section 5.2.1. There are three scenarios to consider: i) the dimpled particles in chain formation, ii) the dimpled particles in dimple-down formation, and iii) the spherical particles. As detailed in chapter 3, we describe the dimpled particles as being formed from the overlap of a real sphere with an imaginary sphere. We approximate the particles used in experiment by setting the radius of both spheres to be equal (*rad1*), and work in a dimensionless setup, such that everything is defined in terms of these radii. Quantities that are given in terms of *rad1* are indicated with a *. The distance between the centre of the spheres, $dist^*$, is set to 1.76. We treat the polymer particles as spheres with a radius of $radp^*$, and take care to keep $radp^*$ low enough that the overlaps of the depletion zones never overlap with one another. Finally, we model the depletion zones of the dimpled particles as having sharp edges.

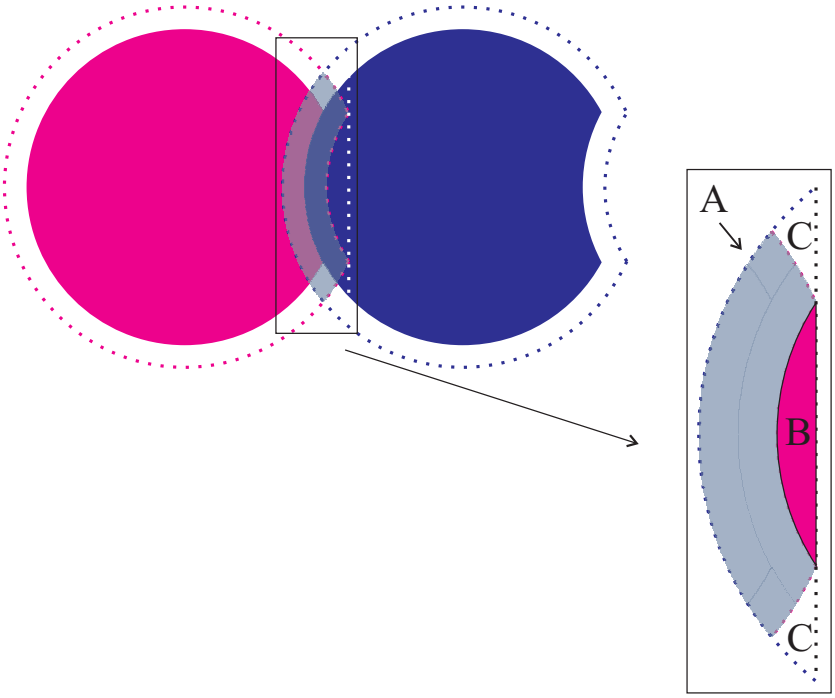

Figure A.1: Overlap of the depletion zones between two dimpled particles in chain formation. The inset gives a zoomed in view of the overlap (shown in grey). This is calculated by finding the volume of the whole spherical cap shown in the inset and subtracting the volume of both the pink spherical cap and the white corners.

A.1.1 Dimpled particles in chain formation

We begin our calculations by firstly focusing on the particle-particle overlap, shown in figure A.1. The overlap of interest is highlighted in grey in figure A.1, and is calculated by considering the three different sections shown in the inset. We initially find the volume of the whole spherical cap (A), and then we must subtract the volume of both the pink spherical cap (B) and the white corners (C). The volume of a spherical cap is given as,

$$V = \frac{\pi}{3}h^2(3R - h), \tag{A.1}$$

with h the height of the cap, and R the radius of the sphere, as indicated in figure A.2. Bearing this in mind, we find that volume A is given by eq. (A.1), with,

$$h = 1 + radp^* - \left(\frac{dist^{*2} - (1 + radp^*)^2 + (1 - radp^*)^2}{2dist^*}\right), \tag{A.2}$$

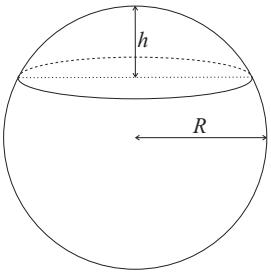

Figure A.2: Definitions used in calculating the volume of a spherical cap.

and $R = 1 + radp^*$. Similarly, volume B is described by a spherical cap with,

$$h = 1 - radp^* - \left(\frac{dist^{*2} - (1 + radp^*)^2 + (1 - radp^*)^2}{2dist^*} \right), \tag{A.3}$$

and $R = 1 - radp^*$. Finding volume C is slightly more challenging, but becomes a lot clearer with the aid of a diagram (figure A.3).

Looking at figure A.3 we find that volume C (indicated by the white corners) is found as

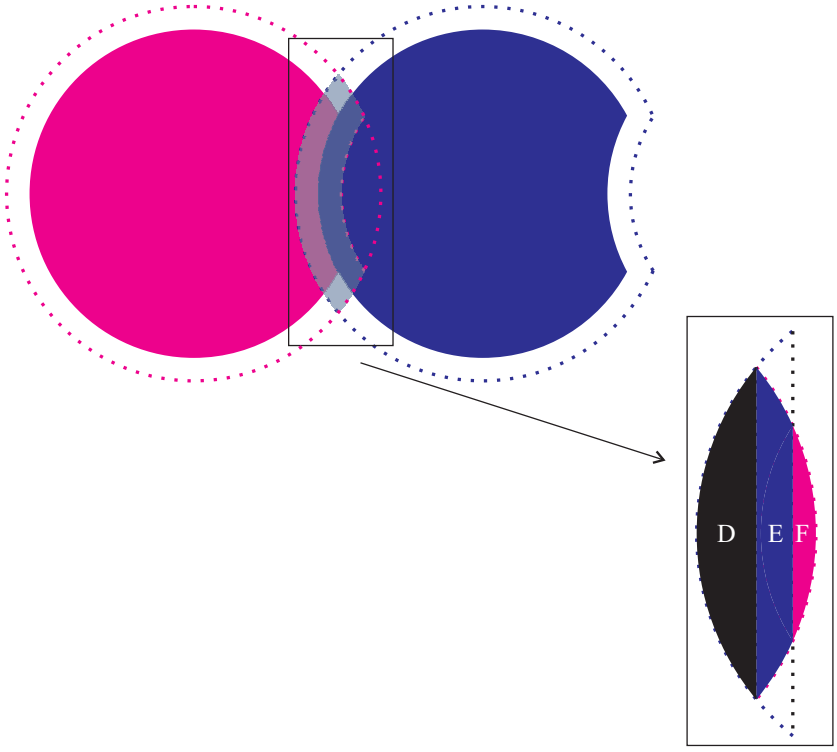

Figure A.3: Overlap of the depletion zones between two dimpled particles in chain formation. The inset gives a zoomed in view of the overlap to aid in the calculation of volume C. This is done by finding the volume of the spherical cap made up of the white sections plus sections D and E, adding the spherical cap F and subtracting the volume of both the spherical cap formed by E and F, as well as that formed by D.

Section	R	h
$C+D+E$	$1+radp^*$	$1+radp^*-\left((dist^{*2}-(1+radp^*)^2+(1-radp^*)^2)/2dist^*\right)$
F	$1+radp^*$	$1+radp^*-\left((dist^{*2}-(1-radp^*)^2+(1+radp^*)^2)/2dist^*\right)$
$E+F$	$1+radp^*$	$1+radp^*-dist^*/2$
D	$1+radp^*$	$1+radp^*-dist^*/2$

Table A.1: Parameters for each volume element in figure A.3.

$C=(C+D+E)+F-(E+F)-D$, where each volume mentioned is itself a spherical cap. The parameters for each volume element are given in table A.1. Now that we know the volume of the overlap of the depletion zones between two particles in chain formation, we must add in the overlap of the depletion zones between the particle and the wall.

As can be seen from figure A.4, the overlap of the depletion zones between the particle and the wall is given as a simple spherical cap for each particle, with $h=2radp^*$ and $R=1+radp^*$.

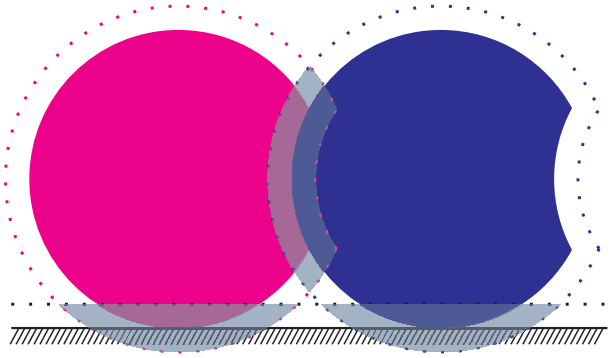

Figure A.4: Overlap of the depletion zones between two dimpled particles in chain formation against a wall.

A.1.2 Dimpled particles in dimple-down formation

As before, we first consider particle-particle overlap, without the presence of a wall. As can be seen from figure A.5, this overlap has the volume of two identical spherical caps, with $h=radp^*$ and $R=1+radp^*$.

We next turn our attention to the particle-wall overlap. In this case, there are two regimes depending on the size of the polymer: if $1-2radp^*-dist^*/2>0$ we are in the small polymer regime, otherwise, we are in the large polymer regime (see figure A.6).

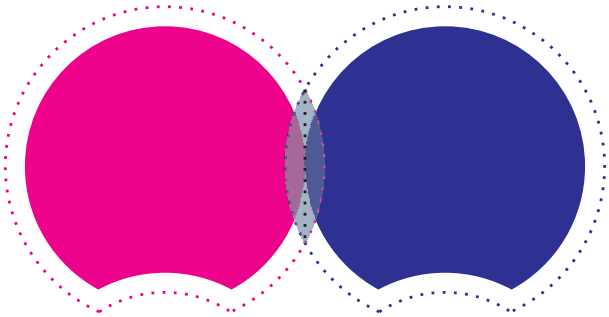

Figure A.5: Overlap of the depletion zones between two dimpled particles in dimple-down formation.

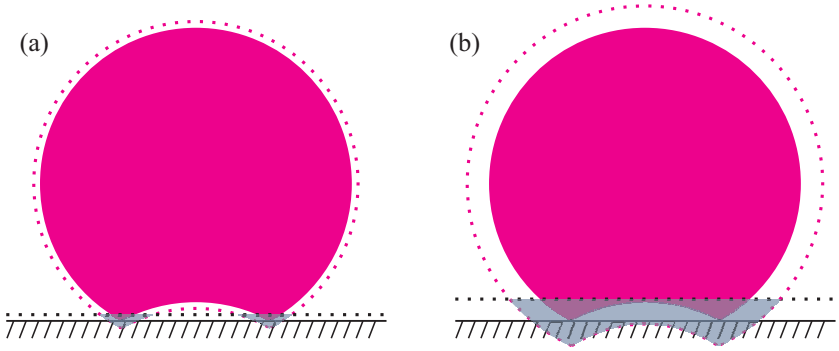

Figure A.6: Two regimes for the particle-wall overlap when in the dimple-down configuration.

Small polymer regime

From figure A.7 we can see that the volume of the overlap of the depletion zones, V_1, (shown in grey) is given as $V_1 = (V_1 + H + I) + G - I - (G + H)$, where again, each volume is described by a spherical cap. The parameters for each volume section are given in table A.2.

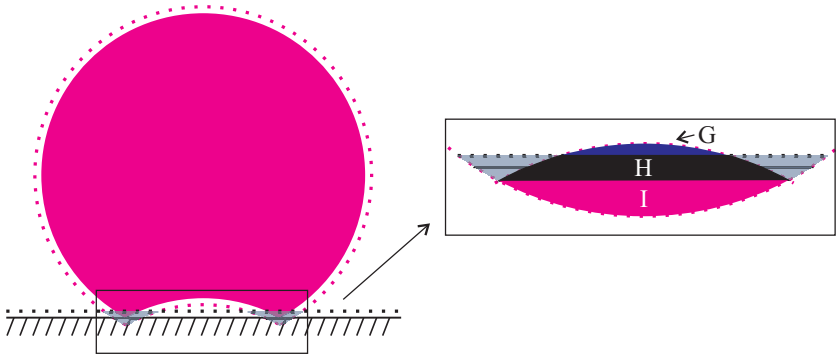

Figure A.7: Overlap of the depletion zones between a dimple-down particle and a wall in the small polymer regime. The volume of interest (shown in grey) is given by finding the spherical cap formed by the grey sections along with H and I, adding G, and then subtracting I and the spherical cap formed by G and H.

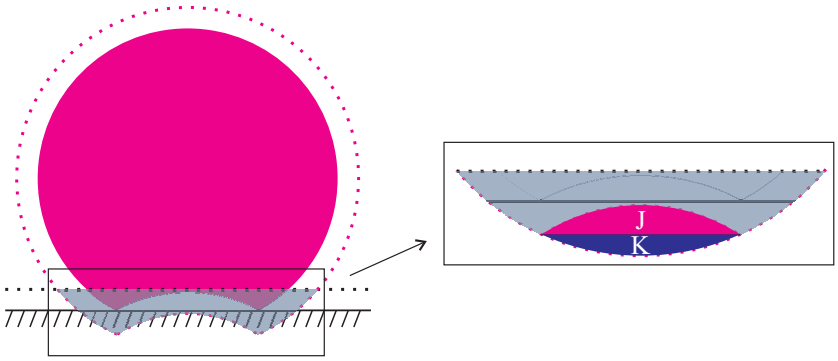

Figure A.8: Overlap of the depletion zones between a dimple-down particle and a wall in the large polymer regime. The volume of interest (shown in grey) is given by finding the spherical cap formed by the grey sections along with J and K, and then subtracting J and K individually.

Large polymer regime

Figure A.8 shows the method to calculate the volume of the particle-wall overlap of the depletion zones, V_2, (shown in grey) in the large polymer regime of dimple-down formation. This is given as $V_2 = (V_2 + J + K) - J - K$, where once more, each volume is described by a spherical cap. The parameters for each volume section are given in table A.2.

Section	R	h
$V_1 + H + I$	$1 + radp^*$	$1 + 2radp^* - dist^*/2$
G	$1 - radp^*$	$1 - 2radp^* - dist^*/2$
$G + H$	$1 - radp^*$	$1 - radp^* - \left((dist^{*2} - (1 + radp^*)^2 + (1 - radp^*)^2)/2dist^*\right)$
I	$1 + radp^*$	$1 + radp^* - \left((dist^{*2} - (1 - radp^*)^2 + (1 + radp^*)^2)/2dist^*\right)$
$V_2 + J + K$	$1 + radp^*$	$1 + 2radp^* - dist^*/2$
J	$1 - radp^*$	$1 - radp^* - \left((dist^{*2} - (1 + radp^*)^2 + (1 - radp^*)^2)/2dist^*\right)$
K	$1 + radp^*$	$1 + radp^* - \left((dist^{*2} - (1 - radp^*)^2 + (1 + radp^*)^2)/2dist^*\right)$

Table A.2: Parameters for each volume element in figures A.7 and A.8.

A.1.3 Spherical particles

Finally, we describe the methods for calculating the volume of the overlap of the depletion zones for the spherical particles against a wall. As we can see from figure A.9(a), the particle-particle overlap is given simply by two identical spherical caps with $h = radp^*$ and $R = 1 + radp^*$. Similarly, from figure A.9(b), we find that the particle-wall overlap is described by another spherical cap, this time with $h = 2radp^*$ and $R = 1 + radp^*$.

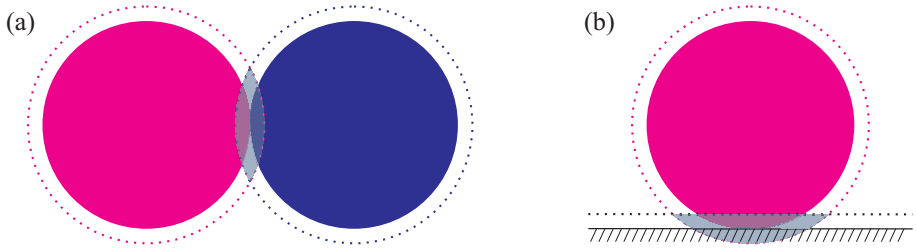

Figure A.9: Overlap of the depletion zones for the spherical particles. (a) shows the particle-particle overlap, while (b) illustrates the particle-wall overlap. Both are given by simple spherical caps.

A.2 Lock-key overlaps

We now outline the procedure for calculating the overlap volume between a dimpled lock particle and a spherical key particle at contact, as used in section 6.2. The protocols outlined at the beginning of section A.1 are still followed, but we additionally introduce a key particle whose radius, $radk^*$, is set to be 0.67, in line with the particles used in experiment. We further assume that both particles are aligned in the x direction to maximise overlap, leading to a centre-to-centre separation, sep^*, of 1.43. From figure A.10 we see that the total overlap volume is given as $A + B - C - D$, where each section is a spherical cap, the parameters for which are given in table A.3.

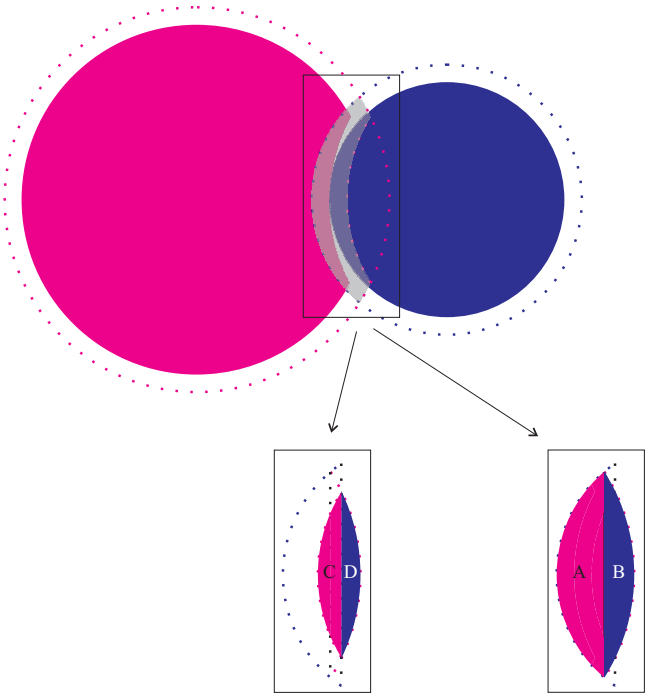

Figure A.10: Overlap of the depletion zones for a lock with a key.

Section	R	h
A	$radk^* + radp^*$	$radk^* + radp^* - \left((sep^{*2} - (1 + radp^*)^2 + (radk^* + radp^*)^2)/2sep^*\right)$
B	$1 + radp^*$	$1 + radp^* - \left((sep^{*2} - (radk^* + radp^*)^2 + (1 + radp^*)^2)/2sep^*\right)$
C	$1 - radp^*$	$1 - radp^* - sep^*/2$
D	$1 + radp^*$	$1 + radp^* - sep^*/2$

Table A.3: Parameters for each volume element in figure A.10.

Bibliography

[1] W. Poon. Colloids as big atoms. *Science (New York, N.Y.)*, 304(5672):830–1, May 2004.

[2] R. J. Hunter. *Foundations of Colloid Science*. Oxford University Press, 2nd edition, 2001.

[3] W. B. Russel, D. A. Saville, and W. R. Schowalter. *Colloidal Dispersions*. Cambridge University Press, 1989.

[4] A. D. McNaught and A. Wilkinson. *IUPAC Compendium of Chemical Terminology (the "Gold Book").* Blackwell Scientific Publications, Oxford, 2nd edition, 1997.

[5] R. Brown. On the existence of active molecules. *Philosophical Magazine*, (21), 1828.

[6] M. D. Haw. Colloidal suspensions, Brownian motion, molecular reality: a short history. *Journal of physics: condensed matter*, 7769, 2002.

[7] A. Einstein. Über die von der molekularkinetischen Theorie der Wärme geforderte Bewegung von in ruhenden Flüssigkeiten suspendierten Teilchen. *Annalen der physik*, 1905.

[8] R. Furth. *Investigations on the Theory of the Brownian Movement by Albert Einstein*. Dover, 1956.

[9] M. von Smoluchowski. Zur kinetischen theorie der brownschen molekularbewegung und der suspensionen. *Annalen der physik*, 1906.

[10] D. S. Lemons and A. Gythiel. Paul Langevin's 1908 paper On the Theory of Brownian Motion. *American Journal of Physics*, 533(1908):1079–1081, 1997.

[11] J. Perrin. Mouvement Brownien et Réalité Moléculaire. *Annales de Chimie et de Physique*, 18:5–114, 1909.

[12] T. O. E. Skinner. *Two-dimensional colloidal systems: grain boundaries and confinement*. Dphil, University of Oxford, 2012.

[13] C. A. Murray and D. G. Grier. Video Microscopy of Monodisperse Colloidal Systems. *Annual Review of Physical Chemistry*, 47(1):421–462, October 1996.

[14] P. Habdas and E. R. Weeks. Video microscopy of colloidal suspensions and colloidal crystals. *Current Opinion in Colloid & Interface Science*, 7(3-4):196–203, August 2002.

[15] D. G. A. L. Aarts, M. Schmidt, and H. N. W. Lekkerkerker. Direct visual observation of thermal capillary waves. *Science (New York, N.Y.)*, 304(5672):847–50, May 2004.

[16] D. G. A. L. Aarts, H. N. W. Lekkerkerker, H. Guo, G. H. Wegdam, and D. Bonn. Hydrodynamics of Droplet Coalescence. *Physical Review Letters*, 95(16):164503, October 2005.

[17] D. Aarts. *The interface in demixed colloid-polymer systems: wetting, waves and droplets.* Phd, Universiteit Utrecht, 2005.

[18] A. van Blaaderen. Colloidal molecules and beyond. *Science (New York, N.Y.)*, 301(5632):470–1, July 2003.

[19] A. van Blaaderen. Colloids get complex. *Nature*, 439:545–546, 2006.

[20] D. J. Kraft, J. Groenewold, and W. K. Kegel. Colloidal molecules with well-controlled bond angles. *Soft Matter*, 5(20):3823, 2009.

[21] J.-G. Park, J. D. Forster, and E. R. Dufresne. Synthesis of colloidal particles with the symmetry of water molecules. *Langmuir : the ACS journal of surfaces and colloids*, 25(16):8903–6, August 2009.

[22] S. C. Glotzer. Materials science. Some Assembly Required. *Science (New York, N.Y.)*, 306(5695):419–20, October 2004.

[23] S. C. Glotzer and M. J. Solomon. Anisotropy of building blocks and their assembly into complex structures. *Nature materials*, 6(8):557–62, August 2007.

[24] J. Du and R. K. O'Reilly. Anisotropic particles with patchy, multicompartment and Janus architectures: preparation and application. *Chemical Society Reviews*, 40(5):2402, 2011.

[25] K. J. Lee, J. Yoon, and J. Lahann. Recent advances with anisotropic particles. *Current Opinion in Colloid & Interface Science*, 16(3):195–202, June 2011.

[26] S. Sacanna and D. J. Pine. Shape-anisotropic colloids: Building blocks for complex assemblies. *Current Opinion in Colloid & Interface Science*, 16(2):96–105, April 2011.

[27] E. Duguet, A. Désert, A. Perro, and S. Ravaine. Design and elaboration of colloidal molecules: an overview. *Chemical Society reviews*, 40(2):941–60, February 2011.

[28] S. Sacanna, D. J. Pine, and G.-R. Yi. Engineering shape: the novel geometries of colloidal self-assembly. *Soft Matter*, pages 8096–8106, 2013.

[29] S.-M. Yang, S.-H. Kim, J.-M. Lim, and G.-R. Yi. Synthesis and assembly of structured colloidal particles. *Journal of Materials Chemistry*, 18(19):2177, 2008.

[30] M. Marechal. *Anisotropic colloids : bulk phase behavior and equilibrium sedimentation.* Phd, Universiteit Utrecht, 2009.

[31] Z. Mao, H. Xu, and D. Wang. Molecular Mimetic Self-Assembly of Colloidal Particles. *Advanced Functional Materials*, 20(7):1053–1074, March 2010.

[32] Z.-Y. Li, J. Wang, and B.-Y. Gu. Full Band Gap in Fcc and Bcc Photonic Band Gaps Structure: NonSpherical Atom. *Journal of the Physical Society of Japan*, 1998.

[33] Y. Xia, B. Gates, and Z.-Y. Li. Self-Assembly Approaches to Three-Dimensional Photonic Crystals. *Advanced Materials*, 13(6):409–413, March 2001.

[34] Y. Zhang, J. Wang, Y. Huang, Y. Song, and L. Jiang. Fabrication of functional colloidal photonic crystals based on well-designed latex particles. *Journal of Materials Chemistry*, 21(37):14113, 2011.

[35] L. Rossi, S. Sacanna, W. T. M. Irvine, P. M. Chaikin, D. J. Pine, and A. P. Philipse. Cubic crystals from cubic colloids. *Soft Matter*, 7(9):4139, 2011.

[36] S. H. Lee, S. J. Gerbode, B. S. John, A. K. Wolfgang, F. A. Escobedo, I. Cohen, and C. M. Liddell. Synthesis and assembly of nonspherical hollow silica colloids under confinement. *Journal of Materials Chemistry*, 18(41):4912, 2008.

[37] A. Perro, S. Reculusa, E. Bourgeat-Lami, E. Duguet, and S. Ravaine. Synthesis of hybrid colloidal particles: From snowman-like to raspberry-like morphologies. *Colloids and Surfaces A: Physicochemical and Engineering Aspects*, 284-285:78–83, August 2006.

[38] S. Lone and I. W. Cheong. Fabrication of polymeric Janus particles by droplet microfluidics. *RSC Advances*, 4(26):13322, 2014.

[39] C. Kaewsaneha, P. Tangboriboonrat, D. Polpanich, M. Eissa, and A. Elaissari. Preparation of Janus colloidal particles via Pickering emulsion: An overview. *Colloids and Surfaces A: Physicochemical and Engineering Aspects*, 439:35–42, December 2013.

[40] A. Walther and A. H. E. Müller. Janus particles. *Soft Matter*, 4(4):663, 2008.

[41] A. B. Pawar and I. Kretzschmar. Fabrication, assembly, and application of patchy particles. *Macromolecular rapid communications*, 31(2):150–68, January 2010.

[42] H. Hou, D. Yu, Q. Tian, and G. Hu. Preparation, characterization, and properties of hollow Janus particles with tailored shapes. *Langmuir : the ACS journal of surfaces and colloids*, 30(7):1741–7, February 2014.

[43] L. Xu, H. Li, X. Jiang, J. Wang, L. Li, Y. Song, and L. Jiang. Synthesis of Amphiphilic Mushroom Cap-shaped Colloidal Particles towards Fabrication of Anisotropic Colloidal Crystals. *Macromolecular rapid communications*, 31(16):1422–6, August 2010.

[44] B. V. Derjaguin and L. Landau. Theory of the stability of strongly charged lyophobic sols and of the adhesion of strongly charged particles in solution of electrolytes. *Acta Physicochimica USSR*, 14:633, 1941.

[45] E. J. W. Verwey and J. Th. G. Overbeek. *Theory of the stability of lyophobic colloids*. Elsevier, 1948.

[46] H. N. W. Lekkerkerker and R. Tuinier. *Colloids and the depletion interaction*, volume 833. Springer, 2011.

[47] F. Oosawa and S. Asakura. On Interaction between Two Bodies Immersed in a Solution of Macromolecules. *The Journal of Chemical Physics*, 22(7):1255, 1954.

[48] F. Oosawa and S. Asakura. Interaction between Particles Suspended in Solutions. *Journal of Polymer Science*, XXXIII:183–192, 1958.

[49] A. Vrij. Polymers at interfaces and the interactions in colloidal dispersions. *Pure and Applied Chemistry*, 48:471–483, 1976.

[50] S. Sacanna, W. T. M. Irvine, P. M. Chaikin, and D. J. Pine. Lock and key colloids. *Nature*, 464(7288):575–8, March 2010.

[51] S. Sacanna, W. T. M. Irvine, L. Rossi, and D. J. Pine. Lock and key colloids through polymerization-induced buckling of monodisperse silicon oil droplets. *Soft Matter*, 7(5):1631, 2011.

[52] G. Bosma, C. Pathmamanoharan, E. H. A. de Hoog, W. K. Kegel, A. van Blaaderen, and H. N. W. Lekkerkerker. Preparation of Monodisperse , Fluorescent PMMA Latex Colloids by Dispersion Polymerization. *Journal of Colloid and Interface Science*, 300:292–300, 2002.

[53] G. H. Koenderink, D. G. A. L. Aarts, V. W. A. de Villeneuve, A. P. Philipse, R. Tuinier, and H. N. W. Lekkerkerker. Morphology and kinetics of phase separating transparent xanthan-colloid mixtures. *Biomacromolecules*, 4(1):129–136, 2003.

[54] E. Jamie. *Colloidal interfaces in confinement*. Dphil, University of Oxford, 2011.

[55] H. Benoit and P. Doty. Light scattering from non-Gaussian chains. *The Journal of Physical Chemistry*, 57(6):958–963, 1953.

[56] T. Coviello, K. Kajiwara, and V. Crescenzi. Solution Properties of Xanthan. 1. Dynamic and Static Light Scattering. *Macromolecules*, 19(11):2826–2831, 1986.

[57] B. Z. Shang, Z. Wang, and R. G. Larson. Molecular dynamics simulation of interactions between a sodium dodecyl sulfate micelle and a poly(ethylene oxide) polymer. *The journal of physical chemistry. B*, 112(10):2888–900, March 2008.

[58] M. Minsky. Memoir on Inventing the Confocal Scanning Microscope. *Scanning*, 10:128–138, 1988.

[59] R. H. Webb. Confocal optical microscopy. *Reports on Progress in Physics*, 427(59):427–471, 1996.

[60] R. Dullens. *Structure and dynamics of colloidal hard spheres in real-space*. Phd, Universiteit Utrecht, 2005.

[61] E. Hecht. *Optics*. Addison Wesley, fourth edition, 2002.

[62] S. Egelhaaf. Solution Scattering. In *Soft Condensed Matter Physics in Molecular and Cell Biology*. Taylor and Francis, 2006.

[63] A. J. Howe. *Synthesis of colloidal model systems for optical tweezing*. Part ii, University of Oxford, 2012.

[64] G. Mie. Der physik. 1. *Leipzig, Ann. Phys.*, 330:377–445, 1908.

[65] C. Bohren and D. Huffman. *Absorption and scattering of light by small particles*. Wiley, 1983.

[66] A. Ashkin. Acceleration and Trapping of Particles by Radiation Pressure. *Physical Review Letters*, 24(4):156–159, January 1970.

[67] A. Ashkin and J. M. Dziedzic. Optical Levitation by Radiation Pressure. *Applied Physics Letters*, 19(8):283, 1971.

[68] A. Ashkin, J. M. Dziedzic, J. E. Bjorkholm, and S. Chu. Observation of a single-beam gradient-force optical trap for dielectric particles. *Optics letters*, 11(5):288–290, June 1986.

[69] J. E. Molloy and M. J. Padgett. Lights, action: Optical tweezers. *Contemporary Physics*, 43(4):241–258, July 2002.

[70] D. G. Grier. A revolution in optical manipulation. *Nature*, 424(6950):810–6, August 2003.

[71] K. Svoboda and S. M. Block. Biological applications of optical forces. *Annual review of biophysics and biomolecular structure*, 23:247–85, January 1994.

[72] H. Zhang and K.-K. Liu. Optical tweezers for single cells. *Journal of the Royal Society, Interface / the Royal Society*, 5(24):671–90, July 2008.

[73] D. G. Grier. Optical tweezers in colloid and interface science. *Current Opinion in Colloid & Interface Science*, 2(3):264–270, June 1997.

[74] http://www.stanford.edu/group/blocklab/Optical%20Tweezers%20Introduction.htm.

[75] P. A. M. Neto and H. M. Nussenzveig. Theory of optical tweezers. *EPL (Europhysics Letters)*, 702, 2000.

[76] A. Mazolli, P. A. Maia Neto, and H. M. Nussenzveig. Theory of trapping forces in optical tweezers. *Proceedings of the Royal Society of London, series A: Mathematical, Physical and Engineering Sciences*, 459(2040):3021–3041, 2003.

[77] A. Ashkin. Forces of a single-beam gradient laser trap on a dielectric sphere in the ray optics regime. *Biophysical Journal*, 61(2):569–582, February 1992.

[78] Y. Liu. *Dynamics of dimpled colloids near a surface*. Part ii, University of Oxford, 2013.

[79] A. Curran, A. M. Yao, G. M. Gibson, R. Bowman, J. M. Cooper, and M. L. Padgett. Real time characterization of hydrodynamics in optically trapped networks of micro-particles. *Journal of biophotonics*, 3(4):244–51, April 2010.

[80] J. Leach, K. Wulff, G. Sinclair, P. Jordan, J. Courtial, L. Thomson, G. Gibson, K. Karunwi, J. Cooper, Z. J. Laczik, and M. Padgett. Interactive approach to optical tweezers control. *Applied optics*, 45(5):897–903, February 2006.

[81] J. Liesener, M. Reicherter, T. Haist, and H. J. Tiziani. Multi-functional optical tweezers using computer-generated holograms. *Optics Communications*, 185(November):77–82, 2000.

[82] J. Crocker and D. Grier. Methods of Digital Video Microscopy for Colloidal Studies. *Journal of Colloid and Interface Science*, 310(179):298–310, 1996.

[83] J. McLoone. http://blog.wolfram.com/2011/09/09/building-a-microscopy-application-in-mathematica/, 2011.

[84] N. Metropolis. The beginning. *Los Alamos Science*, pages 125–130, 1987.

[85] N. Metropolis and S. Ulam. The Monte Carlo method. *Journal of the American statistical association*, 44(247):335–341, 1949.

[86] N. Metropolis, A. W. Rosenbluth, M. N. Rosenbluth, A. H. Teller, and E. Teller. Equation of State Calculations by Fast Computing Machines. *The Journal of Chemical Physics*, 21(6):1087, 1953.

[87] D. Frenkel and B. Smit. *Understanding molecular simulation: from algorithms to applications*. Elsevier, 2nd edition, 2002.

[88] W. W. Wood and J. D. Jacobson. Preliminary Results from a Recalculation of the Monte Carlo Equation of State of Hard Spheres. *The Journal of Chemical Physics*, 27(5):1207, 1957.

[89] W. G. Hoover. Melting Transition and Communal Entropy for Hard Spheres. *The Journal of Chemical Physics*, 49(8):3609, 1968.

[90] M. Marechal and M. Dijkstra. Colloidal hard dumbbells under gravity: structure and crystallization. *Soft Matter*, 7(4):1397, 2011.

[91] M. Dijkstra. Capillary Freezing or Complete Wetting of Hard Spheres in a Planar Hard Slit? *Physical Review Letters*, 93(10):108303, September 2004.

[92] M. Marechal and M. Dijkstra. Crystallization of colloidal hard spheres under gravity. *Physical Review E*, 75(6):061404, June 2007.

[93] Y. Norizoe and T. Kawakatsu. Particle Monte Carlo simulation of string-like colloidal assembly in two and three dimensions. *The Journal of chemical physics*, 137(2):024904, July 2012.

[94] M. Marechal, R. J. Kortschot, A. F. Demirörs, A. Imhof, and M. Dijkstra. Phase behavior and structure of a new colloidal model system of bowl-shaped particles. *Nano letters*, 10(5):1907–11, May 2010.

[95] M. Marechal and M. Dijkstra. Phase behavior and structure of colloidal bowl-shaped particles: Simulations. *Physical Review E*, 82(3):1–11, September 2010.

[96] M. He and P. Siders. Monte Carlo calculation of orientationally anisotropic pair distributions and energy transfer in a model monolayer. *The Journal of Physical Chemistry*, 94(18):7280–7288, September 1990.

[97] R. Eppenga and D. Frenkel. Monte Carlo study of the isotropic and nematic phases of infinitely thin hard platelets. *Molecular Physics*, 52(6):1303–1334, August 1984.

[98] M. Dennison, K. Milinković, and M. Dijkstra. Phase diagram of hard snowman-shaped particles. *The Journal of chemical physics*, 137(4):044507, July 2012.

[99] K. Milinković, M. Dennison, and M. Dijkstra. Phase diagram of hard asymmetric dumbbell particles. *Physical Review E*, 87(3):032128, March 2013.

[100] D. J. Ashton, R. L. Jack, and N. B. Wilding. Self-assembly of colloidal polymers via depletion-mediated lock and key binding. *Soft Matter*, pages 9661–9666, 2013.

[101] M. Marechal. Private communication, 2011.

[102] K. Zhao and T. Mason. Frustrated Rotator Crystals and Glasses of Brownian Pentagons. *Physical Review Letters*, 103(20):208302, November 2009.

[103] R. C. Kramb and C. F. Zukoski. Nonlinear rheology and yielding in dense suspensions of hard anisotropic colloids. *Journal of Rheology*, 55(5):1069, 2011.

[104] C. I. Zoldesi, C. A. van Walree, and A. Imhof. Deformable hollow hybrid silica/siloxane colloids by emulsion templating. *Langmuir : the ACS journal of surfaces and colloids*, 22(9):4343–52, April 2006.

[105] H. R. Sheu, M. S. El-Aasser, and J. W. Vanderhoff. Uniform nonspherical latex particles as model interpenetrating polymer networks. *Journal of Polymer Science Part A: Polymer Chemistry*, 28(3):653–667, February 1990.

[106] J. P. Hoogenboom, P. Vergeer, and A. van Blaaderen. A real-space analysis of colloidal crystallization in a gravitational field at a flat bottom wall. *The Journal of Chemical Physics*, 119(6):3371, 2003.

[107] J. P. Hoogenboom, D. Derks, P. Vergeer, and A. van Blaaderen. Stacking faults in colloidal crystals grown by sedimentation. *The Journal of Chemical Physics*, 117(24):11320, 2002.

[108] A. van Blaaderen, J. P. Hoogenboom, D. L. J. Vossen, A. Yethiraj, A. van der Horst, K. Visscher, and M. Dogterom. Colloidal epitaxy: Playing with the boundary conditions of colloidal crystallization. *Faraday Discussions*, 123:107–119, January 2003.

[109] J. Hoogenboom, A. van Langen-Suurling, J. Romijn, and A. van Blaaderen. Epitaxial growth of a colloidal hard-sphere hcp crystal and the effects of epitaxial mismatch on crystal structure. *Physical Review E*, 69(5):051602, May 2004.

[110] R. Ganapathy, M. R. Buckley, S. J. Gerbode, and I. Cohen. Direct measurements of island growth and step-edge barriers in colloidal epitaxy. *Science (New York, N.Y.)*, 327(5964):445–8, January 2010.

[111] R. Dullens, M. Mourad, D. Aarts, J. Hoogenboom, and W. Kegel. Shape-Induced Frustration of Hexagonal Order in Polyhedral Colloids. *Physical Review Letters*, 96(2):028304, January 2006.

[112] E. K. Riley and C. M. Liddell. Confinement-controlled self assembly of colloids with simultaneous isotropic and anisotropic cross-section. *Langmuir : the ACS journal of surfaces and colloids*, 26(14):11648–56, July 2010.

[113] I. D. Hosein and C. M. Liddell. Convectively assembled nonspherical mushroom cap-based colloidal crystals. *Langmuir : the ACS journal of surfaces and colloids*, 23(17):8810–4, August 2007.

[114] J.-P. Hansen and I. R. McDonald. *Theory of Simple Liquids*. Academic Press, 2006.

[115] D. R. Nelson. *Defects and Geometry in Condensed Matter Physics*. Cambridge University Press, 2002.

[116] C. A. Murray. Bond-Orientational Order in Condensed Matter Systems. In K. Strandburg, editor, *Bond-Orientational Order in Condensed Matter Systems*, pages 137–215. Springer-Verlag, 1992.

[117] M. M. van Schooneveld, V. W. A. de Villeneuve, R. P. A. Dullens, D. G. A. L. Aarts, M. E. Leunissen, and W. K. Kegel. Structure, stability, and formation pathways of colloidal gels in systems with short-range attraction and long-range repulsion. *The Journal of Physical Chemistry B*, 113(14):4560–4, April 2009.

[118] R. Sanchez and P. Bartlett. Equilibrium cluster formation and gelation. *Journal of Physics: Condensed Matter*, 17(45):S3551–S3556, November 2005.

[119] G. Koenderink, S. Sacanna, D. Aarts, and A. Philipse. Rotational and translational diffusion of fluorocarbon tracer spheres in semidilute xanthan solutions. *Physical Review E*, 69(2):021804, February 2004.

[120] X. Ye, T. Narayanan, P. Tong, J. S. Huang, M. Y. Lin, B. L. Carvalho, and L. J. Fetters. Depletion interactions in colloid-polymer mixtures. *Physical Review. E, Statistical physics, plasmas, fluids, and related interdisciplinary topics*, 54(6):6500–6510, December 1996.

[121] G. M. H. Wilkins, P. T. Spicer, and M. J. Solomon. Colloidal system to explore structural and dynamical transitions in rod networks, gels, and glasses. *Langmuir : the ACS journal of surfaces and colloids*, 25(16):8951–9, August 2009.

[122] K. Zhao and T. Mason. Directing Colloidal Self-Assembly through Roughness-Controlled Depletion Attractions. *Physical Review Letters*, 99(26):268301, December 2007.

[123] R. Rice, R. Roth, and C. P. Royall. Polyhedral colloidal rocks: low-dimensional networks. *Soft Matter*, 8(4):1163, 2012.

[124] A. D. Dinsmore, A. G. Yodh, and D. J. Pine. Phase diagrams of nearly-hard-sphere binary colloids. *Physical Review E*, 52(4), 1995.

[125] P. D. Kaplan, J. L. Rouke, A. G. Yodh, and D. J. Pine. Entropically driven surface phase separation in binary colloidal mixtures. *Physical Review Letters*, 72(4):582–585, January 1994.

[126] A. D. Dinsmore, A. G. Yodh, and D. J. Pine. Entropic control of particle motion using passive surface mircostructures. *Nature*, 383, 1996.

[127] I. Langmuir. Repulsive forces between charged surfaces in water, and the cause of the Jones-Ray effect. *Science*, 88(2288):430–432, 1938.

[128] J. Israelachvili. *Intermolecular and Surface Forces*. Academic Press, 1995.

[129] H. N. W. Lekkerkerker, W. C. K. Poon, P. N. Pusey, A. Stroobants, and P. B. Warren. Phase behaviour of colloid + polymer mixtures. *Europhysics Letters*, 20(6):559, 1992.

[130] D. J. Ashton. Private communication, 2013.

[131] C. Kaewsaneha, P. Tangboriboonrat, D. Polpanich, M. Eissa, and A. Elaissari. Janus colloidal particles: preparation, properties, and biomedical applications. *ACS applied materials & interfaces*, 5(6):1857–69, March 2013.

[132] E. Y. K. Fung, K. Muangnapoh, and C. M. Liddell Watson. Anisotropic photonic crystal building blocks: colloids tuned from mushroom-caps to dimers. *Journal of Materials Chemistry*, 22(21):10507, 2012.

[133] S. H. Lee, E. Y. Fung, E. K. Riley, and C. M. Liddell. Asymmetric colloidal dimers under quasi-two-dimensional confinement. *Langmuir : the ACS journal of surfaces and colloids*, 25(13):7193–5, July 2009.

[134] S.-H. Kim, A. D. Hollingsworth, S. Sacanna, S.-J. Chang, G. Lee, D. J. Pine, and G.-R. Yi. Synthesis and assembly of colloidal particles with sticky dimples. *Journal of the American Chemical Society*, 134(39):16115–8, October 2012.

[135] D. J. Kraft, R. Ni, F. Smallenburg, M. Hermes, K. Yoon, D. A. Weitz, A. van Blaaderen, J. Groenewold, M. Dijkstra, and W. K. Kegel. Surface roughness directed self-assembly of

patchy particles into colloidal micelles. *Proceedings of the National Academy of Sciences of the United States of America*, 109(27):10787–92, July 2012.

[136] E. Fischer. Einfluss der Configuration auf die Wirkung der Enzyme. *Berichte der deutschen chemischen Gesellschaft*, 1894.

[137] M. Ceriotti. Private communication, 2013.

[138] D. Kleshchanok, R. Tuinier, and P. R. Lang. Direct measurements of polymer-induced forces. *Journal of Physics: Condensed Matter*, 20(7):073101, February 2008.

[139] W. H. Briscoe and R. G. Horn. Direct measurement of surface forces due to charging of solids immersed in a nonpolar liquid. *Langmuir*, 10(15):3945–3956, 2002.

[140] C. E. McNamee, Y. Tsujii, and M. Matsumoto. Interaction forces between two silica surfaces in an apolar solvent containing an anionic surfactant. *Langmuir*, (16):1791–1798, 2004.

[141] W. A. Ducker, T. J. Senden, and R. M. Pashley. Direct measurement of colloidal forces using an atomic force microscope. *nature*, 1991.

[142] S. H. Behrens, J. Plewa, and D. G. Grier. Measuring a colloidal particle's interaction with a flat surface under nonequilibrium conditions. Total internal reflection microscopy with absolute position information. *The European physical journal. E, Soft matter*, 10(2):115–21, February 2003.

[143] D. Prieve. Measurement of colloidal forces with TIRM. *Advances in Colloid and Interface Science*, 82(1-3):93–125, October 1999.

[144] K. Kegler, M. Salomo, and F. Kremer. Forces of Interaction between DNA-Grafted Colloids: An Optical Tweezer Measurement. *Physical Review Letters*, 98(5):058304, February 2007.

[145] M. M. Elmahdy, A. Synytska, A. Drechsler, C. Gutsche, P. Uhlmann, M. Stamm, and F. Kremer. Forces of Interaction between Poly(2-vinylpyridine) Brushes As Measured by Optical Tweezers. *Macromolecules*, 42(22):9096–9102, November 2009.

[146] D. El Masri, P. van Oostrum, F. Smallenburg, T. Vissers, A. Imhof, M. Dijkstra, and A. van Blaaderen. Measuring colloidal forces from particle position deviations inside an optical trap. *Soft Matter*, 7(7):3462, 2011.

[147] C. Gutsche, U. Keyser, K. Kegler, F. Kremer, and P. Linse. Forces between single pairs of charged colloids in aqueous salt solutions. *Physical Review E*, 76(3):031403, September 2007.

[148] J.-C. Meiners and S. R. Quake. Direct Measurement of Hydrodynamic Cross Correlations between Two Particles in an External Potential. *Physical Review Letters*, 82(10):2211–2214, March 1999.

[149] F. Huang, K. Addas, A. Ward, N. T. Flynn, E. Velasco, M. F. Hagan, Z. Dogic, and S. Fraden. Pair Potential of Charged Colloidal Stars. *Physical Review Letters*, 102(10):108302, March 2009.

[150] K. Kegler, M. Konieczny, G. Dominguez-Espinosa, C. Gutsche, M. Salomo, F. Kremer, and C. N. Likos. Polyelectrolyte-Compression Forces between Spherical DNA Brushes. *Physical Review Letters*, 100(11):118302, March 2008.

[151] G. Dominguez-Espinosa, A. Synytska, A. Drechsler, C. Gutsche, K. Kegler, P. Uhlmann, M. Stamm, and F. Kremer. Optical tweezers to measure the interaction between poly(acrylic acid) brushes. *Polymer*, 49(22):4802–4807, October 2008.

[152] D. Murakami, A. Takenaka, M. Kobayashi, H. Jinnai, and A. Takahara. Measurement of the electrostatic interaction between polyelectrolyte brush surfaces by optical tweezers. *Langmuir : the ACS journal of surfaces and colloids*, 29(52):16093–7, December 2013.

[153] J. C. Crocker and D. G. Grier. Microscopic measurement of the pair interaction potential of charge-stabilized colloid. *Physical Revew Letters*, 73(2):352–355, July 1994.

[154] J. C. Crocker and D. G. Grier. When Like Charges Attract: The Effects of Geometrical Confinement on Long-Range Colloidal Interactions. *Physical Revew Letters*, 77(9):1897–1900, August 1996.

[155] S. Sainis, V. Germain, and E. Dufresne. Statistics of Particle Trajectories at Short Time Intervals Reveal fN-Scale Colloidal Forces. *Physical Review Letters*, 99(1):018303, July 2007.

[156] J. C. Crocker, J. A. Matteo, A. D. Dinsmore, and A. G. Yodh. Entropic Attraction and Repulsion in Binary Colloids Probed with a Line Optical Tweezer. *Physical Review Letters*, 82(21):4352–4355, May 1999.

[157] M. Polin, Y. Roichman, and D. G. Grier. Autocalibrated colloidal interaction measurements with extended optical traps. *Physical Review E*, 77(5):051401, May 2008.

[158] M. Mittal, P. P. Lele, E. W. Kaler, and E. M. Furst. Polarization and interactions of colloidal particles in ac electric fields. *The Journal of chemical physics*, 129(6):064513, August 2008.

[159] R. Verma, J. C. Crocker, T. C. Lubensky, and A. G. Yodh. Attractions between Hard Colloidal Spheres in Semiflexible Polymer Solutions. *Macromolecules*, 33(1):177–186, January 2000.

[160] K. Svoboda, C. F. Schmidt, B. J. Schnapp, and S. M. Block. Direct observation of kinesin stepping by optical trapping interferometry. *Nature*, 1993.

[161] A. C. Richardson, S. N. S. Reihani, and L. B. Oddershede. Non-harmonic potential of a single beam optical trap. *Optics express*, 16(20):15709–15717, 2008.

[162] K. C. Neuman and S. M. Block. Optical trapping. *The Review of scientific instruments*, 75(9):2787–809, September 2004.

[163] M. P. N. Juniper, R. Besseling, D. G. A. L. Aarts, and R. P. A. Dullens. Acousto-optically generated potential energy landscapes: potential mapping using colloids under flow. *Optics express*, 20(27):28707–16, December 2012.

[164] C. Bechinger, M. Brunner, and P. Leiderer. Phase Behavior of Two-Dimensional Colloidal Systems in the Presence of Periodic Light Fields. *Physical Review Letters*, 86(5):930–933, January 2001.

[165] C. Schmitt, B. Dybiec, P. Hänggi, and C. Bechinger. Stochastic resonance vs. resonant activation. *Europhysics Letters (EPL)*, 74(6):937–943, June 2006.

[166] R. D. L. Hanes, C. Dalle-Ferrier, M. Schmiedeberg, M. C. Jenkins, and S. U. Egelhaaf. Colloids in one dimensional random energy landscapes. *Soft Matter*, 8(9):2714, 2012.

[167] A. Curran, M. P. Lee, M. J. Padgett, J. M. Cooper, and R. Di Leonardo. Partial Synchronization of Stochastic Oscillators through Hydrodynamic Coupling. *Physical Review Letters*, 108(24):240601, June 2012.

[168] J. Dobnikar, M. Brunner, and H.-H. von Grünberg. Three-body interactions in colloidal systems. *Physical Review E*, 69(3):031402, March 2004.

[169] R. Tuinier, J. K. G Dhont, and T.-H Fan. How depletion affects sphere motion through solutions containing macromolecules. *Europhysics Letters (EPL)*, 75(6):929–935, September 2006.

[170] T.-H. Fan, J. Dhont, and R. Tuinier. Motion of a sphere through a polymer solution. *Physical Review E*, 75(1):011803, January 2007.

[171] D. Aarts, R. Tuinier, and H. Lekkerkerker. Phase behaviour of mixtures of colloidal spheres and excluded-volume polymer chains. *Journal of Physics: Condensed Matter*, 7551, 2002.

[172] T. Godazgar, R. Shokri, and S. N. S. Reihani. Potential mapping of optical tweezers. *Optics letters*, 36(16):3284–6, August 2011.

[173] M. Jahnel, M. Behrndt, A. Jannasch, E. Schäffer, and S. W. Grill. Measuring the complete force field of an optical trap. *Optics letters*, 36(7):1260–2, April 2011.

List of publications

To date the following publications based upon work in this thesis have been submitted or are in preparation:

Samantha J. Ivell, Roel P.A. Dullens, Stefano Sacanna, Dirk G.A.L. Aarts, (2013), *Emerging structural disorder in a suspension of uniformly dimpled colloidal particles*, Soft Matter, **9**, 9361-9365 (Chapter 4)

Acknowledgements

Firstly, I would like to thank Dirk Aarts for all of his help, patience, guidance and ideas throughout the course of my DPhil. It's been a long road, paved with many long-winded emails from me, but we got there in the end!

Thanks also go to Roel Dullens for his additional input and advice, and to Arran Curran for his help with the challenging last chapter. Thank you to Stefano Sacanna for sticking with me through the particle synthesis. I would like to thank all the members of the Aarts and Dullens groups, both past and present. Liz, for showing me how things were done, and for being a great counsel even after leaving the group. Tom, for always being calm, reassuring, and spontaneous on Wednesdays. Oli, for the constant source of amusement in the upstairs office (squash gate?), and Paola, for the amazing times we had in Crete. I'd also like to thank Alice for the cake, wine and maths, and Julia for all the rowing gossip. Special thanks go to Mike for being there when I needed help, both at work and outside of it. You all made the past 3.5 years great.

Additionally, thanks go to LCBC, for showing me that there are other things to life than just work, and for somehow turning me into a rower. Thank you to Claire Wills and Paul Crewe for teaching me how to row and pushing me, and to all the ladies at CORC for helping me to continue doing what I love.

Ziz and Nads, thank you so much. I couldn't have got to the end without your constant support and friendship (even if I did have to sacrifice the delicious yoghurt). You always said the right things to get me back on track.

Finally, I would like to thank my parents and Simon for encouraging and supporting me the whole way through my DPhil.